Studies of Nuclear Structure using Heavy Ion-induced Transfer Reactions

Thesis submitted in accordance with the requirements of
the University of Liverpool for the degree of Doctor of Philosophy

by

Alan James Cresswell

Oliver Lodge Laboratory

September 1994

Abstract

Three experiments were carried out to use Heavy Ion-induced Transfer Reactions (HITR) to study the nuclear structure of the residual nuclei.

The first experiment used the ^{195}Pt(^{61}Ni,^{62}Ni)^{194}Pt reaction at a beam energy of 305 MeV to attempt to populate a superdeformed band in ^{194}Pt. Gates set on a p-γ-γ matrix and a computer search code, ASAP, were used to look for a superdeformed band. There was no evidence that a superdeformed band was populated in this experiment.

The second experiment used the ^{239}Pu(^{117}Sn,^{118}Sn)^{238}Pu reaction at a beam energy of 630 MeV to attempt to populate the known 0.5 ns fission isomer in ^{238}Pu. The cross sections for the prompt fission of ^{238}Pu populated by transfer and ^{239}Pu following inelastic excitation were measured to be (6$\pm$2) mb and (1.7$\pm$1.0) mb respectively. A single candidate fission event was observed, most probably corresponding to the population of the fission isomer in ^{238}Pu with a cross section of (80 $\pm$ 80) nb. There was no enhancement of the population of the fission isomer compared to light-ion induced reactions.

The final experiment used the ^{161}Dy(^{61}Ni,^{62}Ni)^{160}Dy reaction at a beam energy of 270 MeV to populate two quasiparticle states in ^{160}Dy. Gates set on a p-γ-γ matrix were used to study the decay of ^{160}Dy, in particular the population of collective bands built on two quasiparticle excitations. Transitions from the S-band and 1^-, 4^- and 8^--bands built on two quasiparticle states involving the $1i_{\frac{13}{2}}$, $\Omega = \frac{5}{2}$ neutron orbital, a 2^- octupole band and a 4^+-band were populated. There was also some data from the ^{161}Dy(^{61}Ni,^{60}Ni)^{162}Dy reaction. No transitions from two quasiparticle bands in ^{162}Dy were observed. The experimental data was compared with semi-classical transfer theory (SCTT) calculations. The population of the octupole bands in ^{160}Dy was stronger than expected using the SCTT.

Acknowledgements

The research described in this thesis was carried out during the period 1990 to 1994. I would like to express my thanks to Professors P.J. Twin and E. Gabathuler for giving me the opportunity to pursue this work in the Department of Physics at Liverpool. Financial support during the first three years of study was provided by the Science and Engineering Research Council.

I would like to thank all who have been associated with this work. I would like to express my thanks to past and present members of the Nuclear Structure Group in Liverpool, in particular my supervisor Dr. P.A. Butler and Dr. G.D. Jones for their help and advise. Much of this work was carried out in collaboration with a group from the University of Rochester Nuclear Structure Research Laboratory, and I would like to thank them as well, in particular Dr. C-Y. Wu, Prof. D. Cline and Matt Devlin.

I would also like to express my gratitude to all those who have helped to make my time in Liverpool so enjoyable. I would like to thank Mark Dolman for introducing me to the joys of hill walking and accompanying me on walks when I needed to escape Liverpool. My thanks also goes to all those with whom I have shared a few pints. Finally, my gratitude goes to the members of the Methodist Society and Christian Union and the congregation of Elm Hall Drive Methodist Church who helped my Christian faith to grow, in particular I would like to thank David Wilkinson for encouraging me to see physics and my faith as complimentary.

Now I know in part; then I shall know fully, even as I am fully known.

1Corinthians 13:12

Contents

Abstract i

Acknowledgements ii

Contents iii

1 Introduction. **1**

1.1 Population of Second Minima. 2

1.2 Population of Quasiparticle States. 9

2 Properties of Heavy Ion-Induced Transfer Reactions. **12**

2.1 Introduction. 12

2.2 Scattering of Heavy Ions. 13

2.3 Transfer Reactions. 16

2.4 Coulomb Excitation and High Spin States. 19

3 Attempt to Populate Superdeformed Bands in Pt Nuclei. **21**

3.1 Introduction. 21

3.2 Experimental Apparatus. 22

3.3 The Data Analysis. 27

3.4 Results. 29

3.5 Discussion. 33

4 Attempt to Populate Fission Isomers in Pu Nuclei. **36**

4.1 Introduction. 36

4.2 Experimental Details. 37

4.3 Analysis of Data. 41

4.3.1 The Monte Carlo Simulation. 46

4.4 Results. 50
4.4.1 Summary of the γ-ray Spectroscopy. 50
4.4.2 Prompt Fission Results. 55
4.4.3 Delayed Fission Results. 61
4.5 Discussion. 63

5 Population of Two Quasiparticle States in Dy Nuclei. 65
5.1 Introduction. 65
5.2 Experimental Details. 67
5.3 Results. 72
5.3.1 Excitation Energy Sharing. 72
5.3.2 Inelastic Excitation of ^{161}Dy. 76
5.3.3 The Population of ^{160}Dy. 79
5.3.4 The Population of ^{162}Dy. 89
5.3.5 γ-ray Multiplicities. 90
5.4 Discussion. 93
5.4.1 Semi-classical Transfer Theory (SCTT). 96
5.4.2 SCTT Applied to the ^{161}Dy(^{61}Ni,^{62}Ni)^{160}Dy Reaction. 100
5.4.3 SCTT Applied to the ^{161}Dy(^{61}Ni,^{60}Ni)^{162}Dy Reaction. 110
5.4.4 Comparison of Pick-up and Strippping Channels. 114
5.5 Summary. 114

6 Summary and Conclusion. 116
6.1 Summary. 116
6.1.1 Population of Second Minima. 116
6.1.2 Population of Quasiparticle States. 117
6.2 Conclusions and Further Work. 117

Bibliography 119

Chapter 1

Introduction.

Direct transfer reactions with light ions have played an important role in the development of nuclear physics. For example, the (d,p) deuteron stripping reaction transfers a neutron from the incident deuteron to the target nucleus with the scattered proton carrying information on the angular momentum with which the neutron entered the target nucleus. This is a useful spectroscopic tool because the process can be treated as the transfer of a neutron into a definite single particle orbital in the final nucleus.

The development of new technical facilities and theoretical analysis methods have allowed the use of nucleon transfer reactions using heavy ions. Much of the pioneering work on Heavy Ion-induced Transfer Reactions (HITR) was carried out at Yale[1] and Heidelberg[2] in the mid-1960's. Both these laboratories concentrated on light nucleus-nucleus systems where nuclear structure calculations and light ion-induced transfer data were available for comparison.

Near the end of the 1970's transfer reactions with very heavy ions became possible. At the GSI a magnetic spectrograph[3, 4], conversion electrons[5] and particle-γ techniques[6] were used to study various nuclei. At the Lawrence Berkeley Laboratory the p-p-γ coincidence method[7] was also used. In none of these experiments was it possible to separate the ground band population from other bands due to poor energy resolution.

The development of Ge detector arrays improved the energy resolution of such experiments and made it possible to separate the population of bands. Large detector arrays also makes it possible to use high statistics γ-γ coincidence experiments with well resolved γ-rays.

HITR can provide information similar to that obtained with light ion reactions, but collective excitation in both the entrance and exit channels is stronger in heavy ion reactions as a result of the much larger electromagnetic fields. This can result in transfer between states that are collectively excited, and the collective excitation of states in the residual nucleus. So, for example, single particle and pairing modes can be studied under the influence of high collective angular momentum.

Also, HITR offers the possibility of populating states that are inaccessible to other reaction mechanisms. In particular high spin states in neutron rich nuclei which are not accessible to compound nucleus reactions, and single particle and quasiparticle excitations inaccessible to Coulomb excitation experiments.

HITR are "cold" reactions, that is they populate states close to the yrast line in the residual nucleus. Experiments in several mass regions[8, 9] have shown that HITR preferentially populate aligned quasiparticle states near the yrast line. This can be seen in figure 1.1 which shows plots of total energy against multiplicity for the ^{161}Dy(^{58}Ni,^{59}Ni)^{160}Dy and ^{235}U(^{58}Ni,^{59}Ni)^{234}U reactions.

In both of these reactions there are two peaks in the plot of total energy against multiplicity, a strong population at high energy and multiplicity and a weaker population at low energy and multiplicity. These were interpreted as corresponding to the population of excited quasiparticle states and the ground state respectively.

In the experiment using the ^{235}U(^{58}Ni,^{59}Ni)^{234}U reaction at a beam energy of 325 MeV[9] it was shown that states with spins upto (26^+) were populated without appreciable fission competition. In another experiment using the ^{235}U(^{206}Pb,^{207}Pb)^{234}U reaction at a beam energy of 1394 MeV[10] there was population of states with spins upto (30^+). In the experiment using the ^{161}Dy(^{58}Ni,^{59}Ni)^{160}Dy reaction at a beam energy of 270 MeV[8] states upto spin $I \sim 20$ were observed.

1.1 Population of Second Minima.

The potential energy surface of many nuclei shows a second minimum at larger deformation, as is shown in figure 1.2, as a result of shell structure. For nuclei in the mass $A \approx 130$, $A \approx 150$ and $A \approx 190$ regions this second minimum results in

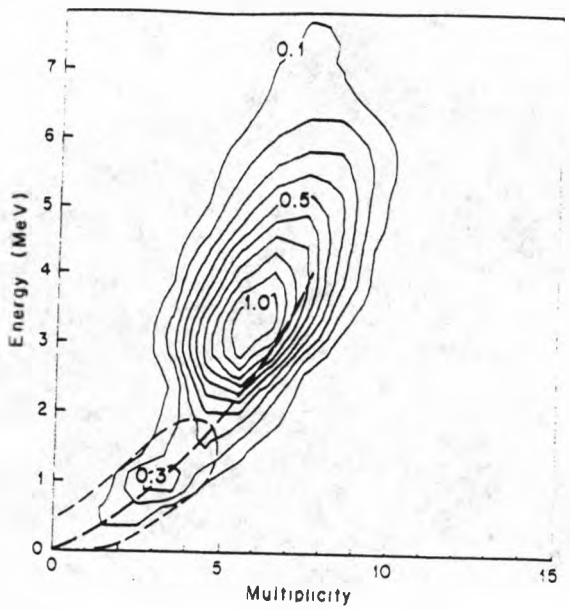

(a)

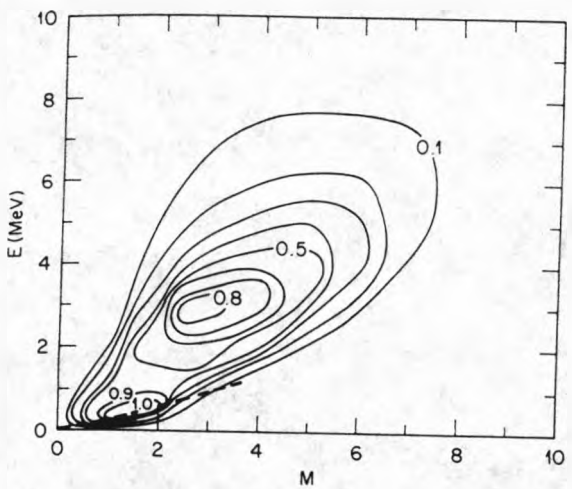

(b)

Figure 1.1: Plots of total energy against multiplicity for (a) the ^{161}Dy(^{58}Ni,^{59}Ni)^{160}Dy and (b) the ^{235}U(^{58}Ni,^{59}Ni)^{234}U reactions. The plots are taken from references [8] and [9] respectively. The heavy dashed lines indicate the yrast lines in ^{160}Dy and ^{234}U respectively, the events which are below these lines reflect finite resolution. The light dashed line in (a) is the 0.1 contour for the inelastic reaction ^{161}Dy(^{58}Ni,^{58}Ni$'$)^{161}Dy$'$.

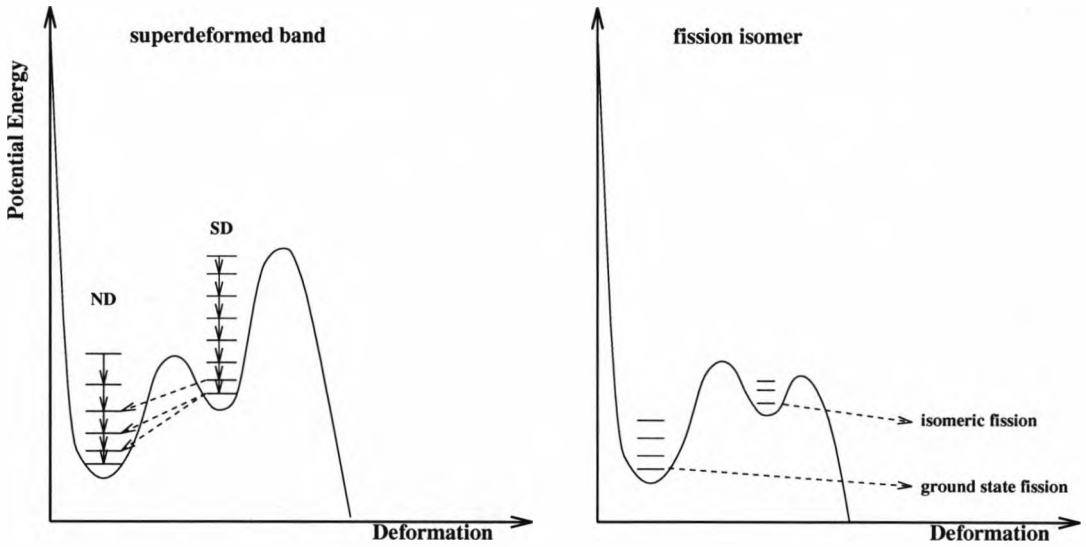

Figure 1.2: The potential surface of a nucleus with either a superdeformed band or a fission isomer.

superdeformed bands, rotational sequences built upon excited deformed states with an axis ratio of about 2:1[11]. The superdeformed band (SD) decays into the normal deformed state (ND) via many γ-rays which have not been observed. In the mass $A \approx 240$ region the second minimum results in fission isomers, excited nuclear states which decay by spontaneous fission with half lives ranging from a few ps to a few ms[12]. This is $\sim$ 30 orders of magnitude shorter than for spontaneous fission from the respective nuclear ground states as a result of the reduced fission barrier experienced by the isomer.

There are three possible mechanisms for populating such states; compound nucleus reactions (fusion-evaporation), light ion-induced reactions or HITRs. Compound nucleus reactions have been very effective at populating superdeformed states. They involve the fusion of two heavy ions forming a very hot compound nucleus which then cools by boiling off several nucleons and high energy statistical γ-rays. They populate nuclei at very high spin and excitation energy. Compound nucleus reactions can not be used to populate fission isomers because the high excitation energy results in a very large amount of prompt fission due to the relatively small fission barrier. This is illustrated in figure 1.3. These reactions are also limited to nuclei on the proton-rich side of the line of stability as a result of the curvature of the stability line in the (N,Z) plane and because several neutrons have to boil off a hot spinning nucleus to cool it

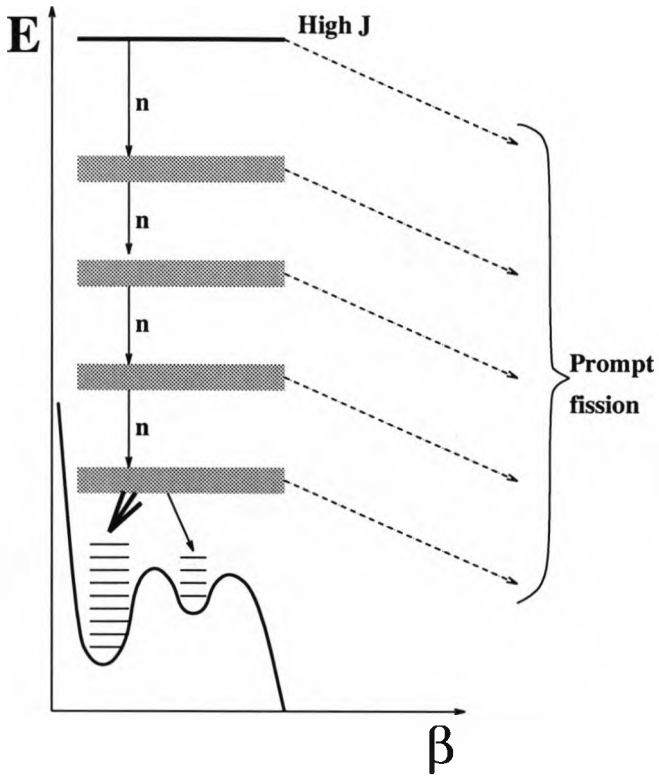

Figure 1.3: Population of fission isomers by using a compound nucleus reaction. The large excitation energy of the residual nucleus results in a very large amount of prompt fission.

before γ-ray emission.

Light ion induced reactions have been successfully used to populate fission isomers. These reactions populate nuclei at much lower spin and excitation energy than compound nucleus reactions. They are not very useful for populating superdeformed bands because they introduce insufficient angular momentum into the system, however the low excitation energy results in much less prompt fission when populating fission isomers. This is illustrated in figure 1.4.

It is hoped that the properties of HITR can be utilized to populate second minima states.

Superdeformed bands in the $A \approx 190$ region become yrast, that is become the lowest energy state for a given spin, at about spin 30 $\hbar$. So, if a HITR introduces sufficient angular momentum into the reaction then the residual nucleus will be formed in the region where the superdeformed band is close to the yrast line, and so may be populated. If a superdeformed band is populated then the strong electromagnetic

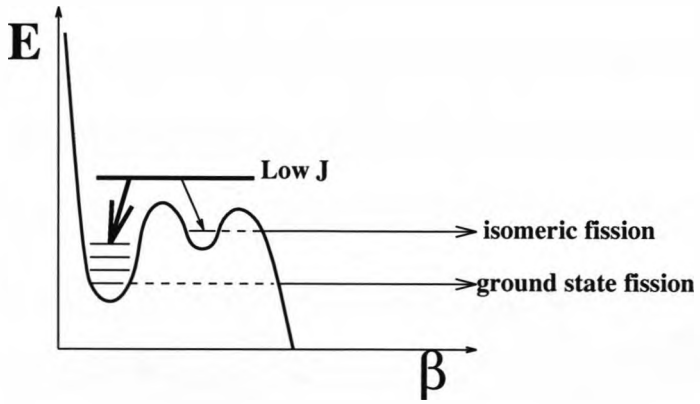

Figure 1.4: Population of fission isomers by using a light ion induced reaction. The lower excitation energy of the residual nucleus compared with compound nucleus reactions results in much less prompt fission.

field associated with the heavy ions will Coulomb excite the nucleus because of the large quadrupole moment resulting from the large deformation. This is illustrated in figure 1.5.

In the $A \approx 190$ region superdeformed bands are observed to spins as low as 8^+[13]. In this region the decay out of the superdeformed band may be due to the mixing of the wavefunctions between the first and second potential wells for the lowest spin states of the superdeformed band. The wavefunctions for the superdeformed band at this point would be of the form

$$\psi_{SD} = \alpha\psi_I + \beta\psi_{II} \tag{1.1}$$

where ψ_I is a wavefunction located at normal deformation, and ψ_{II} is a wavefunction located at superdeformation. For higher spins $I \geq 10$ the superdeformed wavefunction becomes located in the second minimum as $\alpha \rightarrow 0$.

This offers a second possible mechanism for the population of a superdeformed band using a HITR. If the residual nucleus is populated with sufficient spin (~4–8 $\hbar$) and energy (4–5 MeV) then the nucleus will be left in the region where the wavefunctions mix. The superdeformed band will then be preferentially Coulomb excited. This is illustrated schematically in figure 1.6.

Both of these mechanisms should be selective, in that the data will contain γ-rays from only two or three nuclei and only the superdeformed band will be significantly inelastically excited. So, a HITR offers the possibility of studying a superdeformed

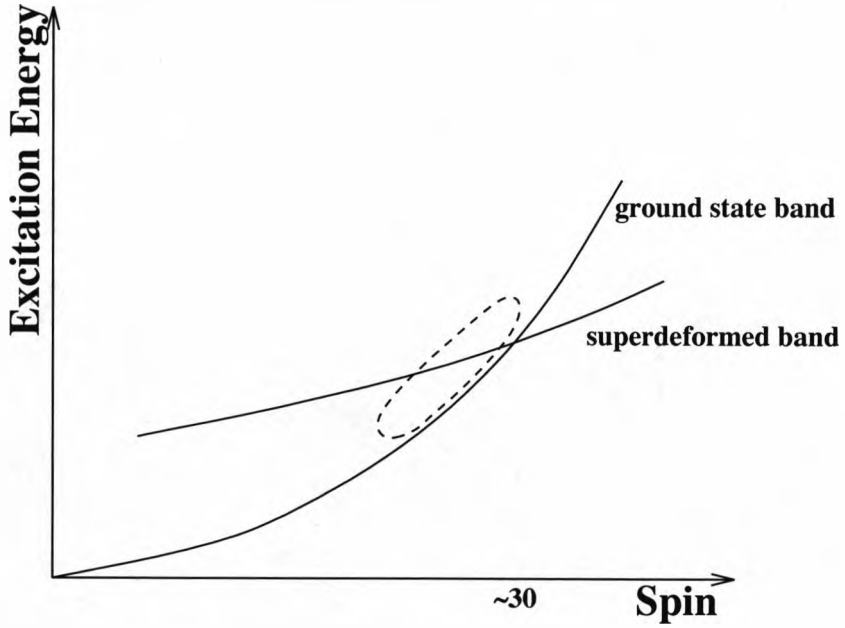

Figure 1.5: The population of a superdeformed band using a HITR. The reaction leaves the residual nucleus in a cold state, near the yrast line. If sufficient angular momentum is introduced in the reaction that the residual nucleus is populated in the region enclosed by the dashed line then the superdeformed band should be populated.

band in a nucleus inaccesible to compound nucleus reactions.

In order to study fission isomers in more detail it would be desirable to populate them with a larger cross section and at higher spin than is possible with light ion induced reactions. This could possibly increase the population of fission isomers, and maybe make it possible to study the properties of the second minimum by observing the γ-rays emitted as the nucleus de-excites.

HITR offers such a possibility, as is illustrated schematically in figure 1.7. HITR should preferentially populate two quasiparticle excitations in the residual nucleus close to the yrast line. The excitation and spin of these states should be low enough that competition from prompt fission is not appreciable, as has been observed for the ^{235}U(^{58}Ni,^{59}Ni)^{234}U reaction[9]. If these states couple to the fission isomeric state then such a reaction would significantly populate the second minimum state at high spin, allowing the state to be studied.

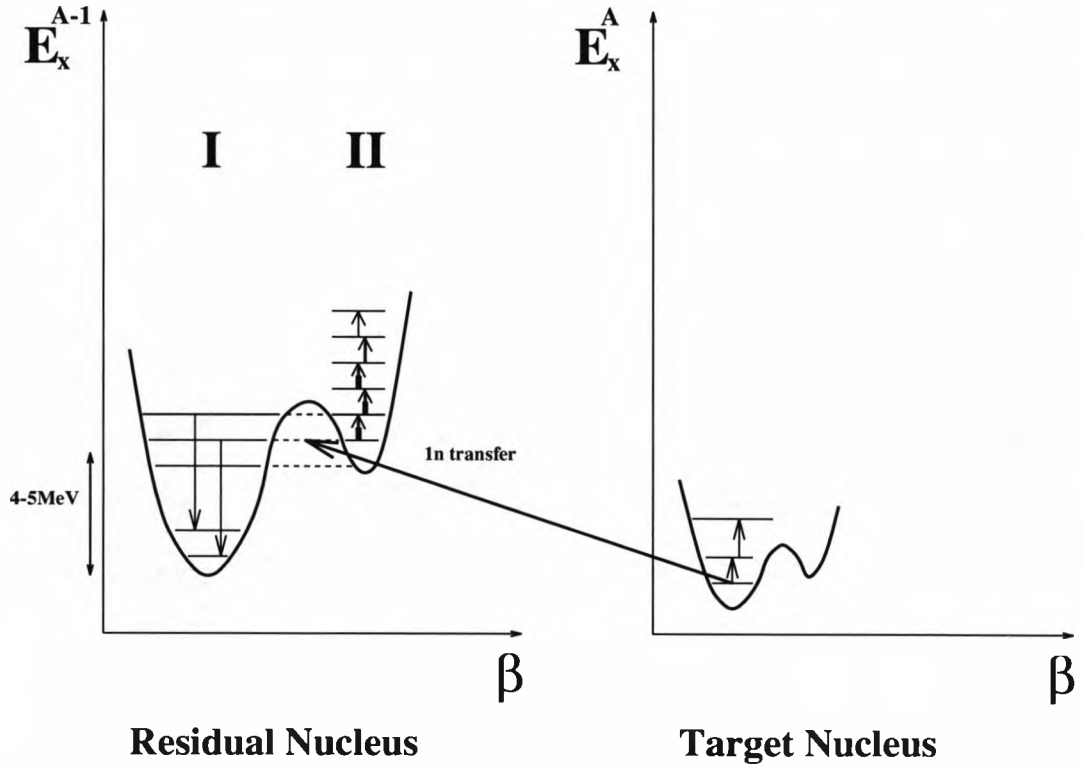

Figure 1.6: Diagram showing the second possible mechanism for populating a superdeformed band. The transfer reaction leaves the residual nucleus at the right spin and excitation energy to be in the region where the superdeformed wavefunction is a mixture of normal and superdeformed wavefunctions. The superdeformed component of the wavefunction is then preferentially Coulomb excited.

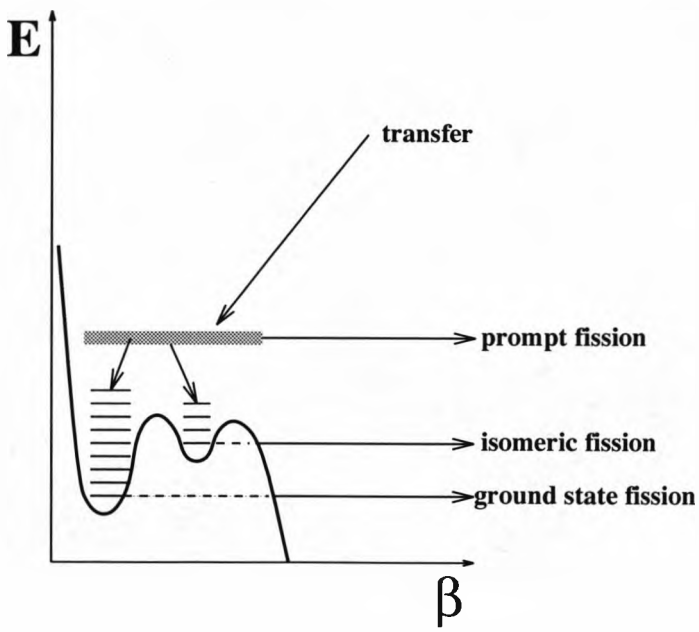

Figure 1.7: Population of fission isomers by using HITR. The intermediate spin and excitation energy allow the population of the isomer at higher spin than is possible using light ion induced reactions, but with much less prompt fission than using heavy ion compound nucleus reactions.

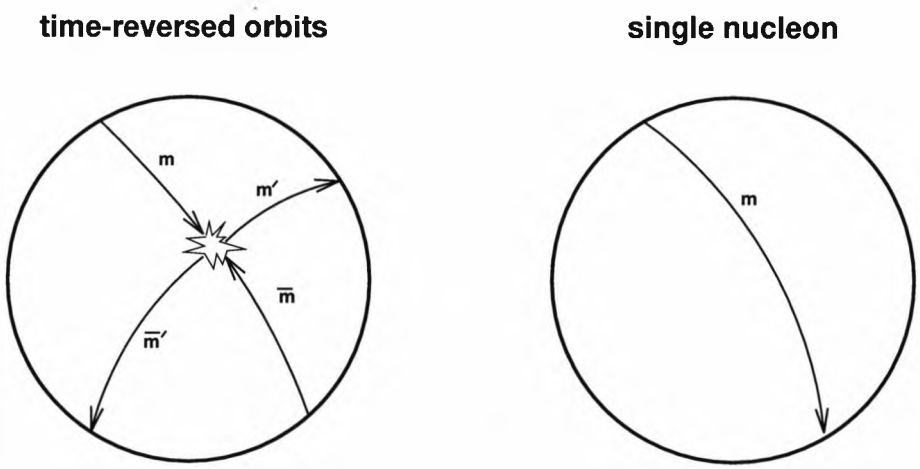

Figure 1.8: A pair of nucleons in time-reversed orbits m and $\overline{m}$ scatter off each other into a new pair of time-reversed orbits, m' and $\overline{m}'$. A single nucleon can not scatter, and so stays in the same orbit.

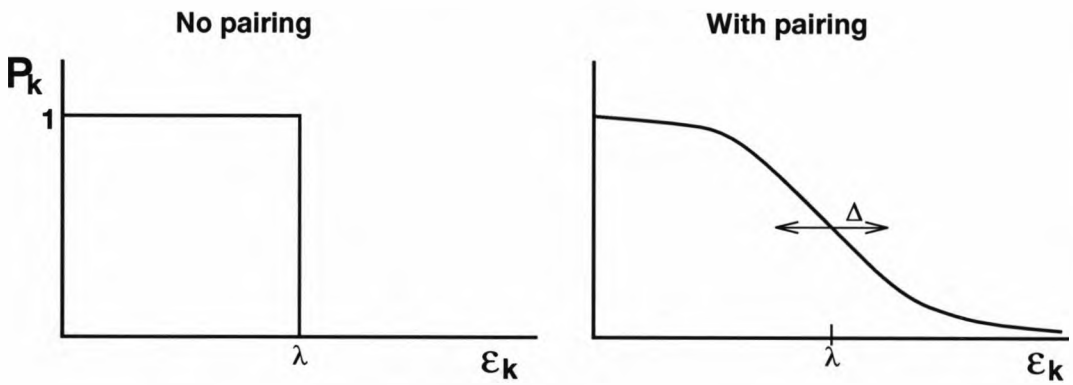

Figure 1.9: The effect of pairing on the population of nuclear states. The population P_k of a state k with energy ε_k is smeared out around the Fermi energy λ.

1.2 Population of Quasiparticle States.

The introduction of a pairing interaction (strength $\Delta \sim 1$ MeV) causes states within $\sim \Delta$ of the Fermi surface to mix together. The reason for this can be seen schematically in figure 1.8, which shows a pair of time-reversed orbits, m and $\overline{m}$. The nucleons in these orbits scatter off each other into another pair of time-reversed orbits, m' and $\overline{m}'$. This results in a smearing out of the population of states as illustrated in figure 1.9. Each state has a population $P_k = v^2$, an amplitude v of particles and u of holes with $v^2 + u^2 = 1$.

In a deformed nucleus each state is doubly degenerate with time-reversed pairs of orbits. In the paired state each of these orbits is equally occupied. However, if

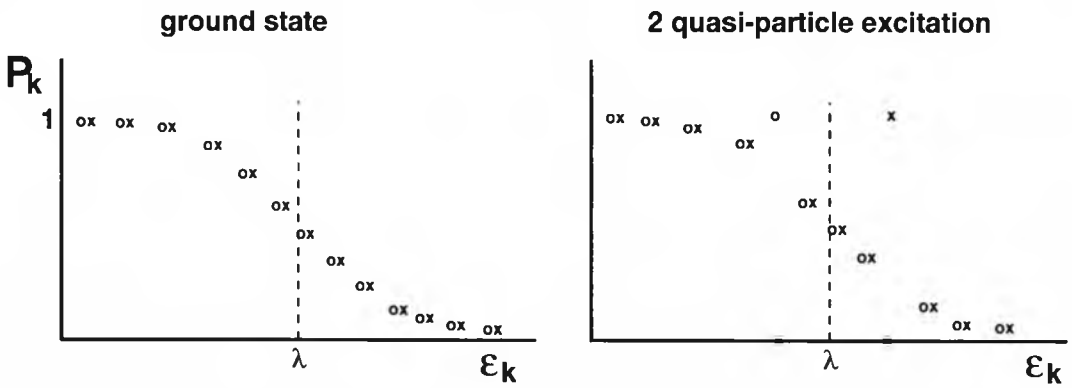

Figure 1.10: A two quasiparticle excitation formed from the ground state by breaking a pair of time-reversed orbits (**ox**) in the ground state. One orbit is completely filled and the other emptied.

one pair is broken each nucleon blocks a pair of time-reversed orbits. This blocking is due to the Pauli exclusion principle, because for a nucleon to scatter into the unoccupied orbit the other nucleon from the original pair must go into the occupied time-reversed orbit. The single nucleon fully occupies the state it is in because there can not be another nucleon in the time-reversed orbital for it to scatter off, this is seen in figure 1.8.

The result is a quasiparticle excitation with one level filled and the corresponding time-reversed orbit empty. For even-even nuclei excited states must have an even quasiparticle number. A two quasiparticle excitation is illustrated in figure 1.10. The number of particles is conserved by the population of the empty time-reversed orbital being transferred to the other orbit involved. Odd nuclei can only have odd quasiparticle numbers since there is already one quasiparticle and breaking a pair of nucleons creates a further two quasiparticles.

The energy of a quasiparticle in state k is

$$E_k = (\Delta^2 + (\varepsilon_k - \lambda)^2)^{\frac{1}{2}} \tag{1.2}$$

Quasiparticle excitations can be easily formed in transfer reactions, which add or remove a nucleon from the target nucleus and thus create particle-hole pairs. This is shown schematically in figure 1.11.

HITR offers a mechanism for the population of such states close to the yrast line, and the simultaneous Coulomb excitation of rotational bands built upon such structures. The population of higher energy states is suppressed since these require

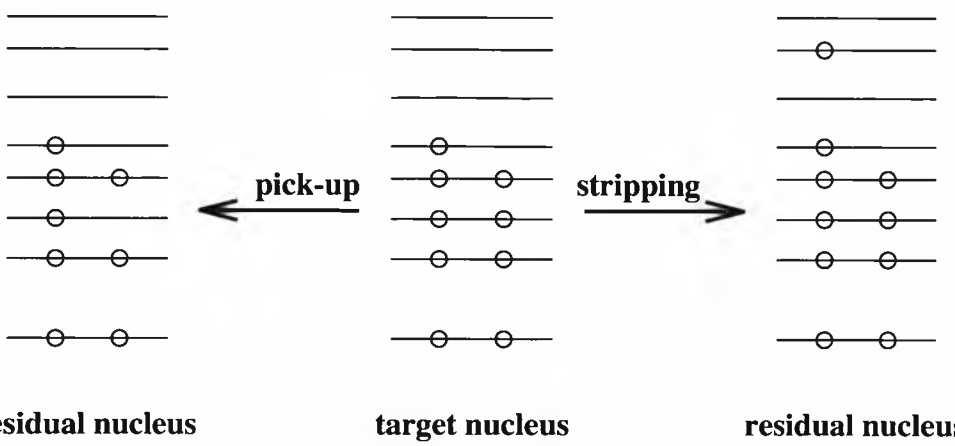

Figure 1.11: The removal or addition of a nucleon from the target nucleus can easily result in the creation of quasiparticle states, which are particle-hole states.

the removal of more tightly bound nucleons (in a pick-up reaction) or the addition of less tightly bound nucleons (in a stripping reaction), thus HITR provide a cold reaction mechanism. If the ground state Q-values are properly matched then this gives large cross sections for high spin transfer between heavy ions.

In previous experiments using the ^{161}Dy(^{58}Ni,^{59}Ni)^{160}Dy reaction at a beam energy of 270 MeV[8, 14] it was shown that HITR in the rare earth region preferentially populate excited two quasiparticle states near the yrast line, although discrete transitions from collective bands built upon such states were not observed. It is hoped that using modern Ge detector arrays the population and decay of such bands can be studied using the de-excitation γ-rays.

Chapter 2

Properties of Heavy Ion-Induced Transfer Reactions.

2.1 Introduction.

Heavy Ion-induced Transfer Reactions (HITR) are direct nuclear reactions, where one or more nucleons are transferred between a heavy projectile and target without the formation of a complex intermediate state. The large mass and energy of the ions results in a small deBroglie wavelength. The ions can then be considered as localised and following classical orbits[15]. HITR can thus be described by a semi-classical model in which the interacting ions follow classical orbits and the transfer of particles is treated quantum mechanically[16]. These are quasi-elastic reactions, with relatively small changes in mass, charge, centre of mass energy and angular momentum.

HITR are of the form $A(a,b)B$. A projectile a reacts with target nucleus A, and a nucleon or cluster x is transferred between them to give ejectile b and residual nucleus B. To first order, x is considered to be in a single particle orbit around a core which does not participate in the transfer. The reaction can either be a pick-up reaction where x is transferred from the target to the projectile or a stripping reaction where x is transferred from the projectile to the target. These two possible reactions are shown schematically in figure 2.1.

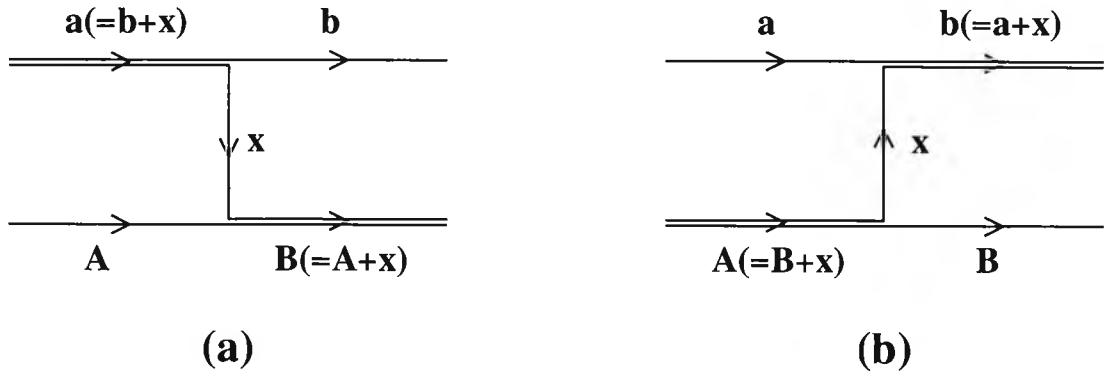

Figure 2.1: Schematic representation of (a) stripping and (b) pick-up reactions transfering a nucleon or cluster x.

2.2 Scattering of Heavy Ions.

The scattering of a projectile of mass A_1 and charge Z_1 from a target of mass A_2 and charge Z_2 is shown schematically in figure 2.2. The scattering angle θ depends on the two charges Z_1 and Z_2, the two masses A_1 and A_2, the beam energy E_{lab} and the impact parameter b. The system has a reduced mass μ and relative velocity v;

$$\mu = \frac{mA_1A_2}{A_1 + A_2} \tag{2.1}$$

$$\frac{v}{c} = \sqrt{\frac{E_{lab}}{469A_1}} \tag{2.2}$$

where m is the nucleon mass and E_{lab} is in MeV.

For energies < 15 MeV/A classical mechanics can be used. So the momentum p and wavenumber k are given by

$$p = \hbar k = \mu v \tag{2.3}$$

$$k = 1/\lambda\!\!\!^{-} = \mu v/\hbar \tag{2.4}$$

The impact parameter, b, defines the scattering orbit. It can be seen in figure 2.3 that the projectile is scattered at larger angles for smaller values of b, which is given by[17]

$$b = a\cot(\tfrac{1}{2}\theta) \tag{2.5}$$

Where a is the half distance of closest approach, which occurs when $b = 0$ (a head-on collision). It is given by

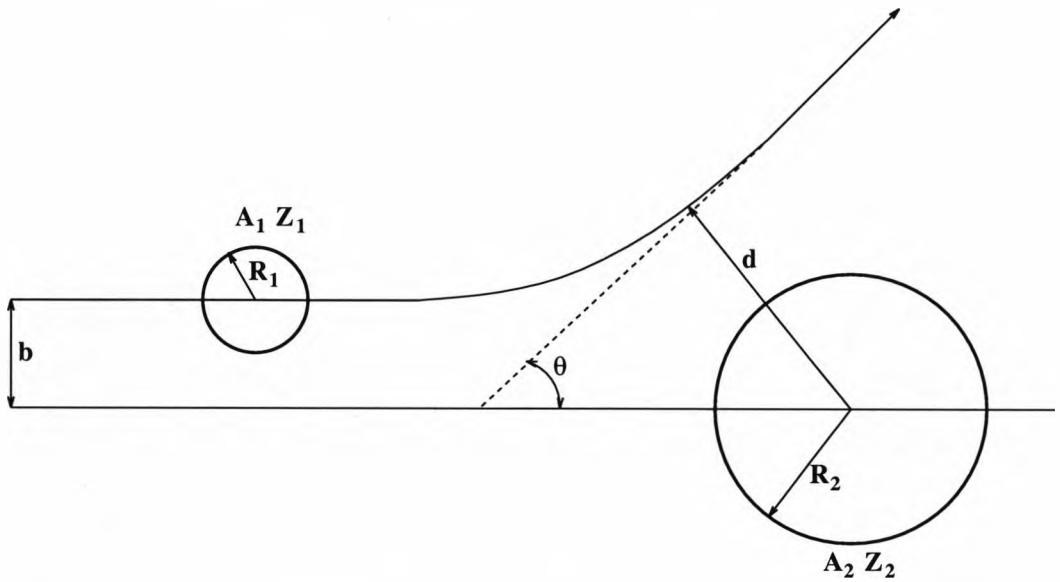

Figure 2.2: Schematic of a heavy ion mass A_1 and charge Z_1 scattering of a heavy target mass A_2 and charge Z_2. The two ions have strong interaction radii R_1 and R_2 respectively. The incoming ion approaches with an impact parameter b, and is scattered at an angle θ. The distance of closest approach between the ions is d.

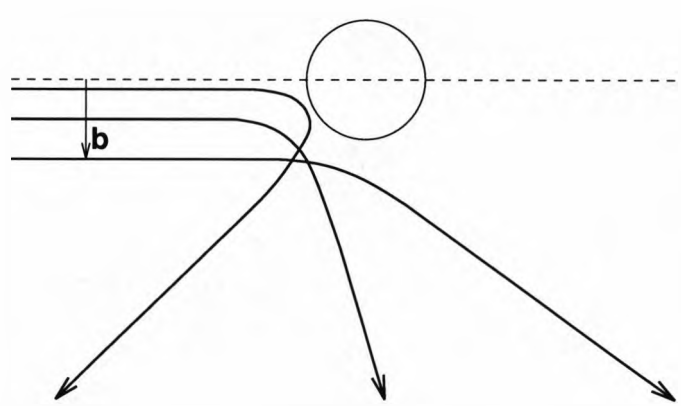

Figure 2.3: Scattering of a heavy ion off a target for different impact parameters, b.

$$a = \frac{Z_1 Z_2 e^2}{4\pi\epsilon_0 \mu v^2} \tag{2.6}$$

The angular momentum of each partial wave is

$$l = kb \tag{2.7}$$

The Sommerfeld parameter, $\eta = ka$, characterises the interaction of two heavy ions. It depends upon the ratio of the distance of closest approach for assumed point particles and the wavelength of their relative motion, if the distance of closest approach is several times the wavelength of the relative motion, $\eta \gg 1$, then the reaction can be described in terms of classical orbits. The Sommerfeld parameter is given by[16, 17]

$$\eta = \frac{Z_1 Z_2 e^2}{4\pi\epsilon_0 \hbar v} \tag{2.8}$$

In a pure Coulomb field the distance of closest approach associated with a scattering angle θ is given by[17]

$$d(\theta) = \frac{\eta}{k}\left(1 + \mathrm{cosec}(\tfrac{1}{2}\theta)\right) \tag{2.9}$$

The strong interaction radius is the sum of the strong interaction radii of each nucleus.

$$R = R_1 + R_2 = r_0(A_1^{\frac{1}{3}} + A_2^{\frac{1}{3}}) \tag{2.10}$$

Where $r_0 \approx 1.3$ fm.

The grazing or critical angle θ_c occurs when $d(\theta_c) = R$. Critical values are then

$$d(\theta_c) = R = \frac{\eta}{k}\left(1 + \mathrm{cosec}(\tfrac{1}{2}\theta_c)\right) \tag{2.11}$$

which gives
$$\sin(\tfrac{1}{2}\theta_c) = \frac{\eta}{kR - \eta} = \frac{a}{R - a} \tag{2.12}$$

$$b_c = \frac{\eta}{k}\cot(\tfrac{1}{2}\theta_c) \tag{2.13}$$

which gives
$$b_c = \frac{a\sqrt{1 - \frac{a^2}{(R+a)^2}}}{\frac{a}{R-a}} = R\sqrt{1 - \frac{2a}{R}} \tag{2.14}$$

$$l_c = kb_c = kR\sqrt{1 - \frac{2a}{R}} \tag{2.15}$$

2.3 Transfer Reactions.

For scattering with $b > b_c$ the two ions stay at a large distance, and no transfer occurs. For $b < b_c$ there is a strong overlap between the ions, this allows strong absorption into other channels (eg: compound nucleus formation) to occur. The peak of the transfer cross section is at scattering angle $\theta = \theta_c$[15], with a characteristic bell shaped distribution around this angle.

Because transfer occurs for trajectories which graze the target only orbits at or near the Fermi surface of the nucleus are involved. This results in a high degree of selectivity.

For a transfer reaction $A(a,b)B$ an entrance channel i, $a + A$, and an exit channel f, $b + B$, are defined. Both of these channels have a centre of mass energy $E^{cm}_{i,f}$, wave number $k_{i,f}$ and reduced mass $\mu_{i,f}$, given by

$$E^{cm}_i = \frac{M_A}{M_A + M_a} E_{lab} \tag{2.16}$$

$$E^{cm}_f = E^{cm}_i + Q \tag{2.17}$$

$$c\hbar k_i = (2\mu_i E^{cm}_i)^{\frac{1}{2}} \tag{2.18}$$

$$c\hbar k_f = (2\mu_f E^{cm}_f)^{\frac{1}{2}} \tag{2.19}$$

$$\mu_i = \frac{M_a M_A}{M_a + M_A} \tag{2.20}$$

$$\mu_f = \frac{M_b M_B}{M_b + M_B} \tag{2.21}$$

where M_x is the mass of nucleus x, E_{lab} is the laboratory energy of the projectile, and Q is the reaction Q-value. The ground state Q-value, Q_{gg}, of the reaction is given by

$$Q_{gg} = (\Delta_a + \Delta_A) - (\Delta_b + \Delta_B) \tag{2.22}$$

where Δ_x is the mass excess of the ground state of nucleus x.

For the classical orbits to be meaningful then they must not be disturbed appreciably by the transfer of charge and mass in the reaction. The orbits in the entrance

and exit channels must be well matched such that the jump which occurs at transfer is of the order of $\hbar$ and no more[16]. If these conditions are satisfied then a semi-classical transfer theory may be used, and the differential cross-section for a HITR may be written

$$\frac{d\sigma}{d\Omega} = \left(\frac{d\sigma}{d\Omega}\right)_R P(\theta, \rho, \xi, \delta) \tag{2.23}$$

Where $\left(\frac{d\sigma}{d\Omega}\right)_R$ is the Rutherford cross section and $P(\theta, \rho, \xi, \delta)$ is the probability of transfer[18]. $P(\theta, \rho, \xi, \delta)$ is a function that will depend upon the kinematics of the scattering and the initial and final states of the transfer. The transfer probability is discussed in more detail in section 5.4.1.

It is usually assumed that the quantum numbers describing the cores of the nuclei do not change since they do not participate in the transfer. If x is transferred from an orbit with quantum numbers n_1, l_1, j_1 to an orbit with n_2, l_2, j_2 then the transferred angular momentum, λ, is restricted by[18]

$$| l_1 - l_2 | \leq \lambda \leq (l_1 + l_2) \tag{2.24}$$

$$| j_1 - j_2 | \leq \lambda \leq (j_1 + j_2) \tag{2.25}$$

There is also a parity conservation restriction,

$$(-)^{\lambda} = (-)^{l_1 + l_2}$$

$$l_1 + l_2 + \lambda \text{ is even} \tag{2.26}$$

However, it can be shown that the favoured λ is $(l_1 + l_2)$, the maximum possible. The reason for this is shown schematically in figure 2.4. Particles are transferred preferentially between orbits perpendicular to the reaction plane and retain their direction of motion. Thus, the angular momentum changes from l_1 to $-l_2$, ie $\lambda = (l_1 + l_2)$.

Transfer reactions exhibit Q-selectivity, due to an effective Q-value near the nucleus where the transfer occurs. This results from the potential near the nucleus, U^{near}, which changes the kinetic energy near the nucleus, T^{near}, from that at infinity, T^{∞}. The effective Q-value is

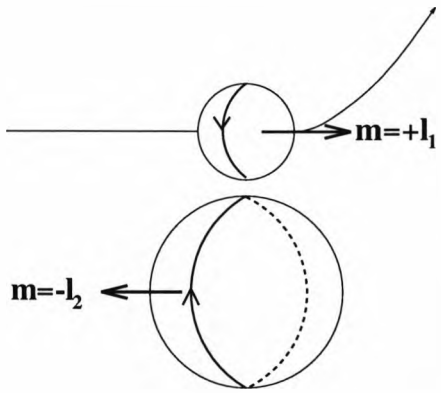

Figure 2.4: The transfer of a particle from an orbit with angular momentum l_1 to an orbit with l_2. The preferred orbits are perpendicular to the reaction plane, and the direction of motion of the transferred nucleon is retained.

$$\begin{aligned} Q_{eff} &= T_f^{near} - T_i^{near} \\ &= T_f^{\infty} - U_f^{near} - (T_i^{\infty} - U_i^{near}) \\ &= Q - (U_f^{near} - U_i^{near}) \\ &= Q - \left(\frac{Z_b Z_B e^2}{4\pi\epsilon_0 d_f} - \frac{Z_a Z_A e^2}{4\pi\epsilon_0 d_i} \right) \end{aligned} \tag{2.27}$$

where d_i and d_f are the distances of closest approach in the entrance and exit channels. For a head on collision,

$$\begin{aligned} d_i &= \frac{Z_a Z_A e^2}{4\pi\epsilon_0 E_i^{cm}} \\ d_f &= \frac{Z_b Z_B e^2}{4\pi\epsilon_0 E_f^{cm}} \end{aligned} \tag{2.28}$$

Since the charge transfer and change in energies is small $d_i \approx d_f$,

$$Q_{eff} = Q - \frac{e^2}{4\pi\epsilon_0 d_i}(Z_b Z_B - Z_a Z_A) \tag{2.29}$$

At sub-Coulomb energies the transfer must occur when the nuclei are near their distance of closest approach, when they are essentially at rest. The nuclei are then reaccelerated by the Coulomb field. For neutron transfer $E_f \approx E_i$, and $Q_{opt} \approx 0$[19]. So, the optimum excitation energy of the residual nucleus and ejectile is $E_{opt} = Q_{gg}$, since there is no charge transferred, $Z_b Z_B = Z_a Z_A$. There is a Q-window several MeV wide around this optimum value. The width of this window is illustrated

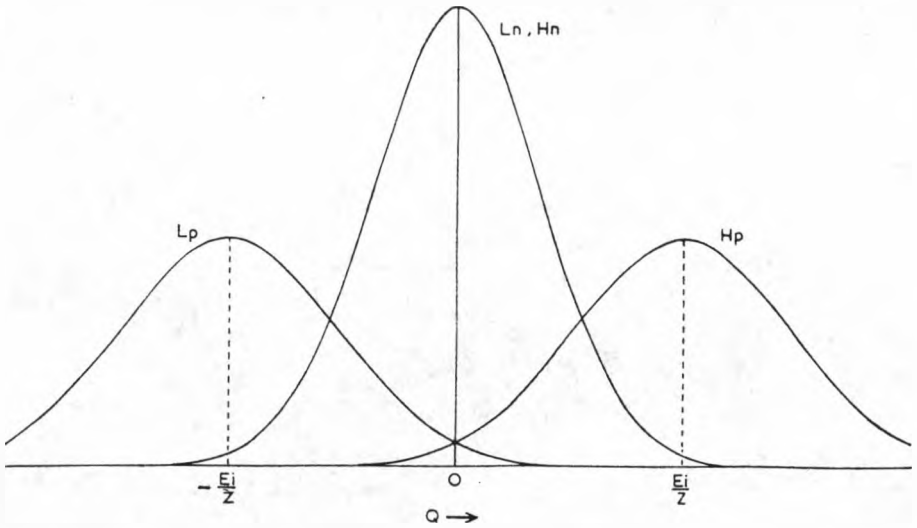

Figure 2.5: Dependence of the yield on the Q-value of a reaction with incident energy E_i and projectile charge Z, taken from reference[20].

schematically in figure 2.5 which is taken from reference[20]. This figure shows the dependence of the yield on the Q-value, for neutron transfers from the light ion (Ln) and heavy ion (Hn) and for proton transfers from the light ion (Lp) and the heavy ion (Hp). E_i is the beam energy and Z is the proton number for the projectile.

2.4 Coulomb Excitation and High Spin States.

Heavy ions offer the possibility of studying new phenomena originating in the large Coulomb contribution to the total interaction. In particular Coulomb excitation by the strong electromagnetic field to high spin states before and after the interaction by nuclear forces. This is then a multi-step process. The cross sections for nucleon transfer are expected to depend on the state of rotation achieved when the nuclear interaction occurs. The strong electromagnetic field would then also allow the Coulomb excitation of the residual nucleus.

This would make it possible to study high spin states of nuclei which are not accessible by other reaction mechanisms. It would also allow the study of single particle states and pairing structures coupled to strong collective excitation.

Using calculations based on classical mechanics and experimentally defined parameters the range of angular momenta that can be probed in very heavy ion ($A \geq 40$)

transfer reactions can be estimated[21]. With such ions transfer proceeds to states with collective angular momentum in the range $I \approx 5$–$20\ \hbar$ for rare earth targets and $I \approx 10$–$30\ \hbar$ for actinide targets. This is the angular momentum due to collective motion only. A particle or particles transferred with a large aligned component of angular momentum would increase this range. It is therefore quite conceivable to achieve direct transfer to states with spin ~ 20–$30\ \hbar$ in the rare earth region and ~ 30–$40\ \hbar$ in the actinide region.

Experimentally, HITR have produced spins upto $\sim 20\ \hbar$ on rare earth targets[14] and to spin $\sim 30\ \hbar$ on actinide targets[9, 10].

Chapter 3

Attempt to Populate Superdeformed Bands in Pt Nuclei.

3.1 Introduction.

The properties of Heavy Ion-induced Transfer Reactions (HITR) offer the possibility of populating superdeformed bands in the mass $A \approx 190$ region in nuclei inaccessible to compound nucleus reactions. In particular, superdeformed bands are predicted to exist for Pt nuclei heavier than ^{188}Pt[22], which is the heaviest Pt isotope that can be populated using a compound nucleus reaction. An experiment was carried out to attempt to populate a superdeformed band in ^{194}Pt using a HITR. The reaction used was ^{195}Pt(^{61}Ni,^{62}Ni)^{194}Pt at a beam energy of 305 MeV, with a small amount of data collected at beam energies of 295 MeV and 315 MeV. For this reaction the ground-state Q-value, $Q_{gg} = 4.3$ MeV. There was also data from the inelastic excitation (Coulex) of ^{195}Pt, and a small amount of data from the stripping reaction ^{195}Pt(^{61}Ni,^{60}Ni)^{196}Pt ($Q_{gg} = 0.10$ MeV).

Work by another group has also tried to use the ^{192}Pt(^{16}O,^{14}C)^{194}Hg two proton stripping reaction to populate the known superdeformed band in ^{194}Hg[23]. In this experiment the statistics were very poor, and the superdeformed band was not seen.

3.2 Experimental Apparatus.

The experiment was carried out at the Nuclear Structure Facility at Daresbury. A beam of typically 30 nA 305 MeV ^{61}Ni was incident on a self supporting 1 mg/cm^2 foil of 97.3% ^{195}Pt. The apparatus used was the Polytessa array[24] consisting of 21 Compton suppressed Ge detectors and a gas counter in the backward hemisphere. The Polytessa array is shown in figure 3.1. The gas counter[25] was a parallel-plate avalanche counter consisting of four quadrants, each of which had 11 position defining blobs etched onto a copper clad board forming the cathode with a thin metalized window forming the anode. These blobs were connected by 12 kΩ resistors, which together with the natural capacitance of the blobs formed a distributed RC delay line. Figure 3.2 shows the arrangement of the blobs on one quadrant, and figure 3.3 shows the schematic arrangement of the four quadrants. The counter was used to detect the back scattered Ni ions, and hence determine the direction and speed of the recoiling Pt nucleus assuming elastic scattering. This would then make it possible to correct for the Doppler shift of the γ-ray energies.

The electronics setup for Polytessa is shown in figure 3.4. The output from the BGO Compton shield was amplified and passed through a discriminator. The resulting signal was used as a veto on the Ge signals. The output from each of the Ge detectors was passed through a spectroscopic amplifier to an ADC and also through a timing filter amplifier (TFA) and a constant fraction discriminator (CFD). The resultant signal was vetoed if there was a signal in the Compton shield. The signals from the Ge detectors which were not vetoed were fed into a multiplicity logic unit (MLU) which produced a fast signal if any Ge signal was recieved (the fast γ) and a signal which is the number of γ-rays detected times 50 mV. Two discriminators were used to give a signal for single γ-rays and more than two γ-rays. The γ-γ TAC was started by the γ-γ signal and stopped by the (delayed) γ signal. For p-γ events the TAC was not started, and so the γ-γ TAC was used to identify γ-γ coincidences.

The electronic setup for the gas counter is shown in figure 3.5. The two ends of the cathode delay line were connected to voltage sensitive preamplifiers. An ion entering the detector caused a cascade which hit blob x depositing a charge Q, and causing a

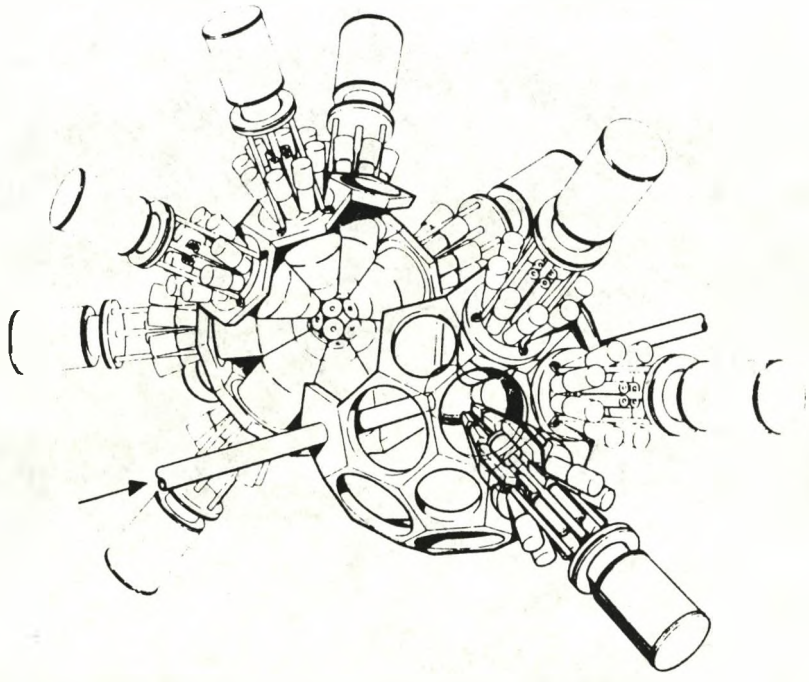

Figure 3.1: The Polytessa array. The arrow indicates the beam axis.

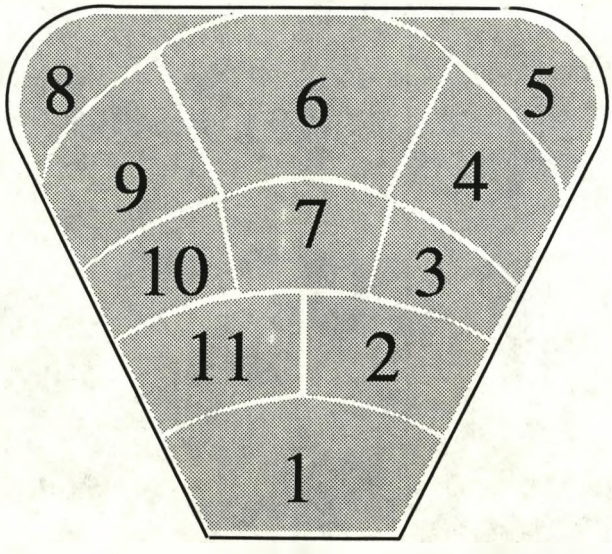

Figure 3.2: The arrangement of the 11 position defining blobs for one quadrant of the gas counter. Each of these blobs is connected in sequence by 12 kΩ resistors on the back of the board creating a delay line.

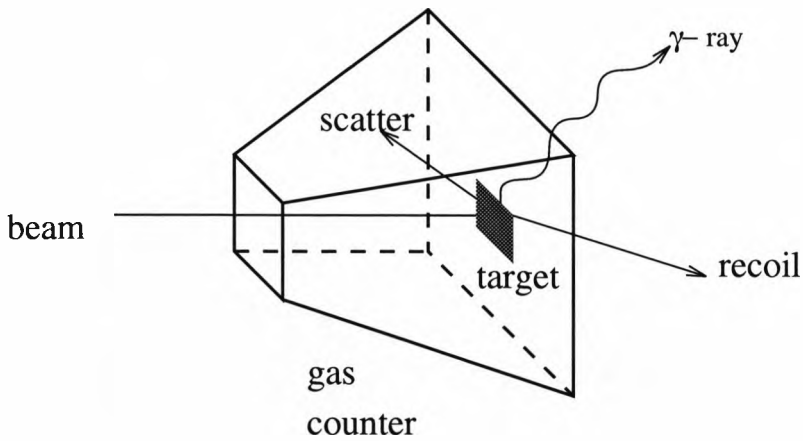

Figure 3.3: Schematic arrangement of the gas counter. The counter provides the position at which the scattered beam particle (Ni) was detected, this defines the scattering angle from which the energy and direction of the recoiling Pt can be found. Hence a correction for the Doppler shift of the γ-rays can be made.

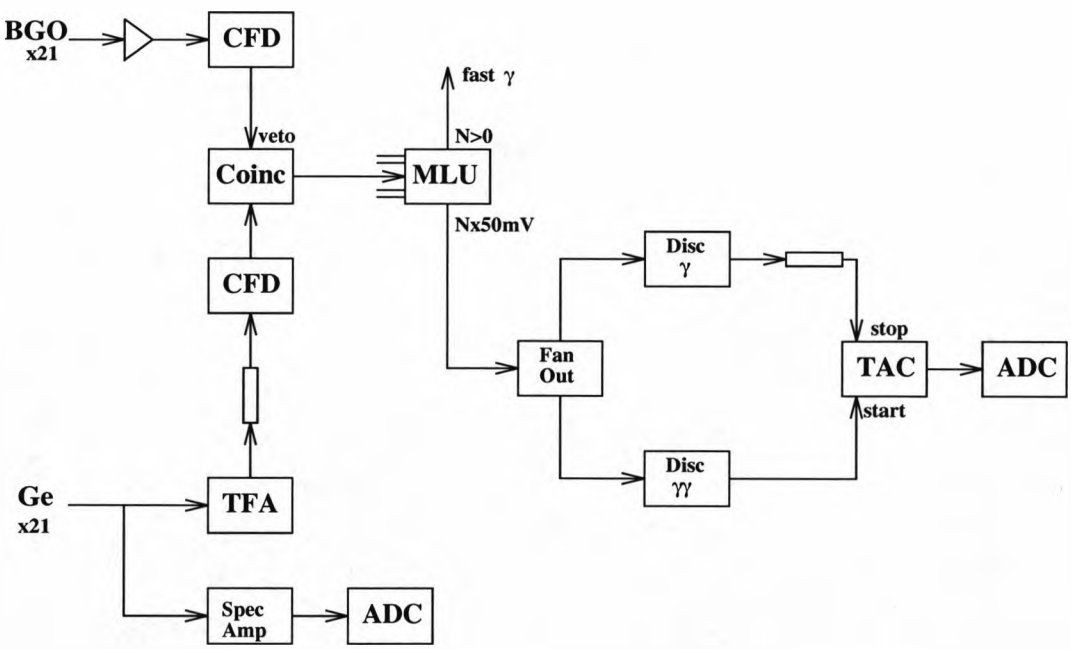

Figure 3.4: The electronic setup for Polytessa. The signals from the Ge detectors are passed through a spectroscopic amplifier into an ADC, giving the energy of the detected γ-ray. This signal is vetoed if there is a signal in the BGO detector associated with the Ge detector. The multiplicity logic unit (MLU) gives a signal if a γ-ray is detected (the fast-γ) and a signal proportional to the number of γ-rays detected. This $N\times50$ mV signal is fanned out into two discriminators, one set at 50 mV the other 100 mV. This gives a γ-γ signal used to start a TAC and a γ signal which is delayed before stopping the TAC. The resultant γ-γ TAC is a convenient means of separating out p-γ-γ events.

current to flow through the resistors connecting the blobs. This current ceased after Q had been distributed over the whole chain. The rise time of the voltages at the end of the delay line was a function of x and independent of Q. The amplified bi-polar signals from the ends of the delay line were fed into timing single channel analysers (TSCAs) which detect the crossover points of the two signals. The signals were delayed (by the times shown on figure 3.5) and used to start and stop a TAC, which generated a signal, fed into an ADC, proportional to the time difference between the crossover points. The resultant spectrum showed which blob fired. See reference [26] for a detailed description of this technique. Figure 3.6 shows the position spectrum produced for one of the quadrants of the gas counter. The peaks for the 11 blobs shown in figure 3.2 are indicated. The trigger signal was supplied by the output from the anode. The output from each anode was passed through a fast amplifier and fanned in with the outputs from the other segments. The output was used to start a TAC, the stop being given by the fast γ signal from the Polytessa electronics indicating that at least one γ-ray had been detected, generating a particle-γ TAC and the master gate.

The master gate informed the event manager that a valid event (ie: the simultaneous detection of a back scattered particle and at least one γ-ray) had occured. The output from the ADC's for each event were read and written onto magnetic tape for permanent storage if the ADC signal, auxiliary trigger and master gate were in coincidence. The event manager was controlled by a GEC4070 computer. The data was partially sorted online, during the experiment, to check that the experiment was running correctly. This sorting was done using just one of the quadrants of the gas counter. The data was later sorted offline, as described in section 3.3 using the full data set.

To calibrate the Ge detectors the master gate was set to any γ-ray. A ^{152}Eu source was then placed in the target position, and the γ-ray spectrum for each detector was recorded. The centroids of the peaks in these spectra were then used to gainmatch the Ge counters to $\frac{1}{2}$ keV per channel. The areas under the peaks were used, along with the known relative intensities of the γ-rays from the source[27], to give the relative efficiency of the detectors as a function of γ-ray energy.

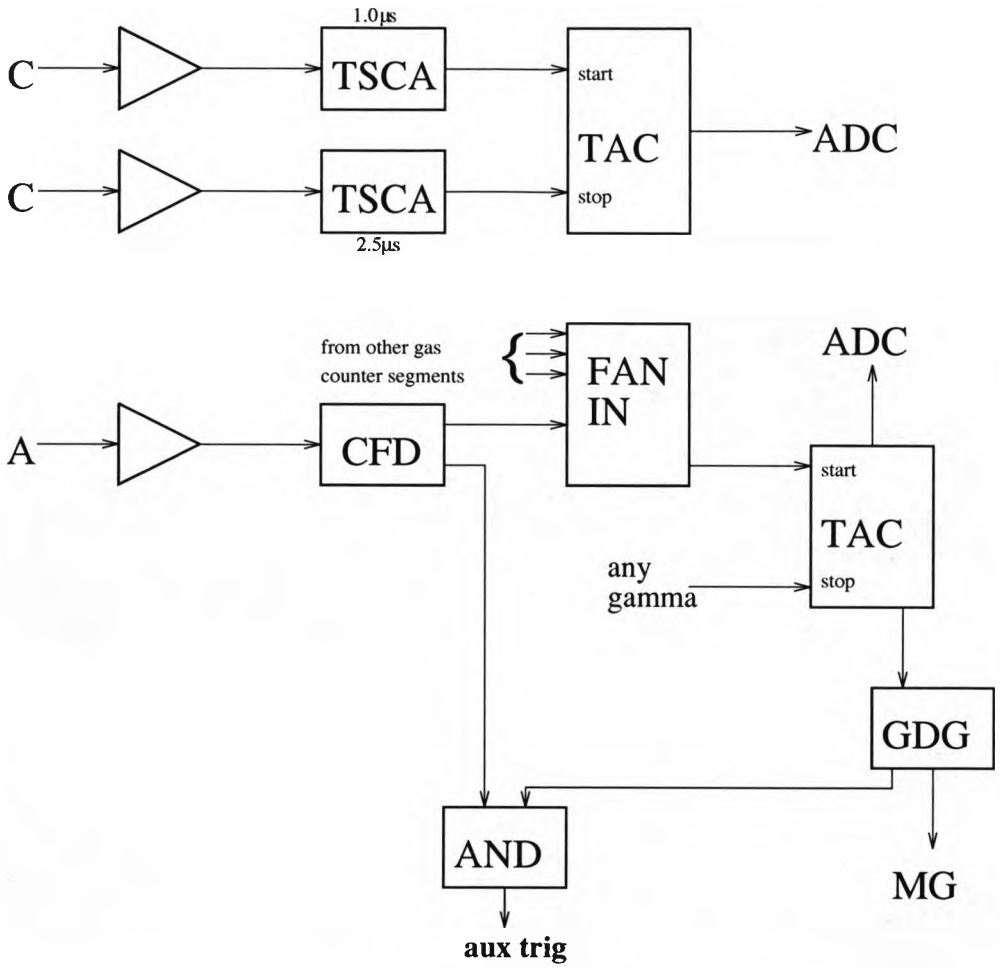

Figure 3.5: The electronic setup for the gas counter. The two ends of the delay line on the cathode (C) are used to start and stop a TAC to give the position, the pulse from the anode (A) was used to provide the trigger and the timing information.

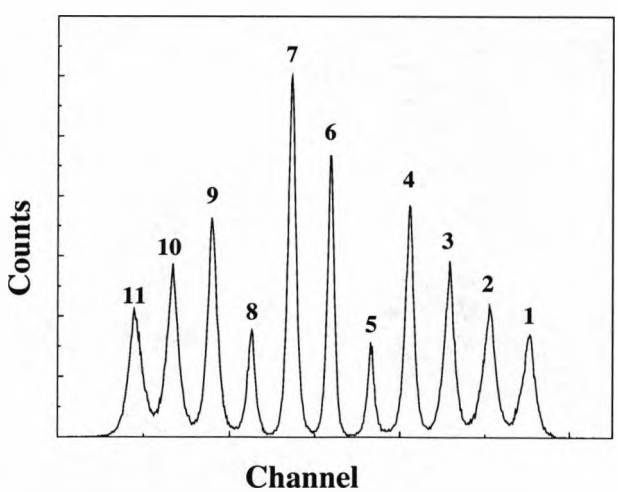

Figure 3.6: The position spectrum for one of the quadrants of the gas counter. The peaks corresponding to each of the 11 blobs shown in figure 3.2 are indicated.

3.3 The Data Analysis.

The first stage in the analysis of the data was to correct for the Doppler shift of the γ-rays detected by the array. The θ_g and ϕ_g of the γ-ray is known from the position of each of the Ge detectors. Working in spherical polar co-ordinates, and using the following kinematic equations, the direction and speed of the recoiling Pt nucleus can be found from the θ_s and ϕ_s of the scattered Ni particle detected in the gas counter.

$$\sin\theta_r = \sqrt{\frac{m_s X}{m_r(1-X)}}\sin\theta_s \tag{3.1}$$

$$\cos\theta_r = \sqrt{1-\sin^2\theta_r} \tag{3.2}$$

$$E_r = E_b(1-X) \tag{3.3}$$

$$v_r = \sqrt{\left(\frac{2E_r}{m_r}\right)\left(\frac{1.6}{1.67}\right)} \tag{3.4}$$

$$\phi_r = \phi_s \pm \pi \tag{3.5}$$

where E is the energy in MeV, the subscripts r, s, t and b refer to the recoil, scatter, target and beam respectively, with m the appropriate mass in atomic mass units. The factor 1.6/1.67 in equation(3.4) gives the velocity in units of 10^7 m/s. For the analysis of this experiment, $m_r = 194$, $m_s = 62$, $m_t = 195$, $m_b = 61$ and $E_b = 305$ MeV. The fraction of the beam energy taken up by the scattered particle, X, is given by;

$$X = B\left(\cos\theta_s + \sqrt{\frac{D}{B} - \sin^2\theta_s}\right)^2 \tag{3.6}$$

where the constants B and D are defined by;

$$B = \frac{m_b m_s}{(m_b+m_t)(m_r+m_s)}\frac{E_b}{E_b+Q} \tag{3.7}$$

$$D = \frac{m_t m_r}{(m_b+m_t)(m_r+m_s)}\left(1+\frac{m_b Q}{m_t(E_b+Q)}\right) \tag{3.8}$$

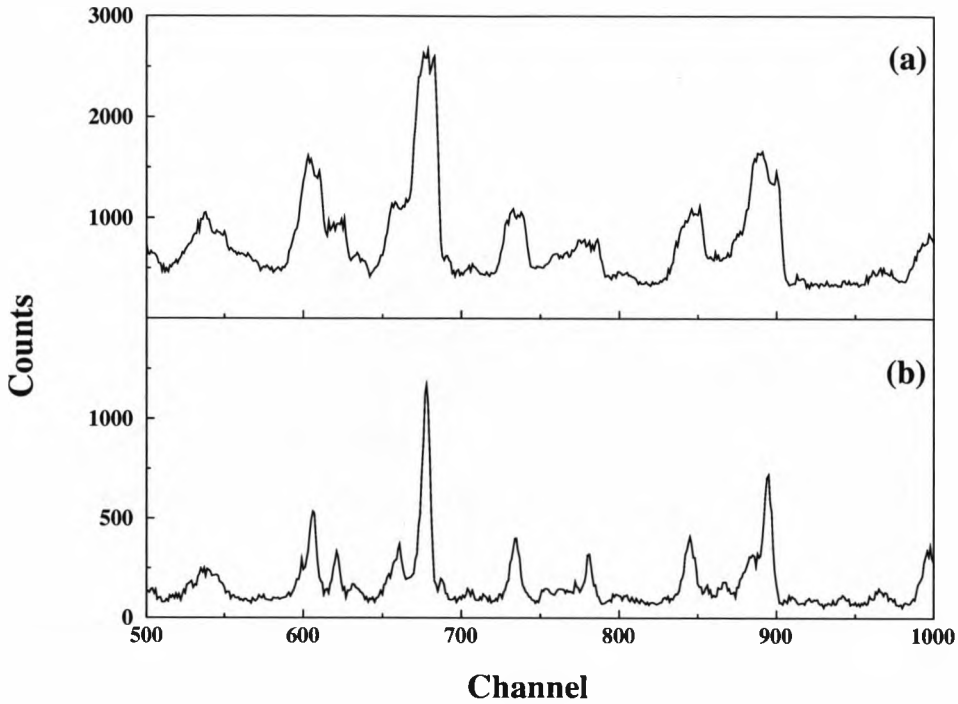

Figure 3.7: Sections of the spectra for one of the Ge detectors (a) before and (b) after the Doppler correction procedure. The channel numbers are not gainmatched, but are approximately $\frac{1}{2}$ keV per channel.

with Q the Q-value for the reaction, in this analysis taken to be zero, ie: assuming elastic scattering. And finally, the measured γ-ray energy ,E'_γ, is corrected to give the energy of the γ-ray in the rest frame of the recoiling nucleus, E_γ;

$$E_\gamma = \frac{E'_\gamma}{1 + (v_r \cos\omega)/c} \tag{3.9}$$

where ω is the angle between the recoil and the γ-ray, given by;

$$\cos\omega = \sin\theta_r \sin\theta_g(\cos\phi_r \cos\phi_g + \sin\phi_r \sin\phi_g) + \cos\theta_r \cos\theta_g \tag{3.10}$$

Figure 3.7 shows sections of the spectra for one of the Ge detectors before and after the Doppler correction procedure. The spectra have not been gainmatched. The correction for the Doppler shift of the γ-rays has reduced the width of the peaks to FWHM$\approx$ 6 keV at $E_\gamma = 500$ keV. The width of this peak arises from the acceptance angles of the Ge detectors, $\Delta\theta$. This results in an uncertainty in θ_g in equation (3.10) and hence an uncertainty in energy $\Delta E \propto \sin\theta_g \Delta\theta$. The Doppler corrected γ-rays were then gainmatched using calibration spectra from a Eu source.

Events with a backscattered Ni detected in coincidence with at least two γ-rays were sorted into a two dimensional E_γ–E_γ spectrum (or particle-γ-γ matrix). This matrix was formed by incrementing the positions (E_{γ_1},E_{γ_2}) and (E_{γ_2},E_{γ_1}) in the matrix, where E_{γ_1} and E_{γ_2} are the energies of two coincident γ-rays. Higher fold events, with three or more γ-rays, were sorted into this matrix by unfolding all the γ-γ combinations of the event, eg: an event with three γ-rays with energies E_{γ_1}, E_{γ_2} and E_{γ_3} has three γ-γ pairs, (E_{γ_1},E_{γ_2}), (E_{γ_1},E_{γ_3}) and (E_{γ_2},E_{γ_3}). The result is a two dimensional matrix with the x- and y-axes being γ-ray energies containing the number of counts.

Nuclear level schemes were constructed by analysing this matrix. A peak is defined by a pair of limits (a "gate") on one axis, and the spectrum corresponding to the γ-rays in coincidence with this gate is given by the projection of the matrix on the other axis. Background regions defined by limits where there are no peaks are subtracted from the resultant spectrum. Setting many gates on the matrix allows one to determine which γ-rays are in coincidence with each other, and hence construct the decay scheme of the nucleus.

The computer code ASAP[28] was used on this matrix to look for a superdeformed band. This utilizes the fact that rotational bands have a regular structure. The γ-ray energies are equally spaced, with the spacing dependent on the moment of inertia, and hence deformation, of the nucleus. The program searches the matrix for regular spaced peaks with the energy separation that would correspond to a superdeformed band.

3.4 Results.

The matrix contained 2.5 M particle-γ-γ events. The total projection of this matrix is shown in figure 3.8. The transitions in the three isotopes populated are indicated.

Gates were set on this matrix to study the decay schemes of these nuclei. Figure 3.9 shows a selection of the spectra produced by gates set on ^{194}Pt transitions. Spectrum (a) is produced by the gate on the 328 keV $2^+ \rightarrow 0^+$ ground state band transition. The γ-rays seen here are from the ground state band, γ-vibrational band

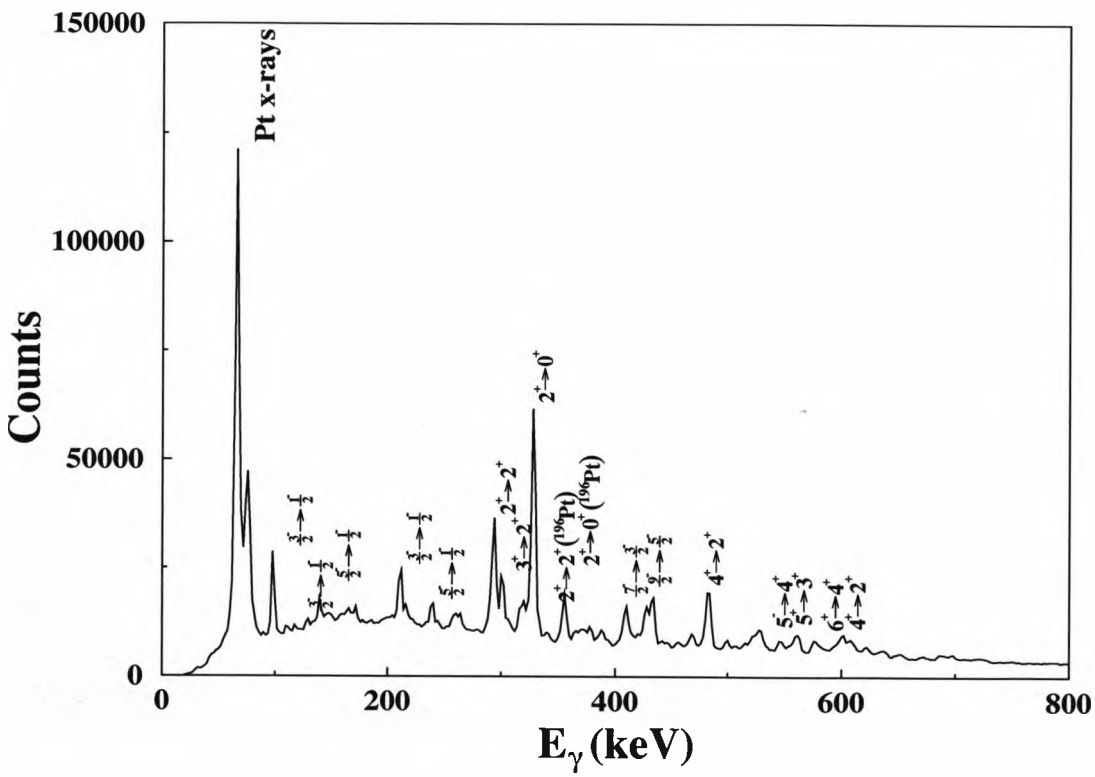

Figure 3.8: Total projection of the p-γ-γ matrix for the Pt data. The transitions with half integer spin are in ^{195}Pt. The transitions with integral spin are in ^{194}Pt except for two transitions which are in ^{196}Pt.

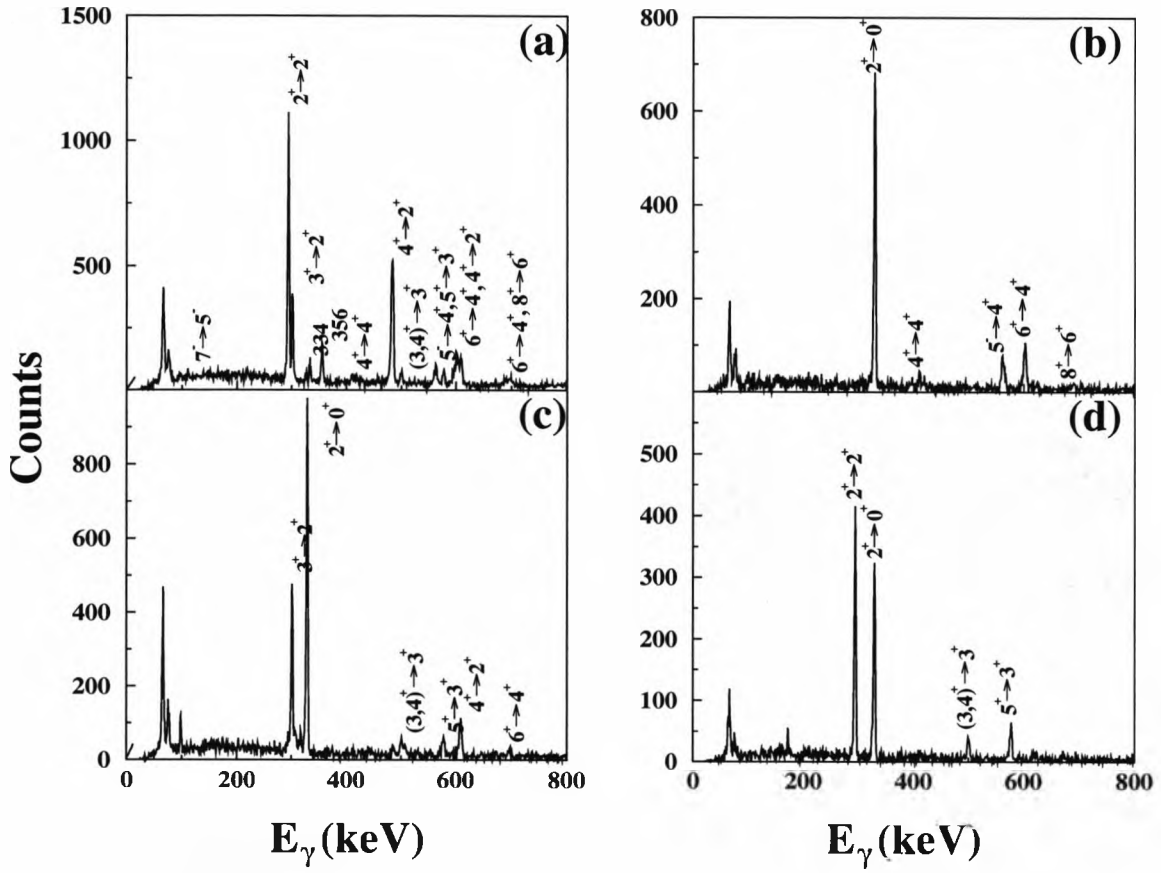

Figure 3.9: Spectra produced by gates on ^{194}Pt transitions. The gates are (a) the 328 keV $2^+ \rightarrow 0^+$ ground state band transition, (b) the 483 keV $4^+ \rightarrow 2^+$ ground state band transition, (c) the 294 keV $2^+ \rightarrow 2^+$ γ-vibrational to ground state band transition and (d) the 301 keV $3^+ \rightarrow 2^+$ γ-vibrational band transition. The 334 keV and 356 keV transitions are contaminants from ^{196}Pt.

and a negative parity band based on a 5^- state (the 334 keV and 356 keV transitions are contaminants from ^{196}Pt). Spectrum (b) is produced by the gate on the 483 keV $4^+ \rightarrow 2^+$ ground state band transition and shows transitions in the ground state band, the negative parity band and some of the γ-vibrational band. Spectrum (c) is produced by the gate on the 294 keV $2^+ \rightarrow 2^+$ γ-vibrational to ground state band transition and shows transitions within the γ-vibrational band and the 328 keV $2^+ \rightarrow 0^+$ ground state band transition. Spectrum (d) is produced by the gate on the 301 keV $3^+ \rightarrow 2^+$ γ-vibrational band transition and shows transitions within the γ-vibrational band.

The decay scheme deduced from these and other gates is shown in figure 3.10. All these transitions have been observed previously[29].

Figure 3.11 shows the spectrum produced by a gate set on the 356 keV $2^+ \rightarrow 0^+$

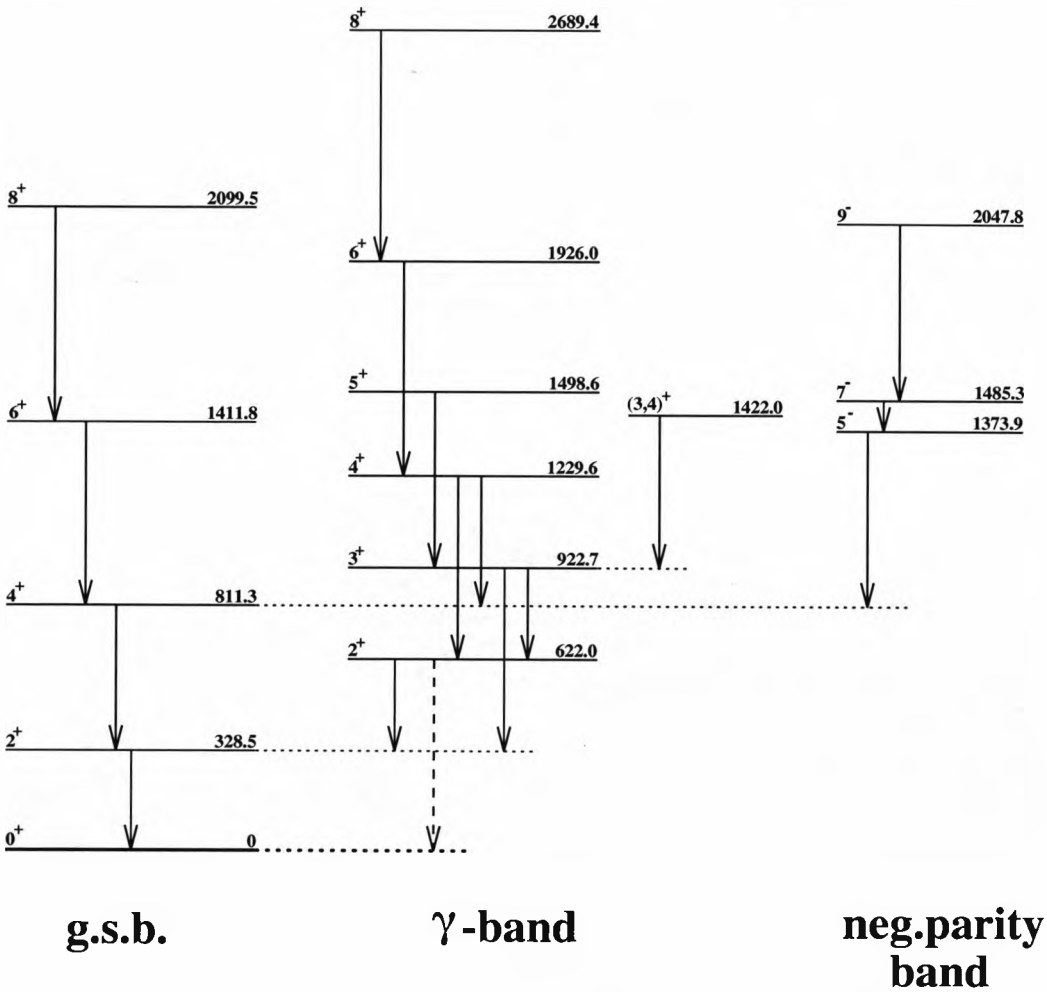

Figure 3.10: Level scheme of ^{194}Pt as observed in this experiment. The 622 keV (shown with a dashed arrow) transition was observed very weakly. All these transitions had been previously observed[29].

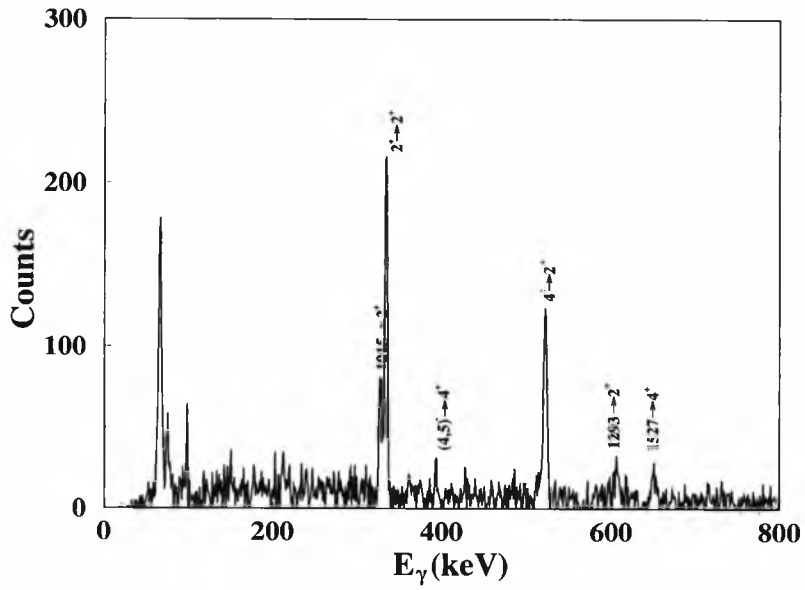

Figure 3.11: Spectrum produced by the gate on the 356 keV $2^+ \rightarrow 0^+$ transition in ^{196}Pt.

transition in ^{196}Pt. The decay scheme deduced for this nucleus is shown in figure 3.12. These transitions have also been observed previously[30].

In this experiment the ground state band of ^{194}Pt was populated up to spin 8^+ at an excitation energy of 2.1 MeV. Coulomb excitation experiments had previously populated the ground state band up to spin 10^+[29]. The γ-vibrational band was also populated to spin 8^+ at an excitation energy of 2.7 MeV (as high as it had previously been observed) and the negative parity band to spin 9^- at 2.0 MeV (it had previously been observed to spin 11^-). There is no evidence that a superdeformed band was populated in ^{194}Pt.

3.5 Discussion.

This experiment failed to populate a superdeformed band in ^{194}Pt. There could be several reasons for this failure. The first could be that the theoretical predictions are wrong, and that there is no superdeformed band in this nucleus. Alternatively, if there is a superdeformed band in ^{194}Pt then the reaction mechanism has not populated the superdeformed band with sufficient intensity to be able to detect it, if at all.

There were two proposed population mechanisms. The first of these required that the transfer reaction give the residual nucleus sufficient angular momentum to form

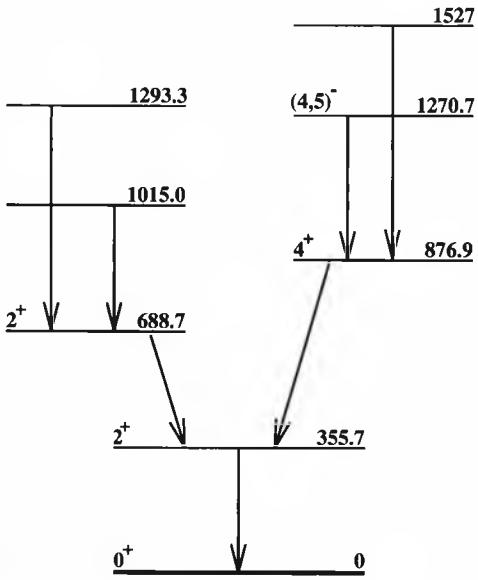

Figure 3.12: Level scheme of ^{196}Pt as observed in this experiment. These transitions have all been previously observed[30].

the nucleus near the region where the superdeformed band becomes yrast, at spin $\sim$ 30 $\hbar$. In this region it was hoped that the superdeformed band could then be directly populated since it lies in the window of states that HITR are expected to populate. However, the experiment only populated states upto spin 8^+ in ^{194}Pt, and that would have included some Coulomb excitation of the residual nucleus. It seems unlikely that the residual nucleus was populated with sufficient angular momentum for there to have been any significant overlap with the superdeformed band.

The other mechanism required the population of the residual nucleus at lower spin near the point where the superdeformed band feeds into the ground state band. It was hoped that in this region the wavefunction of the superdeformed band is a mixture of superdeformed and normal deformed wavefunctions. If the residual nucleus was left in a region where these wavefunctions mixed then it was hoped that the superdeformed component would be preferentially Coulomb excited because the large deformation would result in much larger values of B(E2). Since the experiment failed to populate a superdeformed band this would imply that either the superdeformed wavefunction is not a mixture of superdeformed and normal deformed wavefunctions, or that the mixing is very weak, and so the transfer does not populate the superdeformed band with sufficient intensity to be able to detect it. A final possibility is that the transfer

reaction does not provide enough excitation energy or spin to the residual nucleus for the transfer to leave it in the region where the wavefunctions mix. Indeed, the measured excitation energy of ^{194}Pt is $\leq$ 3 MeV, which is lower than the expected excitation of the superdeformed "band head".

There are some further experiments which may be considered to try to overcome some of these problems. If the problem is that the superdeformed band is there, but just too weak to be observed then better statistics would be needed. This could be achieved by the use of an improved gas counter, covering a larger solid angle and with less dead time, allowing the use of a more intense beam. More statistics could also be achieved by the use of a larger, more efficient Ge array, such as EUROGAM.

If the problem is one of insufficient excitation energy in the system there are other reactions that could be used, for example the ^{195}Pt(^{87}Sr,^{88}Sr)^{194}Pt (Q_{gg} = 5.0 MeV) or ^{195}Pt(^{47}Ti,^{48}Ti)^{194}Pt (Q_{gg} = 5.5 MeV) reactions. These reactions would provide more excitation energy to the residual nucleus, and the Sr reaction would also provide more spin. Both these reactions would also have no contamination from ^{196}Pt.

Since all known superdeformed bands have been populated using compound nucleus reactions they are all in neutron deficient nuclei. Since these nuclei are all more than one neutron away from the lightest stable isotopes one neutron transfer reactions can not be used to try and populate these known superdeformed bands. It is, however, possible to populate nuclei known to have superdeformed bands by proton and multi-nucleon transfer. For example, the ^{192}Pt(^{16}O,^{14}C)^{194}Hg two proton stripping reaction has been used to try to populate the known superdeformed band in ^{194}Hg[23].

Chapter 4

Attempt to Populate Fission Isomers in Pu Nuclei.

4.1 Introduction.

Fission isomers have previously been populated using light ion induced reactions, typically with cross sections of a few μb[12]. It is hoped to utilize the properties of Heavy Ion-induced Transfer Reactions (HITR) to enhance the population of the (0^+, $T_{\frac{1}{2}}$ = 0.5 ns, E_x = 2.4 MeV) fission isomer in ^{238}Pu, which has previously been populated using the ^{236}U(α,2n)^{238}Pu reaction[31]. The reaction used was ^{239}Pu(^{117}Sn,^{118}Sn)^{238}Pu at a beam energy of 630 MeV. For this reaction the ground state Q-value, Q_{gg} = 3.7 MeV.

Previous HITR experiments in this region using the ^{235}U(^{58}Ni,^{59}Ni)^{234}U[9] and ^{235}U(^{206}Pb,^{207}Pb)^{234}U[10] reactions have populated ^{234}U to spin $\sim$ 30. Plots of total energy against multiplicity were produced, figure 4.1 shows the plot for the ^{235}U(^{58}Ni,^{59}Ni)^{234}U reaction taken from reference[9]. These plots showed two peaks, corresponding to direct population of the ground state and the population of aligned two quasiparticle states.

The γ-ray spectroscopy from this experiment was analysed separately and is presented in reference[32]. The study of the fission of the residual nucleus is presented here and in reference[33].

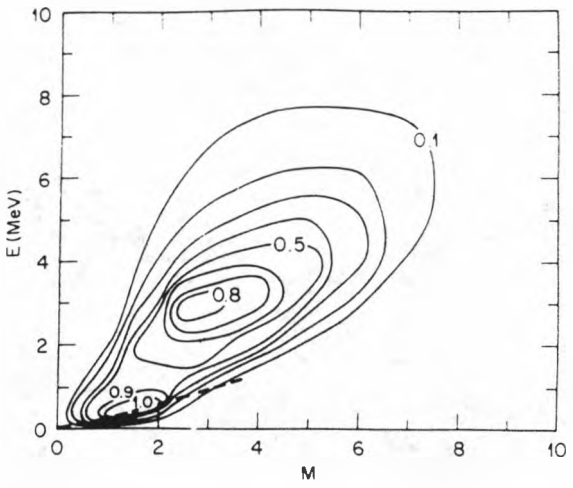

Figure 4.1: Plot of total energy against multiplicity for the ^{235}U(^{58}Ni,^{59}Ni)^{234}U reaction. The dashed line is the approximate yrast line for ^{234}U. Taken from reference[9].

4.2 Experimental Details.

The experiment was conducted at the Oak Ridge Holifield Heavy Ion Research Facility using a large solid angle arrangement of position-sensitive parallel-plate avalanche detectors surrounded by the Spin Spectrometer 4π γ-ray detector array. The Rochester position-sensitive particle detector system comprised an annular backscatter detector, covering particle angles $118° < \theta < 156°$ and 300° in ϕ, coupled to a forward angle conical array of six detectors covering an angular range $15° < \theta < 76°$ and 300° in ϕ. Figure 4.2 shows a schematic arrangement of this detector. The forward angle detector measured the particle angles with an uncertainty of $\Delta\theta = 1°$ and $\Delta\phi = 10°$ while the angular uncertainty for the backscatter detector was $\Delta\theta = 2°$ and $\Delta\phi = 50°$. The intrinsic time resolution of the particle detectors was < 1 ns but this was degraded to $\sim$ 2 ns due to target effects. This detector system was used to detect the scattered Sn ion in the back and two fission fragments in the front. The coincident de-excitation γ-rays were investigated using the Spin Spectrometer which comprised 45 NaI detectors plus 18 Compton-suppressed Ge detectors[34]. The summed energy and observed multiplicity information derived from the NaI detectors is presented in reference[32].

Figure 4.3 shows the arrangement of the electronics for the particle detectors. The cathodes for the front detectors act as delay lines, and signals are taken from them at

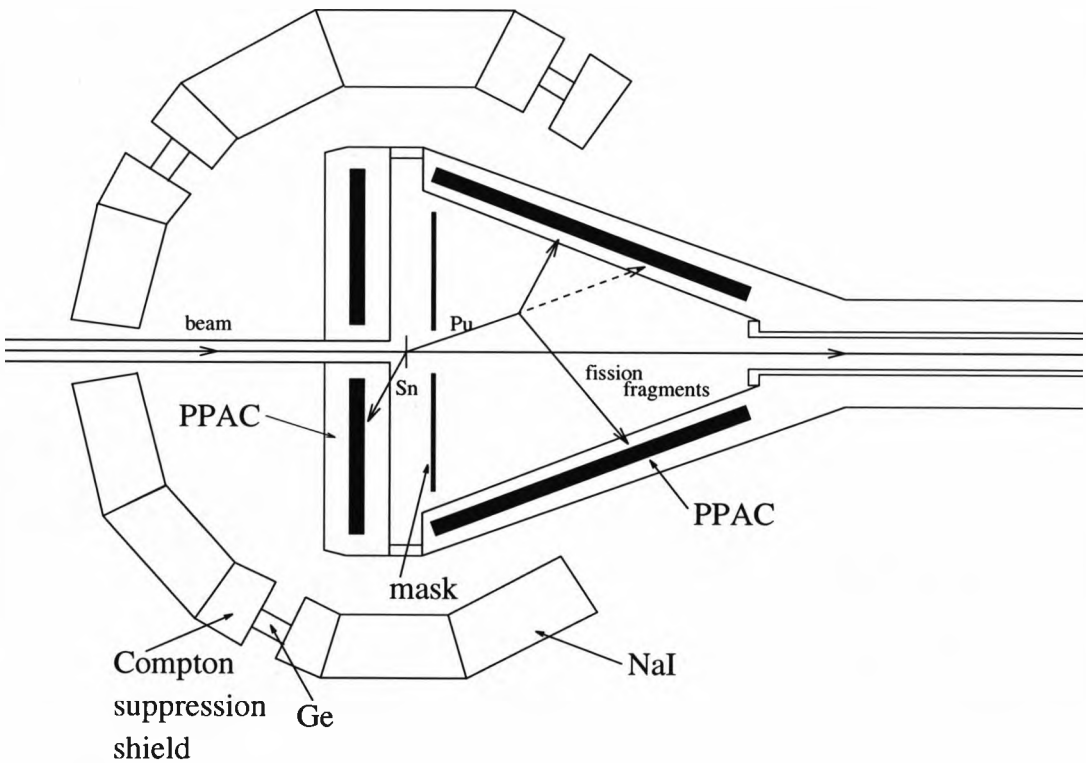

Figure 4.2: Diagram of the detector system used in this experiment. This consists of position-sensitive parallel-plate avalanche counters (PPAC's) in the forward and backward angles within the Spin Spectrometer array of NaI and Compton-suppressed Ge detectors.

10° and 76°. These signals are amplified, passed through a discriminator and delayed by 360 ns and fed into a time to digital converter (TDC). The difference between the times for signals from the 10° and 76° ends of the cathode gives the θ of the forward going particle. Similarly, the cathode of the back detector has signals from the inside and outside of the ring. The time difference between these two signals gives the θ of the back scattered particle.

The signals from the 3 sections of each of the front anodes were amplified and passed through a discriminator. These signals were then fed into a multiplicity logic unit (MALU) which gave an output if more than one front detector fired, this was used as a signal that two forward going particles had been detected. The output from the discriminator was also delayed and fed into a coincidence register (CR) to define which anode section(s) fired, which defines the ϕ of the particle. The 3 signals from each anode were also fed into an OR gate and then a TDC to give the time that each front particle was detected. The signals from the six sections of the back anode were passed through a discriminator, delayed by 380 ns and fed into a coincidence register which defined which section fired, and hence the ϕ of the back scattered particle. The sum output of the discriminator was used as a signal that a back scattered particle had been detected.

The signals for the detection of a back scattered particle and two forward going particles were fed into an AND gate, giving a signal if 3 particles were detected. This was fed into a coincidence register as a fission bit. The signal from the back detector was fed into a TDC to give the time for the detection of the back counter, and was scaled down by a factor of 10 to give a scaled down singles bit used to normalize to the total cross section. It was also fed into an AND gate with a signal from the Spin Spectrometer electronics indicating the detection of at least one γ-ray. This generated a back scattered particle-γ signal.

The event OR gate provided the master gate and the TDC strobe used to define time zero for the TDC's. These were provided for fission events (2 forward going and one back scattered particles), back scattered particle-γ events and scaled down back scattered singles. The delays in the electronics before the coincidence registers and TDC ensured that these signals arrived after the TDC strobe.

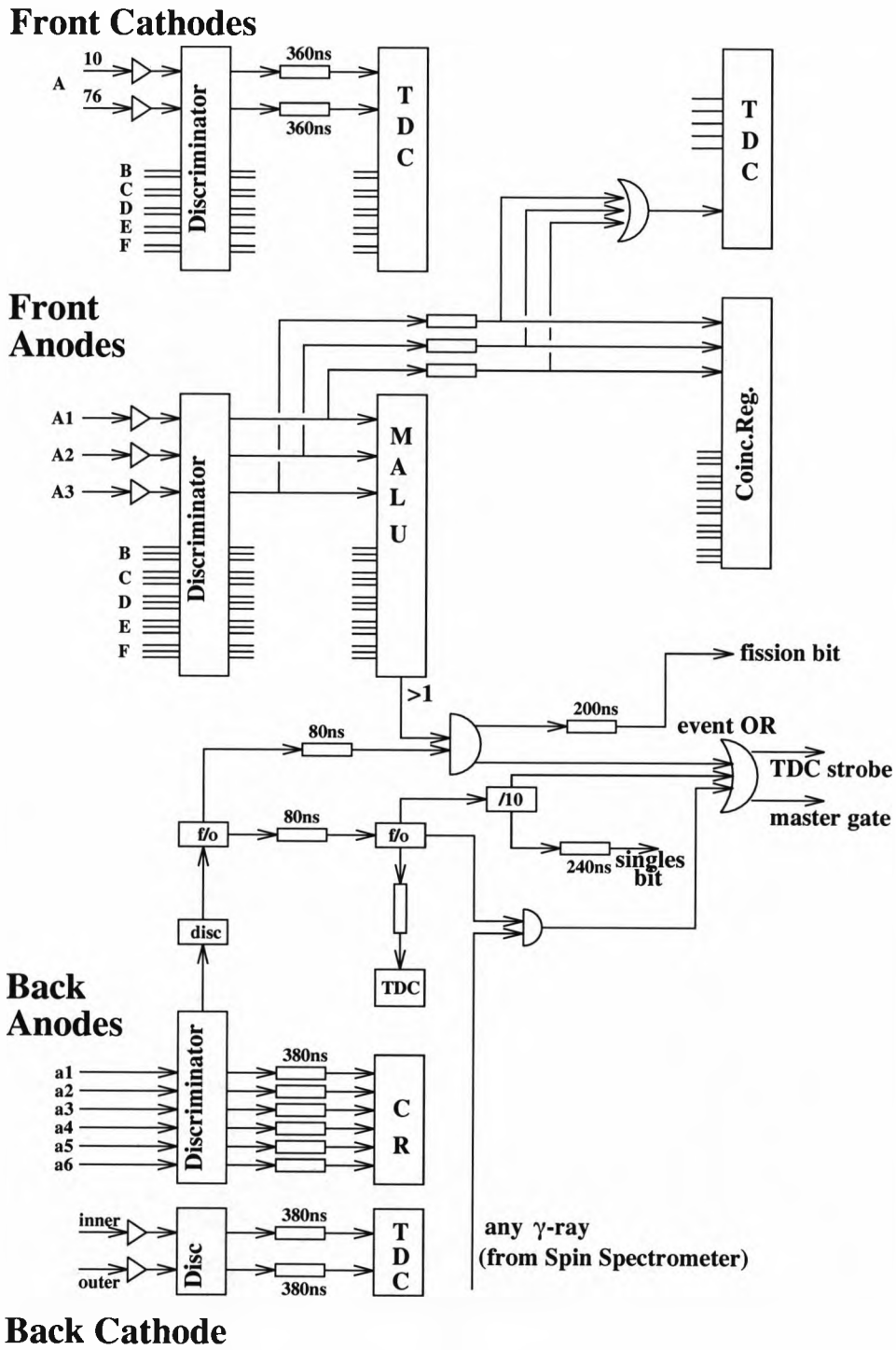

Figure 4.3: Diagram of the electronics for the particle detectors. The cathodes are connected to a delay line, the ends of which are read at 10° and 76° (front) and the inner and outer sides of the ring (back) into TDCs. The difference between the times of the two signals defines θ. The outputs from the anodes define ϕ. They also provide the signals indicating a back scattered particle or two forward going particles. A signal from the Spin Spectrometer electronics gives the any-γ signal. The master gate and TDC strobe are given by fission events (2 forward going and one back scattered particles), scaled down back scattered particles, or back scattered particle-γ.

The ADC's, TDC's and coincidence registers for the Spin Spectrometer and PPAC's were interfaced with the on-line computer (a Perkin-Elmer 32/20) through a CAMAC system. The Event Handler, a pre-programmable CAMAC-based controller, manages the data acquisition system. The data is written on to magnetic tape for permanent storage.

The beam of typically 20 nA 630 MeV ^{117}Sn was incident on a target of 295 μg/cm^2 of 99.967% enriched $^{239}PuO_2$ on a 3.39 mg/cm^2 Ni backing (placed downstream) produced by electrodeposition of the Pu onto the Ni as described in reference[35]. This thick backing was used to increase the detection efficiency for delayed fission by slowing down the Pu recoils.

A mask, consisting of a 3.5 mg/cm^2 piece of flat stainless steel with a 3.63 mm diameter aperture, was place 5 mm downstream of the target, the aperture being carefully aligned with the beam. This mask limited the angular range of the detection of prompt fission fragments emitted from the target to $\theta < 20°$, effectively eliminating the possibility of detecting two such fragments simultaneously. Recoiling nuclei that decayed with a flight time > 0.25 ns travelled beyond the mask before fission occurred, and thus the detection of the fission products was limited only by the solid angle of the forward particle detector. The mask could be inserted and removed without disturbing any detectors.

The experiment was run in two parts. The first part of the experiment was run with no mask, the "mask out" data, studying the prompt fission events. The second part of the experiment was run with the mask, the "mask in" data, studying delayed fission.

4.3 Analysis of Data.

A valid coincidence event was one in which three particles were detected, one in the backward annular detector and two in the forward detectors.

The θ_s and ϕ_s of the backwards scattered Sn nucleus were used to determine the θ_r, ϕ_r and energy E_r of the recoiling Pu nucleus, using the same kinematic equations given earlier for the Pt experiment (equations(3.1)–(3.8)) with $m_t = 239$, $m_b = 117$,

$m_r = 238$, $m_s = 118$ and $E_b = 630$ MeV.

Events where the two fragment directions and the recoil direction were not coplanar within the acceptance of the backward annular detector were rejected. Coplanar events must satisfy the relationship;

$$\cot\theta_2 \sin(\phi_1 - \phi_r) + \cot\theta_1 \sin(\phi_r - \phi_2) - \cot\theta_r \sin(\phi_1 - \phi_2) = 0 \qquad (4.1)$$

Events where $\mid \cot\theta_r \sin(\phi_1 - \phi_2) \mid > \mid \cot\theta_2 \mid + \mid \cot\theta_1 \mid$ are not coplanar as relationship (4.1) can not then be satisfied, and are rejected. The θ and ϕ of the two particles in the front detectors were then used to determine the ϕ_r of the recoiling Pu nucleus to greater accuracy than determined by the backward detector, thus reducing errors in the analysis. This was achieved by varying ϕ_r to minimize $\mid \cot\theta_2 \sin(\phi_1 - \phi_r) + \cot\theta_1 \sin(\phi_r - \phi_2) - \cot\theta_r \sin(\phi_1 - \phi_2) \mid$.

The time difference, $T_{1,2}$, between the forward and backward detectors with an arbitary offset was also measured. The offset was determined by separately detecting Sn backscatters in coincidence with one particle in the front detectors. Such two body events were assumed to be largely due to elastic scattering with no fission. The kinematics of elastic scattering are known, and so the timing signals can be calibrated.

For three body events, the timing signals and the known geometry of the detectors were used to determine the velocity, and hence energy per unit mass, of the two fission fragments. The geometry of one of the front detectors is shown schematically in figure 4.4. The normal to the plane is at an angle of 75° to the beam direction, and the plane of the detector is 7.5 cm from the target at the closest point. The angle ϕ_{diff} is the difference between the ϕ of the normal to the plane and the ϕ of the section of the detector that the fragment hits. The distance between the target and the point of the detector where the first fragment was detected, b_1 in units of cm, is given by;

$$b_1 = \frac{7.5}{\cos\phi_{diff} \cos(75 - \theta_1)} \qquad (4.2)$$

where θ_1 is given in degrees. If T_1 is measured in units of ns then the velocity in units of 10^7 m/s is given by;

$$v_1 = b_1/T_1 \qquad (4.3)$$

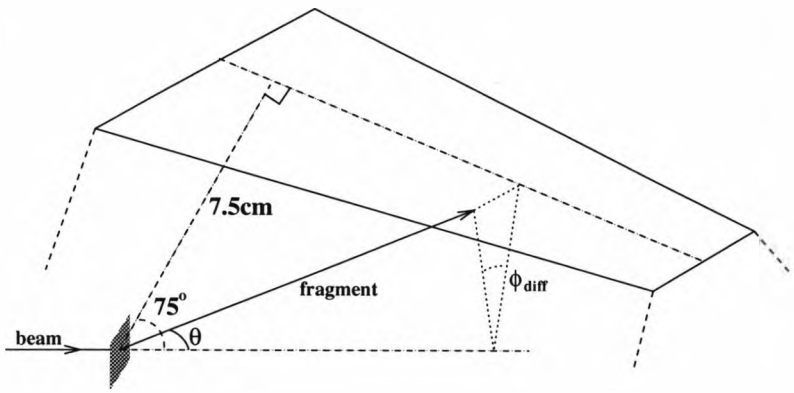

Figure 4.4: The geometry of one of the forward detectors. The normal to the plane is at an angle of 75° to the beam direction, and the plane is 7.5 cm from the target at the closest point. The angle ϕ_{diff} is the difference between the ϕ of the normal to the plane and the ϕ of the section of the counter that the fragment hits.

Then the energy per atomic mass unit in MeV is;

$$E_1 = \tfrac{1}{2}v_1^2(1.67/1.6) \tag{4.4}$$

This is repeated for the second fragment, giving v_2 and E_2.

For the first part of the data analysis, looking at the prompt fission events from the mask out data, the measured energy per unit mass of the fragments was corrected to account for the fragment having passed through the thick Ni backing. This was done by using the range of ions of different energies per atomic mass unit in Ni from Northcliffe and Schilling[36]. It is seen that all nuclei in the mass range 40–200 have approximately the same range for the same energy, and the range follows an approximate straight line shown in figure 4.5, with;

$$R \simeq mE + c \tag{4.5}$$

where $m = 3.15$ and $c = 2.5$ for the range in units of mg/cm^2. This number was adjusted to fit the experimental data to give the total mass as 238 and $\theta_{cm} = 180°$ in equations (4.17)–(4.14), the best fit being $m = 1.50$. That is, the experimentally observed ranges of the fragments is approximately 30% that given by the values in Northcliffe and Schilling. Given the final measured energy E_f it is found that the range for the fragment, having passed through the backing is;

$$R_f = mE_f + c \tag{4.6}$$

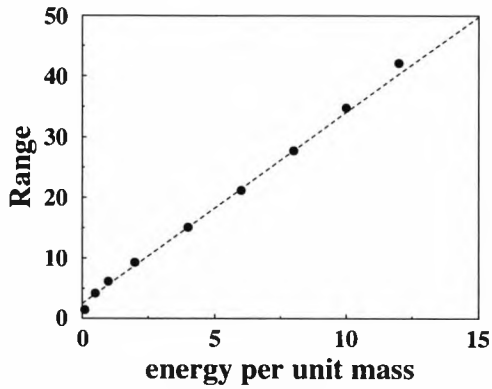

Figure 4.5: The range of ions of different masses in Ni against energy per atomic mass unit. The dashed line is a fit of $R \simeq mE + c$ with $m = 3.15$ and $c = 2.5$.

It is known that the fragment has travelled through a distance $t = 3.39/\cos\theta$ of Ni backing, in units of mg/cm^2, so the initial range;

$$R_i = R_f + t \tag{4.7}$$

Hence the initial energy and velocity are;

$$E_i = E_f + t/m \tag{4.8}$$

$$v_i = \sqrt{2E_i(1.6/1.67)} \tag{4.9}$$

For the second part of the experiment, looking at delayed fission from the mask in data, the correction was made for the slowing of the Pu recoil in the backing by using the ranges for Pu in Ni from Northcliffe and Schilling but using the known initial velocity to give the reduced velocity of the recoil when it fissions. An error of 30% was allowed in these ranges.

The velocity (speed and direction) of both fragments in the laboratory frame at the point of fission is then known. The angle between the two fragments in the centre of mass frame (θ_{cm}), the masses of the fragments ($m_{1,2}$) and the total kinetic energy of the two fragments in the centre of mass (E_{cm}) can now be found.

The angle between the first fission fragment and the direction of the recoiling Pu nucleus in the centre of mass, θ_{cm1}, is given by;

$$\cos\theta_{cm1} = \frac{v_1 \cos\theta_{f1} - v_r}{v_1'} \tag{4.10}$$

where v_1 is the speed of the fragment and v_r the speed of the recoiling Pu in the laboratory frame at fission. This is before the Pu has passed through the backing for the mask out data, and after for the mask in data. v_1' is the speed of the fragment in the centre of mass and θ_{f1} is the angle between the fission fragment and the recoil in the laboratory frame at the point of fission. For delayed fission where the recoil has travelled a distance d_r, the fragment travels a distance c_1 between the point of fission and the detector.

$$c_1 = \sqrt{d_r^2 + b_1^2 - 2d_r b_1 \cos\theta_{r1}} \tag{4.11}$$

the angle θ_{f1} is then given by;

$$\sin\theta_{f1} = \frac{b_1 \sin\theta_{r1}}{c_1} \tag{4.12}$$

For prompt fission, $\theta_{f1} = \theta_{r1}$, where θ_{r1} is the laboratory angle between the direction of the Pu recoil and the vector from the target to the detector.

$$\cos\theta_{r1} = \sin\theta_1 \sin\theta_r \cos(\phi_1 - \phi_r) + \cos\theta_1 \cos\theta_r \tag{4.13}$$

Similarly for the second fragment the procedure is repeated, giving θ_{cm2}. Then the centre of mass angle for the fission;

$$\theta_{cm} = \theta_{cm1} + \theta_{cm2} \tag{4.14}$$

The fragment masses are then given by;

$$m_1 = \frac{m_r v_r}{v_1 \cos\theta_{r1} + (\sin\theta_{r1}/\tan\theta_{r2})} \tag{4.15}$$

$$m_2 = \frac{m_r v_r}{v_2 \cos\theta_{r2} + (\sin\theta_{r2}/\tan\theta_{r1})} \tag{4.16}$$

And the total mass;

$$m_{tot} = m_1 + m_2 \tag{4.17}$$

Finally, the total kinetic energy of the two fragments in the centre of mass in units of MeV is simply;

$$E_{cm} = (\tfrac{1}{2}m_1v_1^2 + \tfrac{1}{2}m_2v_2^2 - \tfrac{1}{2}m_rv_r^2)(1.67/1.6) \tag{4.18}$$

Genuine fission events should have $\theta_{cm} \approx 180°$, $m_{tot} = 238$ and $E_{cm} \approx 180$ MeV. To aid in the analysis of the data a Monte Carlo simulation was used.

4.3.1 The Monte Carlo Simulation.

The Monte Carlo Simulation was first written to show whether the experimental setup, with mask, would be capable of detecting and identifying delayed fission events. The code accounted for the slowing down of fission fragments (for prompt fission) or the recoiling Pu nucleus (for delayed fission) using values for $\frac{dE}{dx}$ derived from Northcliffe and Schilling[36]. It assumed Rutherford scattering of the Sn and Pu, and that $\frac{d\sigma}{d\Omega}$ for fission has a $\frac{1}{\sin\theta}$ distribution in the centre of mass with respect to the recoil direction. It also assumed a Gaussian mass distribution (terminated after two standard deviations), for prompt fission this was assumed to be symmetric and for delayed fission asymmetric. These were chosen following studies of ^{4}He induced reactions at high energies that produce prompt fission with a symmetric mass distribution and observations that isomeric fission is similar to spontaneous fission of the ground state[37] which has an asymmetric mass distribution. It also assumed that no mass was lost in fission, and that there was a finite beam spot with a Gaussian profile. A random lifetime of delayed fissions (weighted with the appropriate exponential) was assumed.

The program was also used to find the efficiency of the detector system for detecting fission events (ie: whether both fragments are detected). For the mass distributions given above the detection efficiencies were $(57.8 \pm 0.3)\%$ for prompt fission with the mask removed and $(55.6 \pm 0.3)\%$ for delayed fission of the 0.5 ns isomer with the mask in place. The efficiency calculated for other mass distributions and for an isotropic $\frac{d\sigma}{d\Omega}$ distribution in the centre of mass produced changes in the efficiency of less than 2%.

The program was modified to aid the analysis of the data so that it would produce various characteristics of fission events, which could then be compared with the results generated from the actual data. The program generated values for θ, ϕ and time for

the detectors in the forward and backward directions. Two dimensional plots of θ_1 vs θ_2, T_1 vs T_2 and $(T_1 - T_2)$ vs $(\theta_1 + \theta_2)$ with the mask in place (for both prompt and delayed fission) and with no mask (prompt fission only) were produced. These are shown in figure 4.6.

It can be seen from these plots that if delayed fission events occur then it should be possible to identify them. It can be seen that events with $\theta > 20°$ cannot be prompt fission as these would not pass the mask; however these must be distinguished from any other possible event such as prompt fragments, recoiling Pu nuclei or Sn nuclei scattering off the edge of the mask or random firing of the gas counter sections. It is hoped that finding the kinematic information about the events (mass, angle in the centre of mass, and energy in the centre of mass) and gating on the timing and angle information that any random events can be eliminated.

The values for the θ and ϕ of the backscattered Sn and the two fission fragments and the time of flight of each fragment produced by the simulation were then used as the input into an analysis routine that carried out the same procedure as would be used on the actual data. This successfully recreated the values input into the simulation, showing that the analysis procedure would work. These are seen in figure 4.7, which is for prompt events with $m = 3.15$ for the calculation of the slowing of the fragments in the backing (equation (4.8)). The value for m is different from that found experimentally because the slowing of the fragments in the simulation used theoretical values of $\frac{dE}{dx}$, so it is to be expected that the value for m which gives the best fit for the simulation should be the same as the value given by Northcliffe and Schilling[36].

Figure 4.8 shows the results of the Monte Carlo simulation for delayed fission events. These are calculated using the fission time input into the Monte Carlo simulation to give the fission point.

It is found that varying the fission time (and hence recoil distance) has no effect on the centre of mass angle for the fission and very little effect on the total mass. It is found however that varying the recoil time does change the energy in the centre of mass and the individual masses of the two fragments. So in the actual data analysis, for simplicity, the calculations assumed no recoil distance, so this was also done for

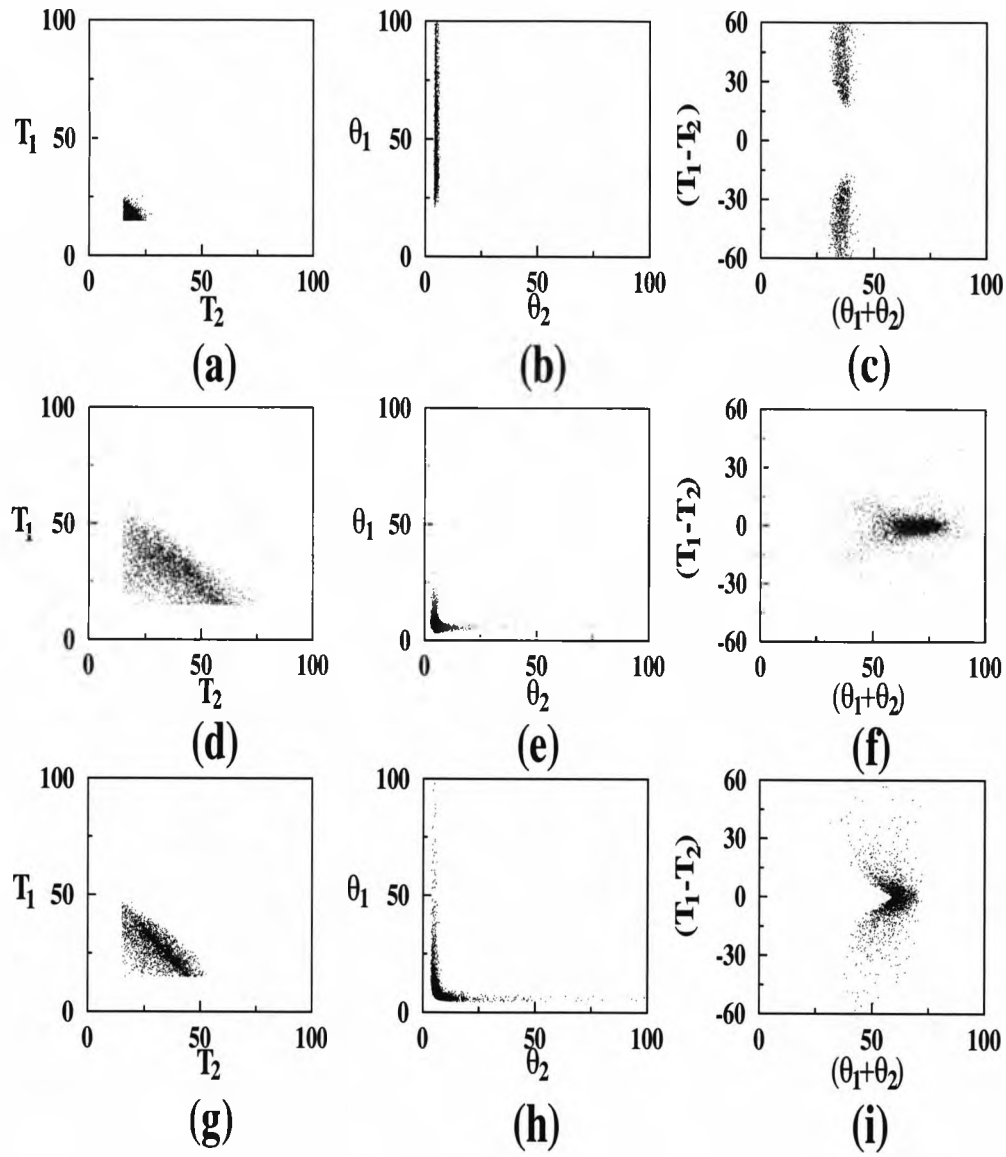

Figure 4.6: Monte Carlo calculations showing plots of θ_1 vs θ_2, T_1 vs T_2 and $(T_1 - T_2)$ vs $(\theta_1 + \theta_2)$ for prompt fission events with the mask in place ((a), (b) and (c)), delayed fission events with the mask in place ((d), (e) and (f)), prompt fission events without the mask ((g), (h) and (i)). The angles are in degrees and the times in nanoseconds.

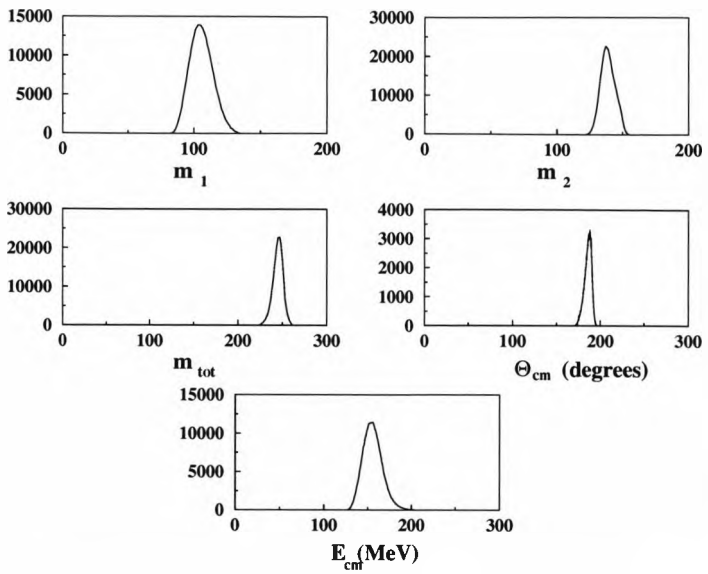

Figure 4.7: Output of the analysis procedure for prompt fission of Pu using values of θ, ϕ and time given by the Monte Carlo simulation without the mask.

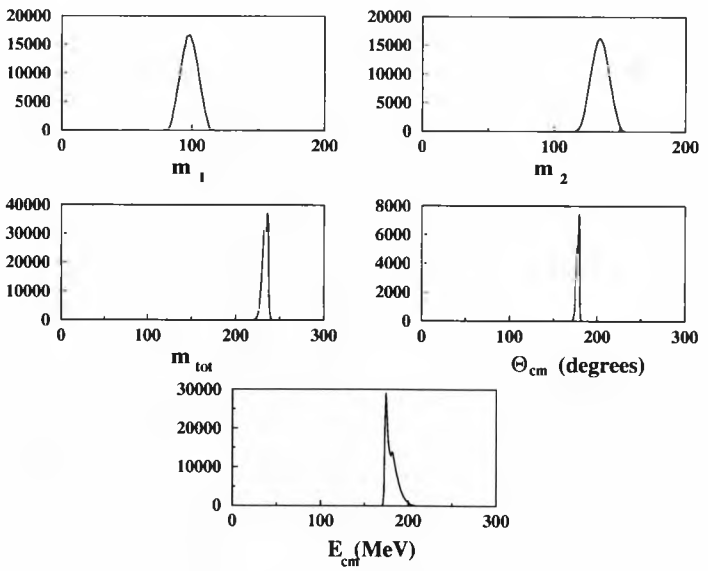

Figure 4.8: Output of the analysis procedure for delayed fission of Pu using values of θ, ϕ and time given by the Monte Carlo simulation, with the recoil distance given by the known fission time input into the calculation.

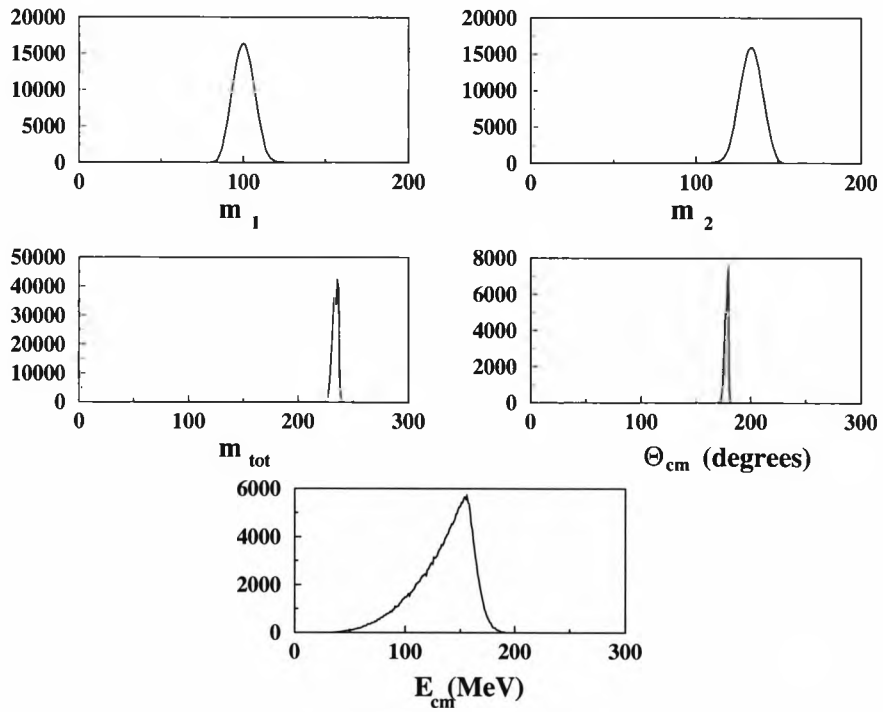

Figure 4.9: Output of the analysis procedure for delayed fission of Pu using values of θ, ϕ and time given by the Monte Carlo Simulation, assuming no recoil distance.

the Monte Carlo simulation. Figure 4.9 shows the results given by this assumption, it can be seen that the sharp peaks for θ_{cm} and total mass are retained, but that this calculation considerably broadens the E_{cm} peak.

4.4 Results.

4.4.1 Summary of the γ-ray Spectroscopy.

The γ-ray data were analysed separately from the particle data, and is presented in reference[32]. The results of this work are summarised here.

Two dimensional plots of the summed energy (H) deposited in the NaI and shield detectors versus the observed multiplicity or fold (K) gated on γ-rays corresponding to ^{238}Pu or ^{239}Pu detected by the Ge detectors were produced. These plots are shown in figure 4.10. These showed that the population patterns of the inelastic and transfer processes are different, with the transfer reaction populating states at higher energy and spin. The population pattern for the transfer channel is similar to that observed

in similar reactions[9] with two peaks near the yrast line at high and low spins.

Analysis of p-γ-γ correlations yielded the decay schemes of ^{238}Pu and ^{239}Pu. Figure 4.11 shows the total projection of the p-γ-γ matrix, with the ground band transitions labelled by their initial spin. The transitions labelled with half-integer spins are in ^{239}Pu, and those labelled with integer spins are in ^{238}Pu.

In ^{239}Pu the ground band was observed to the $\frac{49}{2}^+$ level, with a tentative identification of the $\frac{51}{2}^+ \rightarrow \frac{49}{2}^+$ transition. A distinct band observed in the ungated spectrum, that had previously been observed[38] but with no definite assignment, was assigned to ^{239}Pu. It was tentatively placed as the continuation of an octupole band previously observed upto spin $\frac{11}{2}^-$[39]. A second, weakly populated band, was placed as the other signature band. These two bands extend the octupole band to $(\frac{35}{2}^-)$ and $(\frac{37}{2}^-)$ for the two signature partners of the band. Lack of statistics led to insufficient γ-γ evidence to establish these assignments. Other known bands in ^{239}Pu[39] were not observed, but since very few states with spins above $\frac{11}{2}^+$ are known the possibility that unidentified lines correspond to higher spin states in side bands is not excluded. The decay scheme for ^{239}Pu is shown in figure 4.12.

In ^{238}Pu the ground band was observed up to spin 26^+. Known transitions from other bands in ^{238}Pu[40] were not observed. The cross section for populating states that feed through the 6^+ state was determined to be (65$\pm$25) mb. From systematics this represents approximately 80–90% of the total transfer cross section.

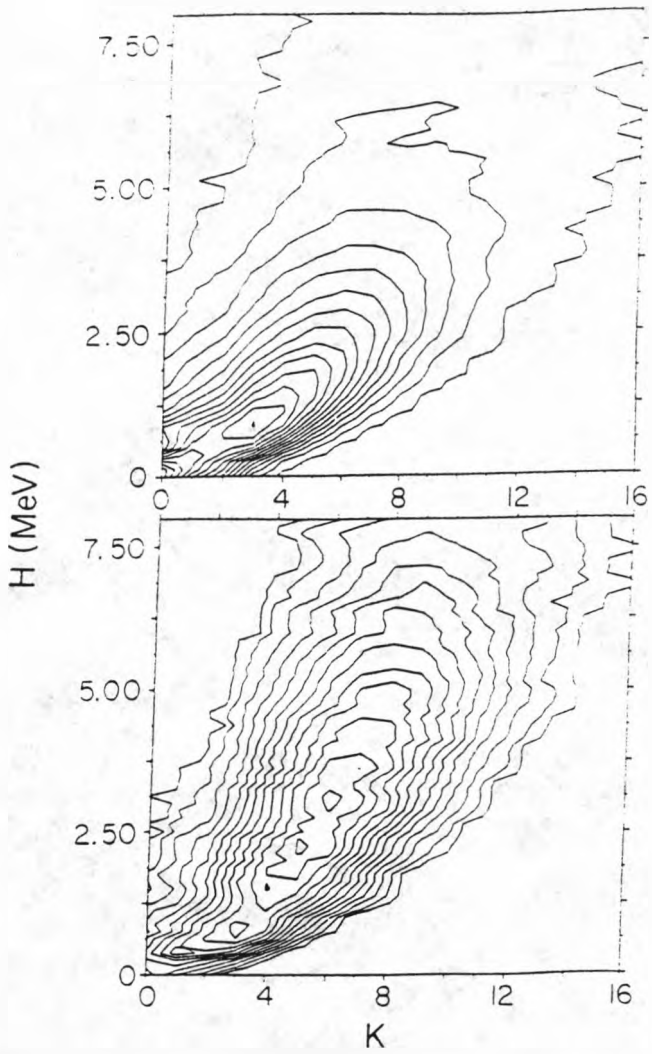

Figure 4.10: Two dimensional plots of summed energy (H) versus fold (K) produced with gates set on ^{239}Pu γ-rays (top) and ^{238}Pu γ-rays (bottom), taken from reference[32].

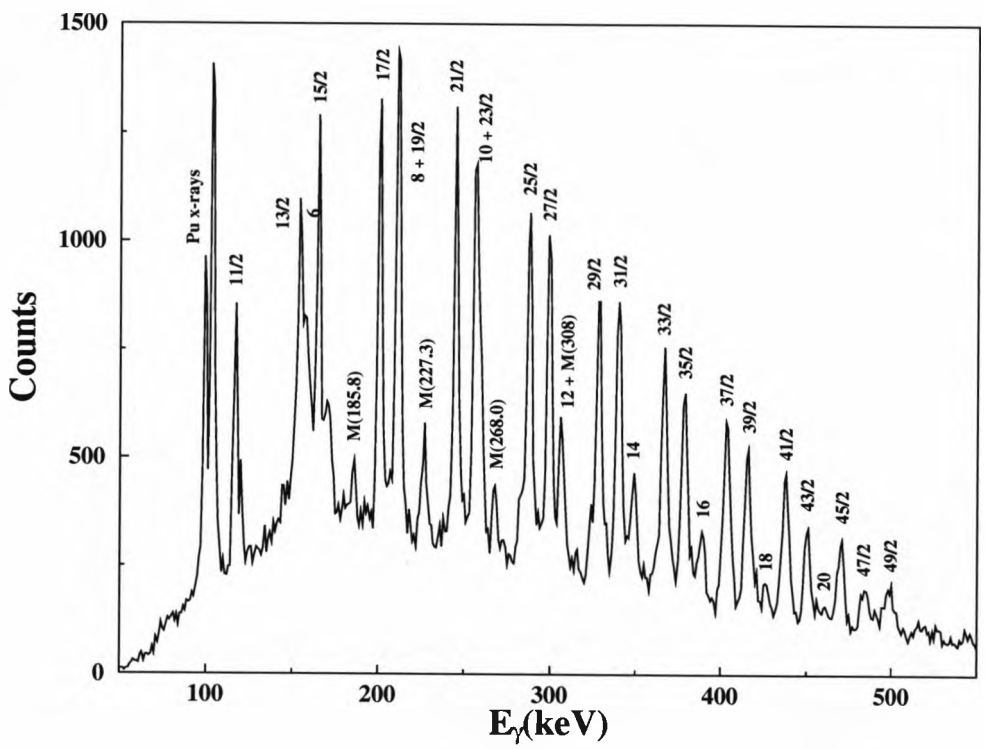

Figure 4.11: The total projection of the p-γ-γ matrix. The ground band transitions are labelled by their initial spin, half-integer for ^{239}Pu transitions and integer for ^{238}Pu transitions. The transitions labeled by M's are "side-band" lines.

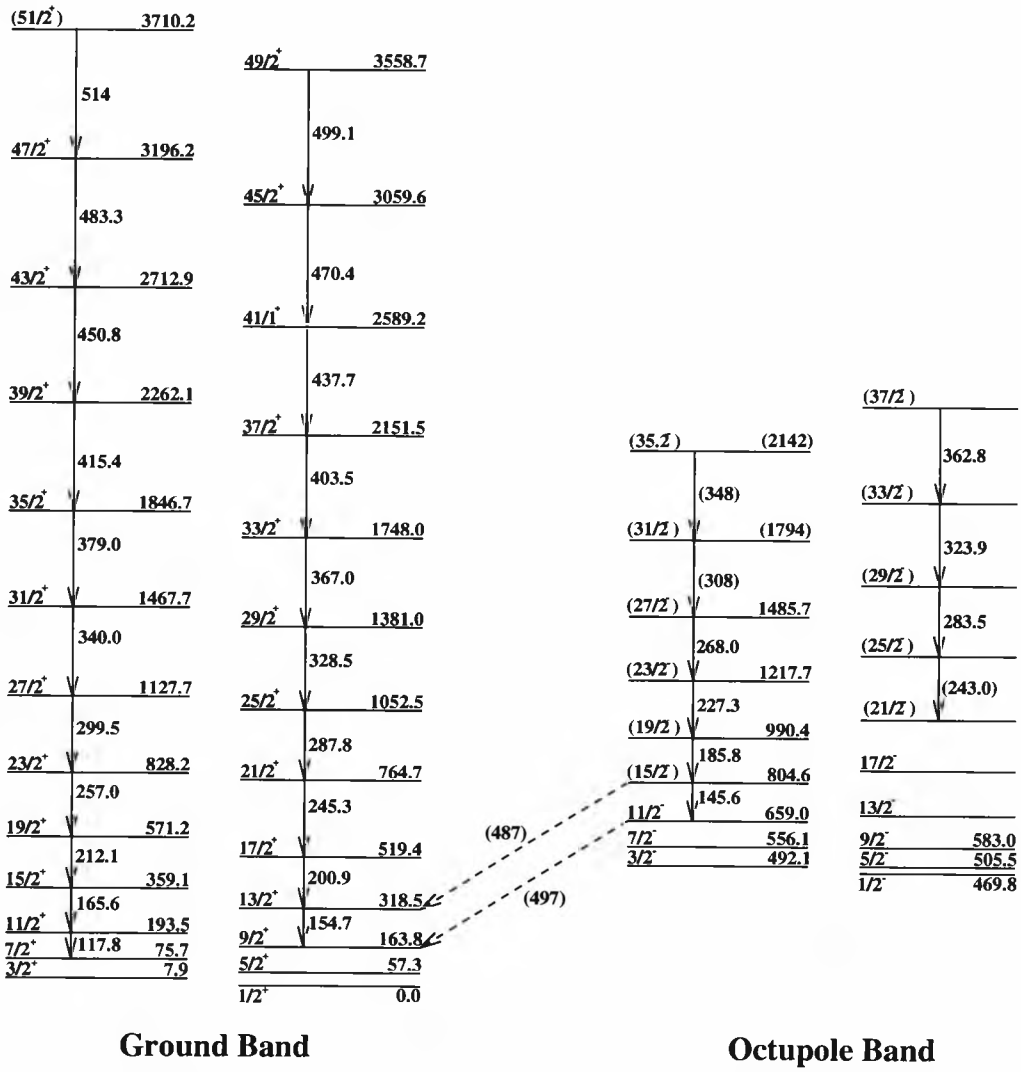

Figure 4.12: The decay scheme of ^{239}Pu. The transition observed in this experiment are labelled by their energies.

4.4.2 Prompt Fission Results.

Two dimensional contour plots of θ_1 vs θ_2 and $time_1$ vs $time_2$ were used to show the values of laboratory angle and flight time for the two particles in the front detectors. These plots and the regions of the θ_1 vs θ_2 and $time_1$ vs $time_2$ space which were assumed to contribute to fission are shown in figure 4.13. These regions were chosen by inspection of the output of the Monte Carlo simulation. They were confirmed by setting gates on the masses and θ_{cm} to give two dimensional plots gated on events correponding to fission. These plots are shown in figure 4.14 where it can be seen that requiring values of θ_{cm}, m_1, m_2 and m_{tot} which correspond to fission enhances the regions which are assumed to contribute to fission.

The values of m_1, m_2, m_{tot}, E_{cm} and θ_{cm} of events in the regions of the θ_1 vs θ_2 and $time_1$ vs $time_2$ plots corresponding to fission are shown in figure 4.15. It can be seen from the spectra for m_1 and m_2 that the mass distribution for prompt fission has a large symmetric component. This justifies the use of a symmetric distribution in the Monte Carlo calculation of the detector efficiency.

Gates were then set on the resulting mass and θ_{cm} spectra to select events with $30 < m_{1,2} < 190$, $210 < m_{tot} < 275$ and $150° < \theta_{cm} < 207°$, the limits of these gates are also indicated on figure 4.15. These were the gates used to produce the two dimensional plots in figure 4.14. The γ-ray spectrum from the Ge detectors in coincidence with these gates was constructed. The γ-rays were Doppler corrected assuming that they were emitted by the scattered Sn nucleus. This spectrum was used to determine the origin of the prompt fission events. A similar spectrum of γ-rays from Sn with no gates set was also produced. These spectra, as well as spectra gated on Pu γ-rays for comparison, are shown in figure 4.16. The ungated and the fission gated spectra are for all p-γ events in the mask out data with no background subtracted. The spectra gated on the Pu γ-rays were generated by gates on a matrix of Pu γ-ray energy against Sn γ-ray energy produced using all p-γ-γ events from the mask in and mask out data sets, the background was subtracted using background regions in the Pu γ-ray spectrum. The two dominant γ-rays in these spectra are the 158.6 keV $\frac{3}{2}^+ \rightarrow \frac{1}{2}^+$ transition in ^{117}Sn corresponding to inelastic scattering and the 1229.5 keV $2^+ \rightarrow 0^+$ transition in ^{118}Sn corresponding to one neutron pick-up.

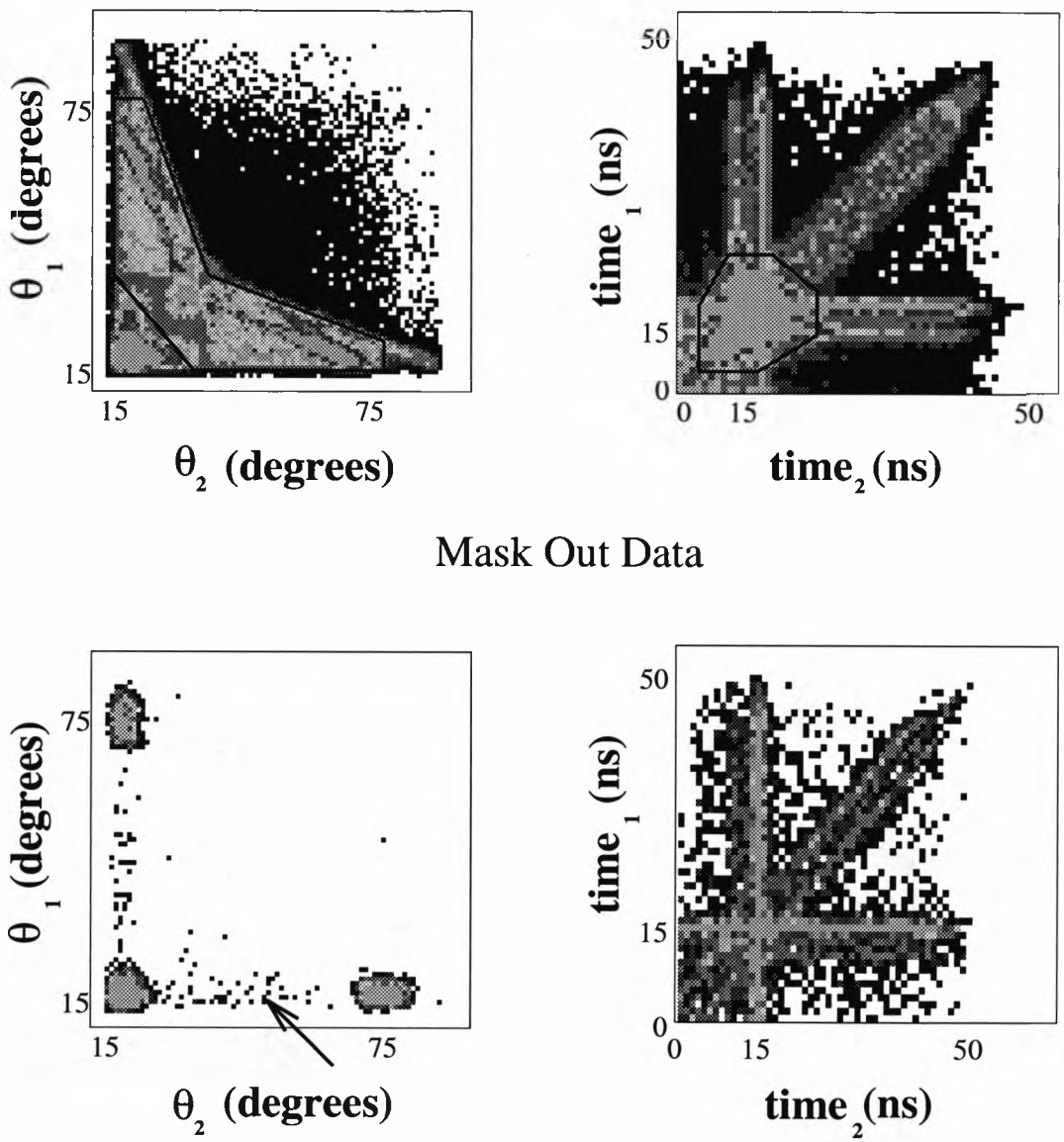

Figure 4.13: Two dimensional contour plots of θ_1 vs θ_2 and $time_1$ vs $time_2$ of events in the front counters. The top two plots are for the mask out data, the approximate positions of the gates set on these plots are the regions enclosed by the solid black lines. The bottom two plots are for the mask in data, the single candidate delayed fission event is the event on the θ_1 vs θ_2 plot which is indicated by the arrow and is one of several events with $time_1 \approx time_2 \approx 15$ ns and is not indicated for clarity. The regions with $\theta_1 \approx \theta_2 \approx 15°$; $\theta_1 \approx 15°$, $\theta_2 \approx 75°$ and $\theta_1 \approx 75°$, $\theta_2 \approx 15°$ correspond to random events as described in the text.

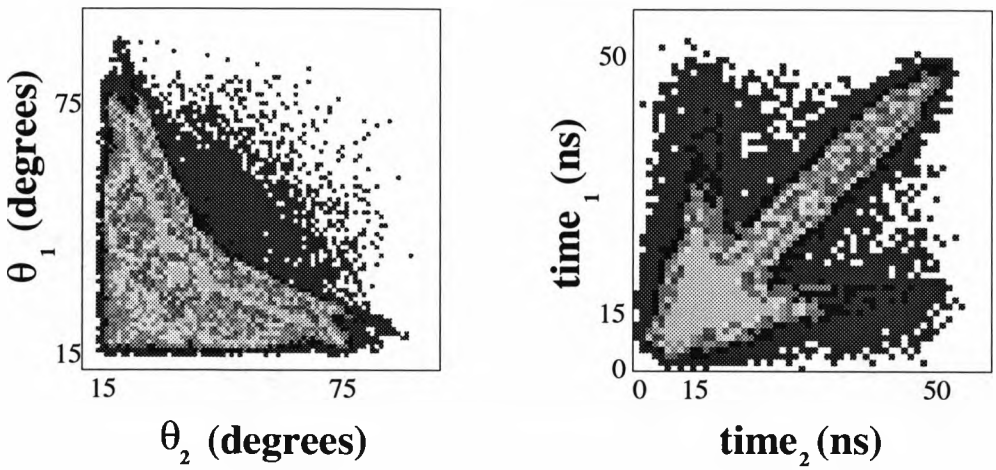

Figure 4.14: Two dimensional contour plots of θ_1 vs θ_2 and $time_1$ vs $time_2$ generated by gates giving events with θ_{cm}, m_1, m_2 and m_{tot} corresponding to fission.

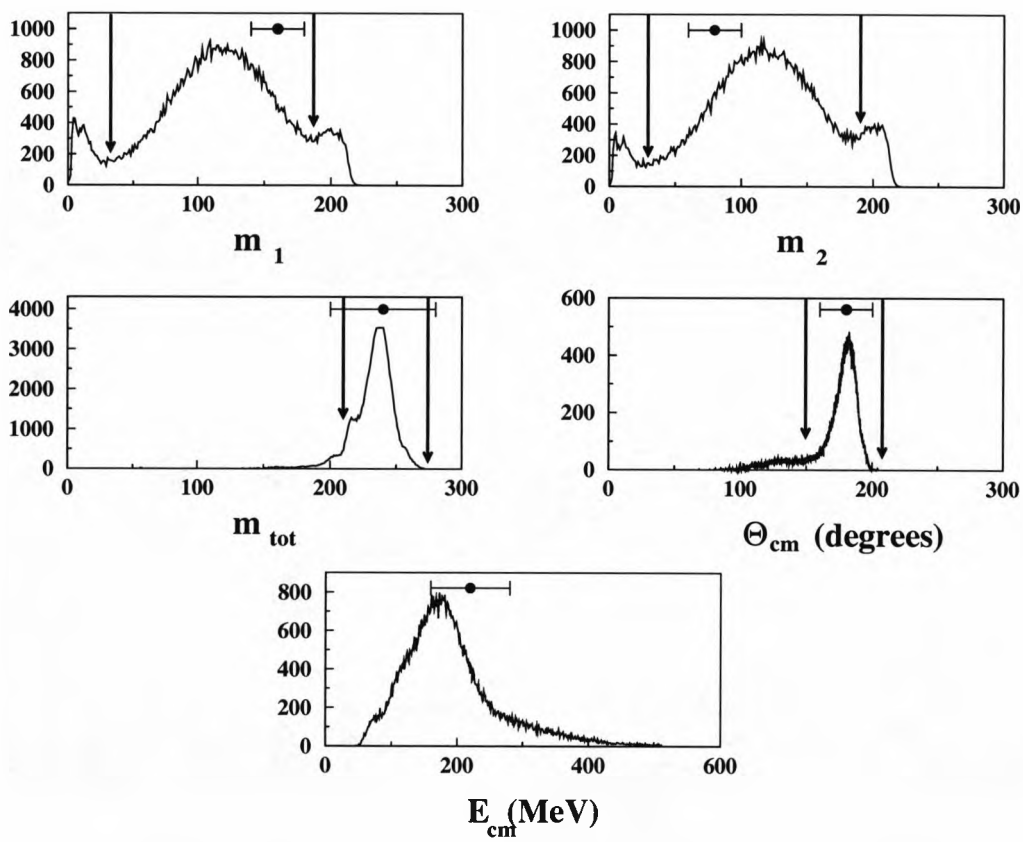

Figure 4.15: The values of $m_{1,2}$, m_{tot}, θ_{cm} and E_{cm} for coplanar events with gates set on the regions of the θ_1 vs θ_2 and $time_1$ vs $time_2$ which contribute to fission, as indicated on figure 4.13. The arrows indicate the limits of the gates set on these spectra to give the fission gate used to generate the Sn γ-ray spectrum. The points marked above the graphs show the values for these quantities of the candidate delayed fission event for comparison.

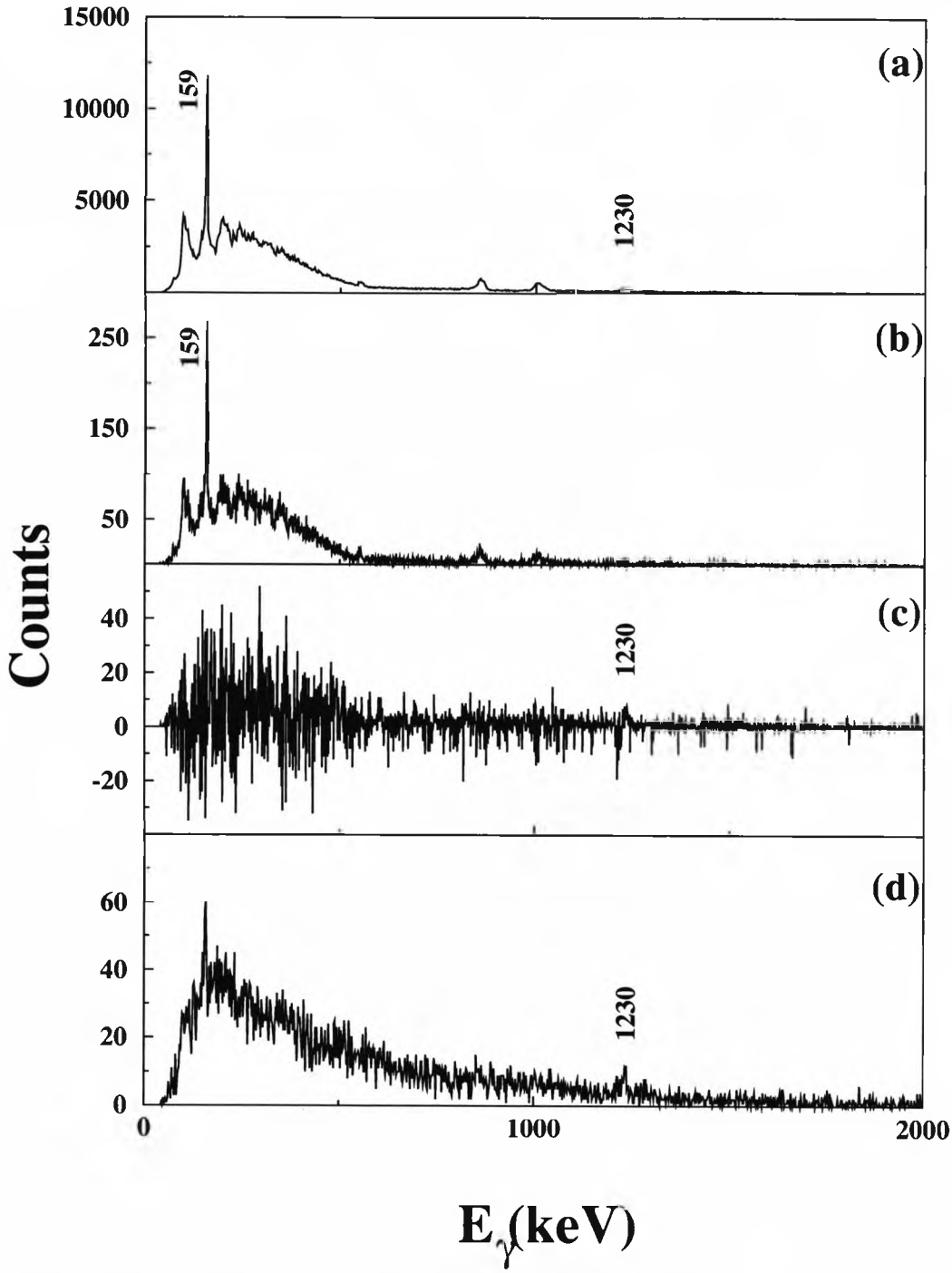

Figure 4.16: The γ-ray spectra, Doppler corrected assuming emission from the scattered Sn. (a) Total ungated spectrum, (b) gated on ^{239}Pu, (c) gated on ^{238}Pu, and (d) gated on fission. The γ-rays indicated are the 158.6 keV transition in ^{117}Sn (labelled 159), and the 1229.5 keV transition in ^{118}Sn (labelled 1230).

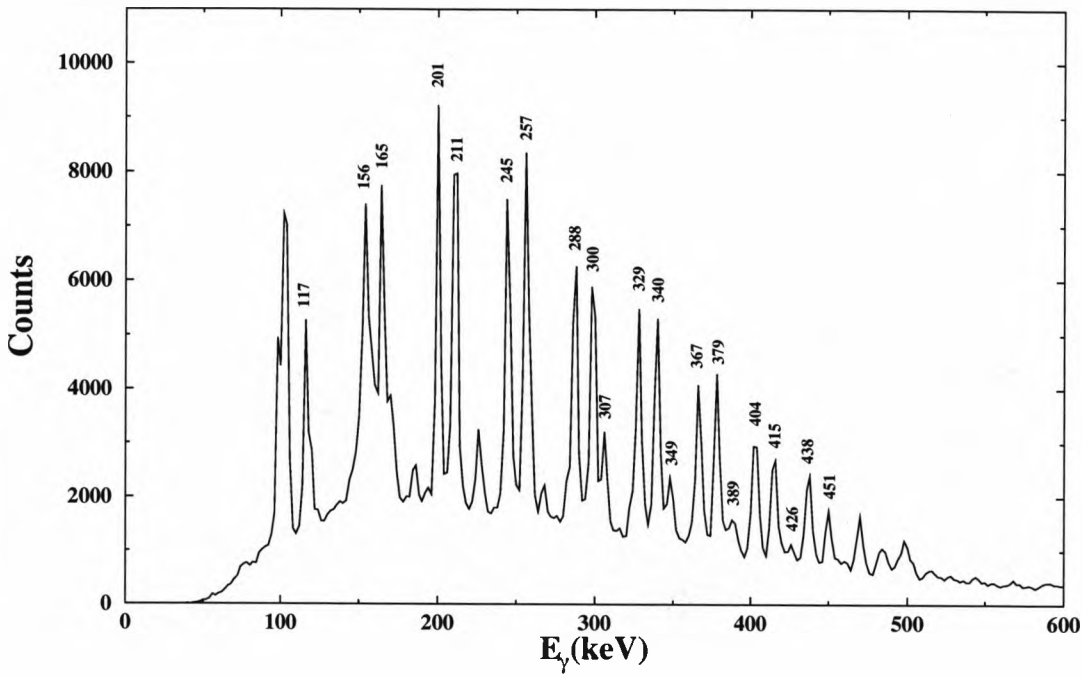

Figure 4.17: The γ-ray spectrum for all p-γ events in the mask out data, Doppler corrected assuming they were emitted by the recoiling Pu nucleus. The transitions which were gated on to produce the Sn γ-ray spectra gated on Pu are shown, they are listed in the text.

The γ-rays were also Doppler corrected assuming that they were emitted by the recoiling Pu nucleus. The spectrum produced by this calculation for all the p-γ events in the mask out data is shown in figure 4.17, where the peaks used to define the Pu gated Sn γ-ray spectra in figure 4.16 are marked with their energies. In ^{238}Pu these are the 158.1 keV $6^+ \rightarrow 4^+$, 210.4 keV $8^+ \rightarrow 6^+$, 260.1 keV $10^+ \rightarrow 8^+$, 306.8 keV $12^+ \rightarrow 10^+$, 349.0 keV $14^+ \rightarrow 12^+$, 389.4 keV $16^+ \rightarrow 14^+$ and 426.4 keV $18^+ \rightarrow 16^+$ transitions. In ^{239}Pu these are the 117.8 keV, 154.7 keV, 165.6 keV, 200.9 keV, 212.1 keV, 245.3 keV, 257.0 keV, 287.8 keV, 299.5 keV, 328.5 keV, 340.0 keV, 367.0 keV, 379.0 keV, 403.5 keV, 415.4 keV, 437.7 keV and 450.8 keV ground band transitions shown in figure 4.12.

The intensities of the two Sn γ-rays in the spectra shown in figure 4.16 were measured. In the total Sn γ-ray spectrum there were 20800 ± 300 159 keV γ-rays and 1800 ± 100 1230 keV γ-rays observed. For the Sn γ-ray spectrum gated on the fission events there were 90 ± 30 159 keV γ-rays and 100 ± 15 1230 keV γ-rays observed.

The number of Sn γ-rays detected is the product of the number of Pu nuclei included in the gate, the efficiency of the Ge counter and the probability that the

event excites the low lying states in the Sn ion.

$$N_{Sn_\gamma} = \varepsilon_\gamma P_x N_{Pu} \tag{4.19}$$

The number of Pu nuclei in the gate is either the total number of ^{238}Pu or ^{239}Pu (for the ungated Sn γ-ray spectrum) or the number of ^{238}Pu or ^{239}Pu fissions detected (for the fission gated Sn γ-ray spectrum). The number of Pu nuclei in the ungated spectrum can be found from the number of γ-rays from transitions near the bottom of the ground state bands in the two nuclei. In figure 4.17 there are 7300 ± 170 117.8 keV $\frac{11}{2}^+ \rightarrow \frac{7}{2}^+$ γ-rays from ^{239}Pu and 5600 ± 600 158.1 keV $6^+ \rightarrow 4^+$ γ-rays from ^{238}Pu. The relative efficiencies and internal conversion coefficients for these transitions are $\varepsilon_{117} = 1210$, $\alpha_{117} = 4.9$, $\varepsilon_{158} = 1310$ and $\alpha_{158} = 1.1$. These give $N_{^{238}Pu} = (9.0 \pm 0.7)\varepsilon_N$ and $N_{^{239}Pu} = (35.4 \pm 1.0)\varepsilon_N$, where ε_N is a normalization term resulting from the conversion from relative to absolute Ge efficiencies.

The probability of exciting the low lying states in Sn,

$$P_x = \frac{N_{Sn}}{N_{Pu}} \tag{4.20}$$

The number of Sn nuclei excited above the low lying states can also be found from the number of Sn γ-rays observed in the ungated spectrum in figure 4.16. The relative efficiencies and internal conversion coefficients for the transitions in Sn are $\varepsilon_{158} = 1310$, $\alpha_{158} = 0.16$, $\varepsilon_{1230} = 350$ and $\alpha_{1230} = 2.7 \times 10^{-4}$. These give $N_{^{117}Sn} = (15.9 \pm 0.2)\varepsilon_N$ and $N_{^{118}Sn} = (6.7 \pm 0.3)\varepsilon_N$. For the transfer channel $P_x = 0.74 \pm 0.07$, and for the inelastic channel $P_x = 0.45 \pm 0.01$.

It was assumed that a large component of the excitation of the Sn resulted from Coulomb excitation in the entrance channel or excitation during the transfer reaction. Thus P_x was taken to be the same for Pu nuclei which did and did not fission.

The fraction of each channel which fissions, P_f, is the ratio of the number of Pu nuclei which fission to the total number of Pu nuclei. The number of Pu nuclei can be found from the number of Sn γ-rays detected. The total number of Pu nuclei is

$$N_{Pu(tot)} = \frac{N_{Sn_\gamma(tot)}}{(\varepsilon_\gamma P_x)} \tag{4.21}$$

and the number of Pu nuclei which fissioned is

$$N_{Pu(fiss)} = \frac{N_{Sn_\gamma(fiss)}}{(\varepsilon_\gamma \varepsilon_f P_x)} \tag{4.22}$$

Where $N_{Sn_\gamma(tot)}$ and $N_{Sn_\gamma(fiss)}$ are the number of Sn γ-rays seen in the total γ-ray spectrum and the γ-ray spectrum produced by the gate on fission events respectively. $\varepsilon_f = 57.8\%$, and is the efficiency for detecting prompt fission events determined by the Monte Carlo simulation. So, the fraction of the channel which fissions,

$$P_f = \frac{N_{Pu(fiss)}}{N_{Pu(tot)}} = \frac{N_{Sn_\gamma(fiss)}}{N_{Sn_\gamma(tot)}\varepsilon_f} \tag{4.23}$$

For the transfer channel, this gives $P_f = (9.5 \pm 1.2)\%$. From the concurrently measured cross section of (65 ± 25) mb[32] for the transfer channel, the cross section for the prompt fission of ^{238}Pu following transfer is (6 ± 2) mb.

For the inelastic channel, $P_f = (0.7 \pm 0.3)\%$. The systematics of fission following inelastic excitation follow a Z_p^7 dependence for actinide nuclei[41], where Z_p is the charge on the projectile nucleus. Extrapolation of previous measurements[41] gives $P_f = (0.4 \pm 0.2)\%$ for the fission of ^{239}Pu induced by inelastic scattering of Sn. This is consistent with the value measured in this work. From the observed values of $N_{^{239}Pu}$ and $N_{^{238}Pu}$ the cross section for the inelastic channel is (250 ± 100) mb. These values for P_f and total cross section correspond to a cross section for the prompt fission of ^{239}Pu following inelastic excitation of (1.7 ± 1.0) mb.

4.4.3 Delayed Fission Results.

The second data set, taken with the mask in place, was analysed in the same way as the prompt fission events. Again, two dimensional plots of θ_1 vs θ_2 and $time_1$ vs $time_2$ were produced and are shown in figure 4.13. The region at $\theta_1 \approx \theta_2 \approx 15°$ corresponds to events with a genuine backscattered Sn and recoiling Pu with a random forward-going particle. The regions at $\theta_1 \approx 15°$, $\theta_2 \approx 75°$ and $\theta_1 \approx 75°$, $\theta_2 \approx 15°$ correspond to events involving scattering from the edge of the mask.

No gates were set on the $time_1$ vs $time_2$ plot, and the random regions described above were excluded. This left 150 events, for each of which values for θ_{cm}, $m_{1,2}$, m_{tot} and E_{cm} were calculated. It was found that, as predicted by the Monte Carlo simulation, these values were largely independent of the recoil time, and hence no

information on the fission lifetime is available. Only events for which $150° < \theta_{cm} < 210°$, $210 < m_{tot} < 275$ and $0.2 < m_1/m_2 < 5$ were accepted.

There is only one event which satisfied all three of these gates, it is indicated by the arrow on the θ_1 vs θ_2 plot of figure 4.13. On the $time_1$ vs $time_2$ plot it is one of the several events with $time_1 \approx time_2 \approx 15$ ns. For this event $\theta_{cm} = 180 \pm 20°$, $m_1 = 160 \pm 20$, $m_2 = 80 \pm 20$, $m_{tot} = 240 \pm 40$ and $E_{cm} = 220 \pm 60$ MeV. The errors were determined by varying the range of Pu in Ni by 30% and the positions and times within the resolution of the detector and noting the variation in the values given. These values are shown on figure 4.15, where it can be seen that this event lies within the experimentally observed range of values for prompt fission. The fragment masses are more asymmetric than the average for the prompt fission, as would be expected[37].

An estimate for the number of random events that would be expected to satisfy these conditions can be made. There are 150 events after excluding the random regions described above, of these 3 have the correct m_{tot} and 8 have the correct θ_{cm}. The value for m_{tot} and θ_{cm} are largely independent, so assuming all these events are randoms it would be expected that approximately 1 in 1000 would have both the m_{tot} and θ_{cm} within the limits given.

Since no information on the fission lifetime is available, the possibility that the one event is due to the direct fission of the 3 ns isomeric state in ^{239}Pu populated by inelastic excitation cannot be ruled out. This possibility is, however, unlikely because this state has only been observed to decay to the lower-lying 8 μs isomer in previous studies[42]. So, if the 3 ns isomer has been observed then this would imply that the 8 μs isomer has also been strongly populated by inelastic excitation.

The ratio of isomeric to prompt fission cross sections was obtained by normalizing to the number of events in the backward detector. If the observed event is due to the direct fission of the 3 ns isomer in ^{239}Pu, then the ratio of delayed fission to prompt fission of ^{239}Pu is $(1.7 \pm 1.7) \times 10^{-4}$. This corresponds to a cross section of (0.3 ± 0.3) μb for the direct fission of this state.

If, as is more likely, the observed event corresponds to the 0.5 ns isomer in ^{238}Pu then the ratio of delayed fission to prompt fission of ^{238}Pu is $(12 \pm 12) \times 10^{-6}$ following

HITR. This corresponds to a cross section of (80 ± 80) nb for the fission of the 0.5 ns isomer in ^{238}Pu. Fission isomer events also have been observed previously following the ^{236}U(α,2n)^{238}Pu reaction[12], in which the maximum ratio of delayed to prompt fission was $(20 \pm 2) \times 10^{-6}$.

4.5 Discussion.

Taking the most likely assumption, that the observed delayed fission event is due to the decay of the 0.5 ns isomer in ^{238}Pu, then the ratio of delayed to prompt fission of ^{238}Pu is $(12 \pm 12) \times 10^{-6}$. This ratio is comparable to the maximum ratio observed following a light ion induced reaction, implying that the reaction used here has not enhanced the population of the fission isomer. The cross section for populating the fission isomer in this experiment is also considerably smaller.

One explanation of why this experiment has failed to populate the fission isomer appreciably is that the entry states to the second minimum, which are presumably several MeV above the minimum itself, are unstable with respect to decay through the outer fission barrier. This would result in prompt fission if the transfer populated the second minimum at higher spin, or if the Coulomb excitation of the second minimum created high spin.

Another explanation would be that the two quasiparticle states that are selectively populated by the transfer reaction do not readily couple to the superdeformed state in the second minimum. This would result in very little mixing between the normal and superdeformed wavefunctions, and so little population of the second minimum. This is similar to the situation with the Pt experiment.

A further experiment is proposed to try to populate the 0.5 ns fission isomer in ^{238}Pu more strongly using the ^{237}Np(^{58}Ni,^{57}Co)^{238}Pu one proton stripping reaction at a beam energy of 345 MeV. A Distorted Wave Born Approximation (DWBA) simulation carried out by the Rochester group gave that the summed Q-window for the ^{238}Pu peaks to be about 4.5 MeV with a width of about 7 MeV. This should be, in principle, an ideal energy window to explore the second minimum in ^{238}Pu. A cross section of about 5% of the Rutherford cross section is expected, compared to

about 20% for the one neutron pick-up reaction. If it is assumed that the ratio of the population of the second minimum to the first minimum is about the same as that of the (d,p) reaction (3.0×10^{-4}) then the detection rate for the delayed fission events could be about 600/day for a 1 pnA beam on a 300 μg/cm^2 target using the same apparatus as the experiment described here.

Chapter 5

Population of Two Quasiparticle States in Dy Nuclei.

5.1 Introduction.

The properties of Heavy Ion-induced Transfer Reactions (HITR) should be well suited to populating collective bands built upon quasiparticle excitations in deformed nuclei. The quasiparticle states can be formed easily by the addition or removal of a nucleon from the ground state of a nucleus, the large electromagnetic field associated with the heavy ions should then allow large simultaneous Coulomb excitation of bands built on these intrinsic excitations.

In previous experiments using the ^{161}Dy(^{58}Ni,^{59}Ni)^{160}Dy reaction at a beam energy of 270 MeV[8, 14] it was shown that two quasiparticle states in ^{160}Dy are populated by a HITR. In the first of these experiments[8] a plot of total energy vs multiplicity showed two peaks, as can be seen in figure 5.1. This is consistent with direct population of the ground state, the peak with the lower multiplicity, and excited two quasiparticle states in ^{160}Dy.

In the second experiment[14] the γ-rays observed in NaI detectors in coincidence with the strongest ^{161}Dy and ^{160}Dy transitions observed in Ge detectors were studied. The spectra for the transfer and inelastic channels for the NaI detectors in three angular ranges are shown in figure 5.2. In the transfer channel there were two peaks with a Doppler shift corresponding to γ-emission from the Dy; a poorly resolved peak at about 400-500 keV and a broad pronounced peak at about 1 MeV. These were interpreted as resulting from transitions between excited two quasiparticle bands (at

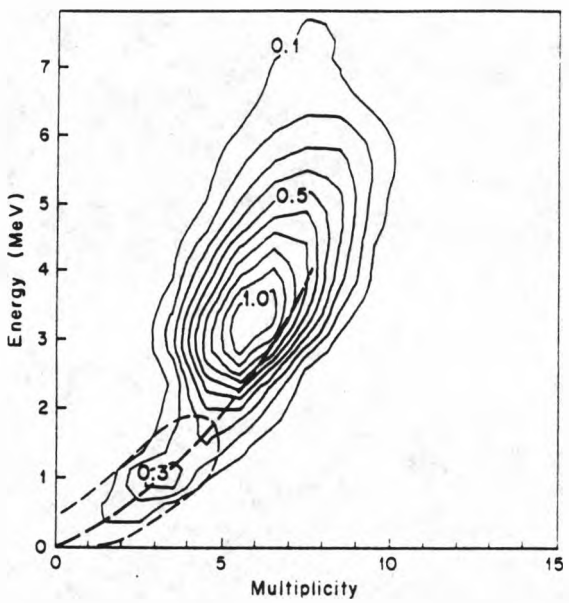

Figure 5.1: Plot of total energy vs multiplicity taken from reference[8] for the transfer reaction ^{161}Dy(^{58}Ni,^{59}Ni)^{160}Dy (solid lines) and the inelastic reaction ^{161}Dy(^{58}Ni,^{58}Ni$'$)^{161}Dy (dashed line, 0.1 contour only). The distributions are gated on the strong ground state band transitions in ^{160}Dy and ^{161}Dy observed by Ge detectors respectively. The heavy dashed line represents the ^{160}Dy yrast line.

400–500 keV) and between two quasiparticle bands and the ground state band (at 1 MeV). In neither of these experiments were discrete γ-rays corresponding to decays from two quasiparticle bands resolved.

Light ion induced reactions to ^{160}Dy have populated bands built on two quasiparticle states either directly by (^{3}He,α)[43] or by compound nucleus reactions[44]. These have included 4^- and 1^--bands built on a $\nu i_{\frac{13}{2}} h_{\frac{9}{2}}$ configuration and an S-band built on a $(\nu i_{\frac{13}{2}})^2$ configuration. Similar states have been populated in ^{162}Dy, also using light ion induced reactions[45, 46]. These bands were studied by analysing the reaction products[43, 45] and the de-excitation γ-rays[44, 46].

In the experiment reported here such states in ^{160}Dy and ^{162}Dy were populated using the ^{161}Dy(^{61}Ni,^{62}Ni)^{160}Dy (Q_{gg} = 4.15 MeV) and ^{161}Dy(^{61}Ni,^{60}Ni)^{162}Dy (Q_{gg} = 0.38 MeV) reactions. These reactions are expected to populate bands built upon two quasineutron excitations involving the $i_{\frac{13}{2}}$, $\Omega = \frac{5}{2}$ neutron orbital which is the ground state of ^{161}Dy. The de-excitation γ-rays were studied to investigate the population of the bands built on such two quasiparticle states. The results of this study are presented here and in reference[47]. The excitation energy sharing between the projectile and target in the pick-up reaction were analysed separately, and are presented in reference[48].

5.2 Experimental Details.

The experiment was conducted at the Daresbury Nuclear Structure Facility using a position-sensitive parallel-plate avalanche counter (PPAC) inside the EUROGAM phase I array. The PPAC was an annular backscatter detector, covering angles $117° < \theta < 149°$ in strips of 2°, with 6 ϕ sections covering 50° each. The 16 θ divisions were etched onto a PCB board (the cathode) and connected by a delay line provided by two chips.

The EUROGAM phase I array[49] consists of 45 Compton suppressed Ge detectors. The finite size of the detectors results in the broadening of the γ-rays detected, the additional width of the γ-ray energy being $\Delta E_\gamma \propto \sin\theta \Delta\theta$, which is largest for $\theta = 90°$. The opening angle, $\Delta\theta$, of the 30 detectors in the rings at $\theta = 86°$, 94°,

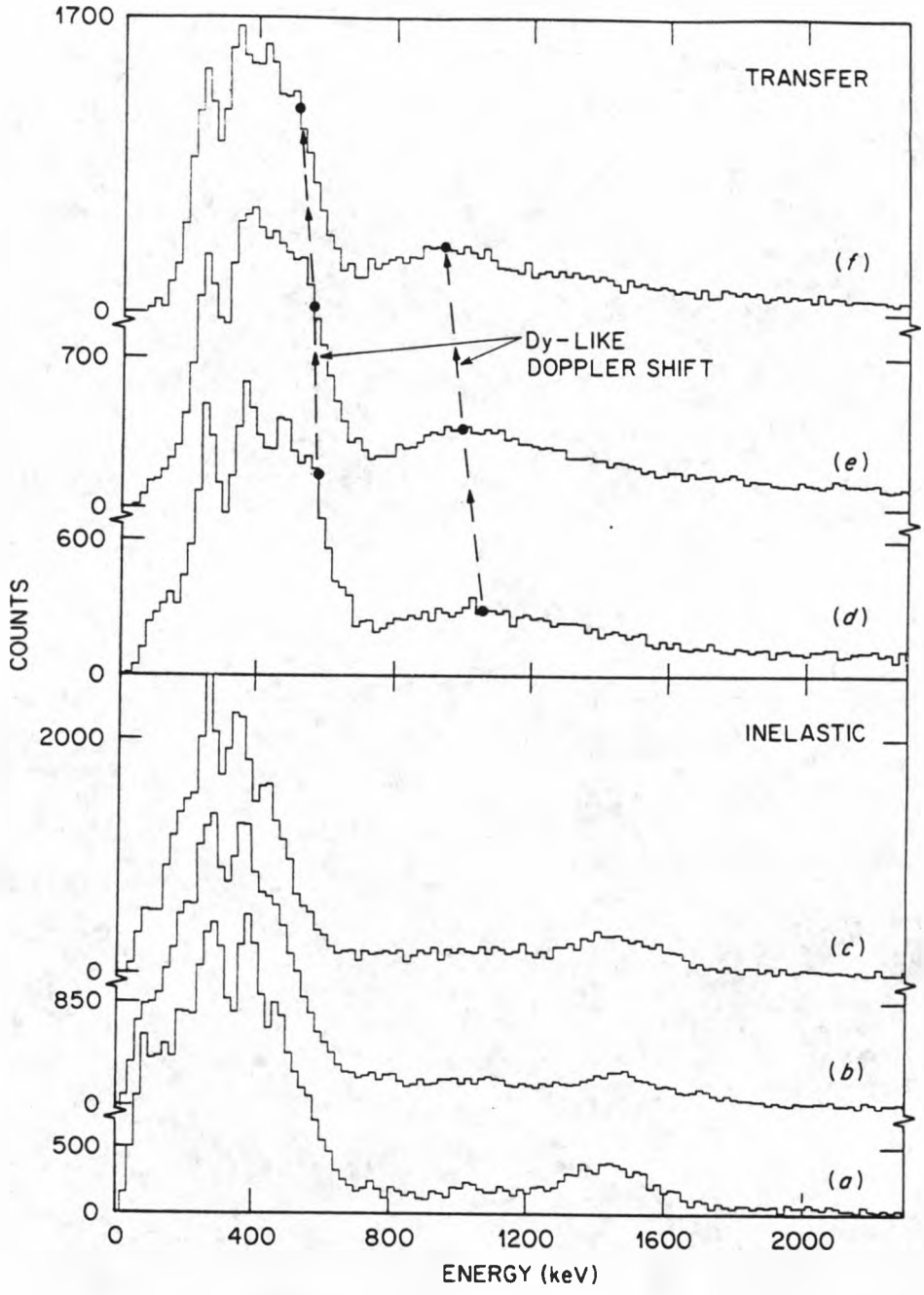

Figure 5.2: Spectra from the NaI detectors in coincidence with strong γ-rays for the inelastic and transfer channels detected in Ge detectors, taken from reference[14]. The spectra are from NaI detectors in three angular ranges; 0°–60° (spectra (a) and (d)), 60°–120° ((b) and (e)), and 120°–180° ((c) and (f)).

108° and 134° was reduced by fitting them with heavy metal slits. This reduced the additional broadening of the γ-ray energies recorded in these detectors due to the Doppler effect from $\approx$ 10 keV to $\approx$ 5 keV for a 1 MeV γ-ray. Heavy metal collimators fitted to the other Ge detectors shield the BGO suppression shield from direct γ-rays emitted from the target, which could generate false vetoes. An attenuator, consisting of a thin sheet of copper, was placed in front of each detector to reduce the efficiency for detecting x-rays. The arrangement of these detectors is shown schematically in figure 5.3.

The setup for the electronics for the PPAC is shown in figure 5.4. The six lines from the anode are amplified and fed into a bit register which gives a signal indicating which anode section fired, and hence the ϕ of the scattered Ni. The output of the bit register was fed into a NIM ADC where it was read by the event builder. The anodes were also fed into an OR to give the FTL1 trigger that was fed into the EUROGAM trigger system. The signals from the two ends of the cathode delay line were amplified and used to start two TACs which were stopped by the trigger from the anodes. The output of these two TACs went into NIM ADCs giving the relative timing of each end of the delay line, the difference between these timings gave the θ of the scattered Ni.

The setup for the electronics for the EUROGAM trigger system is shown in figure 5.5. The electronics for the EUROGAM array are on VXI (VME eXtension for Instrumentation) cards, and generate raw Ge signals (no Compton suppression) and clean Ge signals (Compton suppressed). If the system is not busy then the fast trigger is generated if there is a Ge signal in coincidence with the particle signal or just a particle. The scalars FTR1 and FTR2 are the particle rate, FTR3 the γ rate and FTR4 the p-γ rate. The input FTL2 allows the particle counter to be disabled from the trigger system so that the Ge counters can be set up and calibrated with a constant level in FTL1.

The beam of typically 75 nA 270 MeV ^{61}Ni was incident on a self-supporting 400 μg/cm^2 foil of 95.9% ^{161}Dy, whose major isotopic impurity was ^{162}Dy (2.5%). The polar and azimuthal angles of the backscattered Ni particle detected in the PPAC were used to Doppler correct the coincident γ-rays detected in the EUROGAM

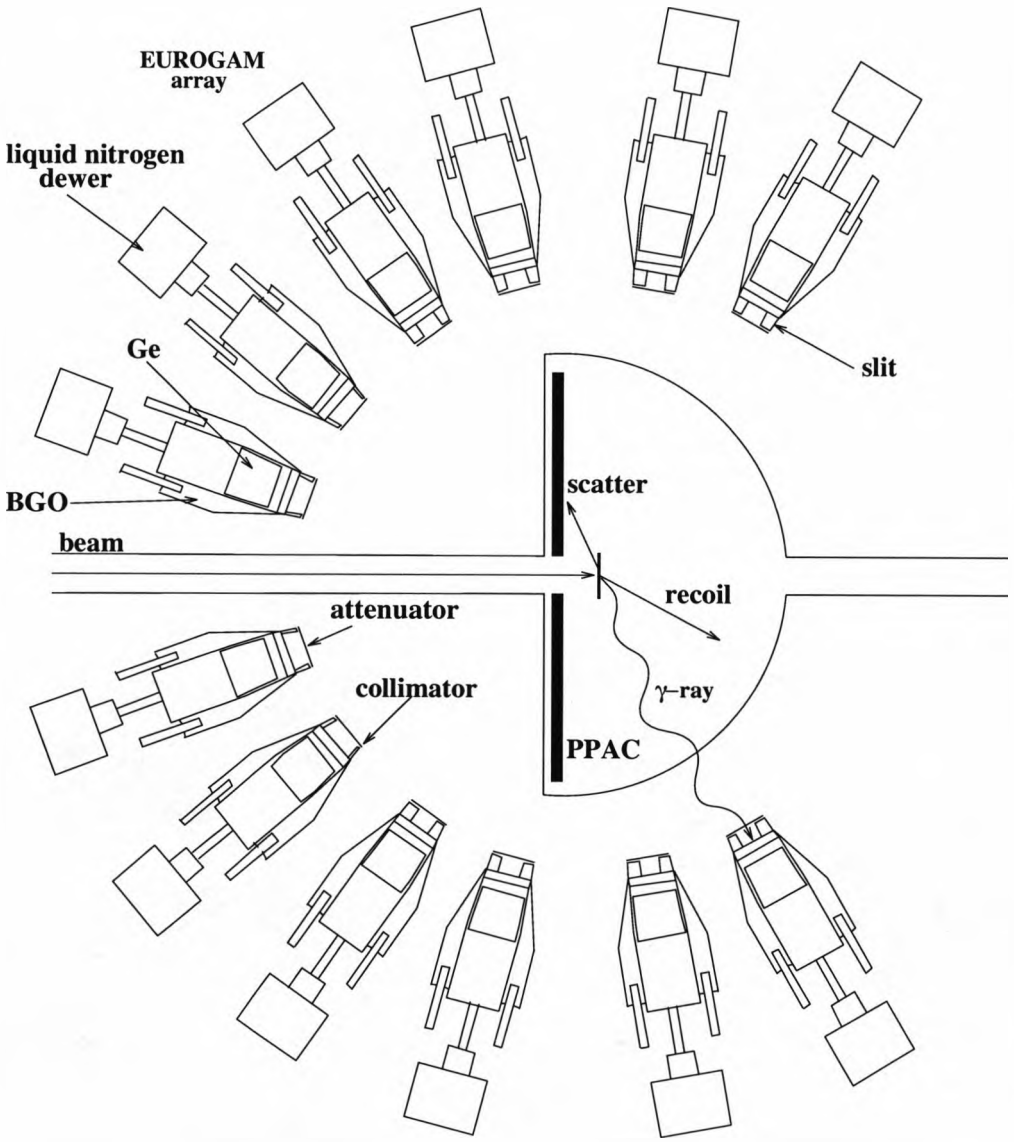

Figure 5.3: Schematic diagram of the detector arrangement. The back scattered Ni was detected in the PPAC, the position of this particle was used to calculate the speed and direction of the recoiling Dy. The de-excitation γ-rays were detected in the EUROGAM phase I array. Slits fitted on the Ge detectors near 90° were used to reduce the Doppler broadening of the γ-rays detected at these angles. The collimators fitted to the other detectors shield the BGO suppression shield from direct γ-rays emitted from the target. The attenuators reduced the efficiency of detecting x-rays.

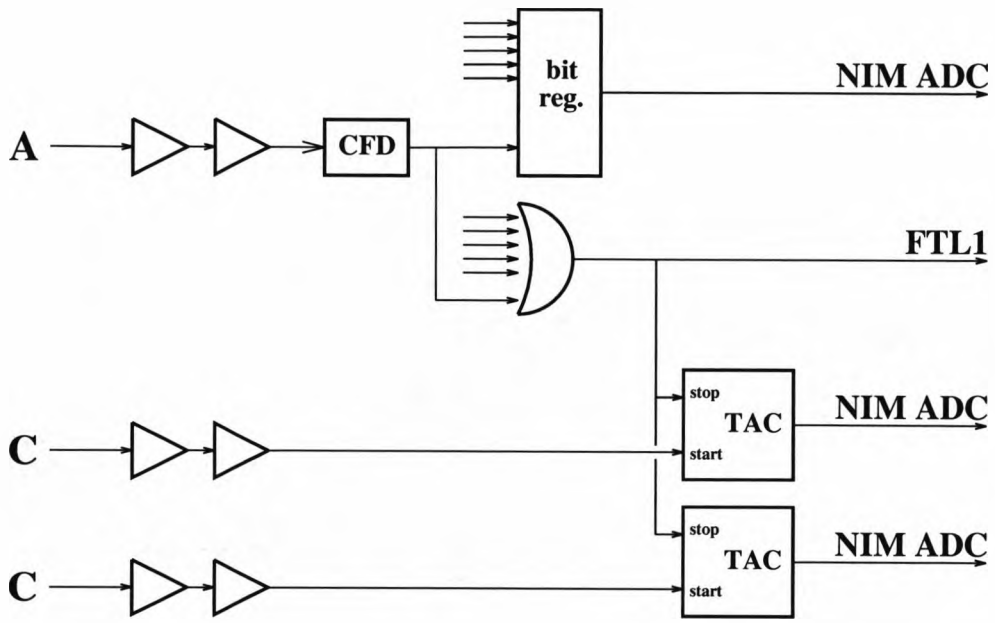

Figure 5.4: Electronic setup for the PPAC. The signal from the anode (A) was used to give the ϕ of the scattered Ni (from the bit register), the trigger (any particle) and the stop pulse for the two TACs for the two ends of the cathode delay line (C). The output from the TACs gave the relative timing of the ends of the cathode delay line, the difference between these times gives θ.

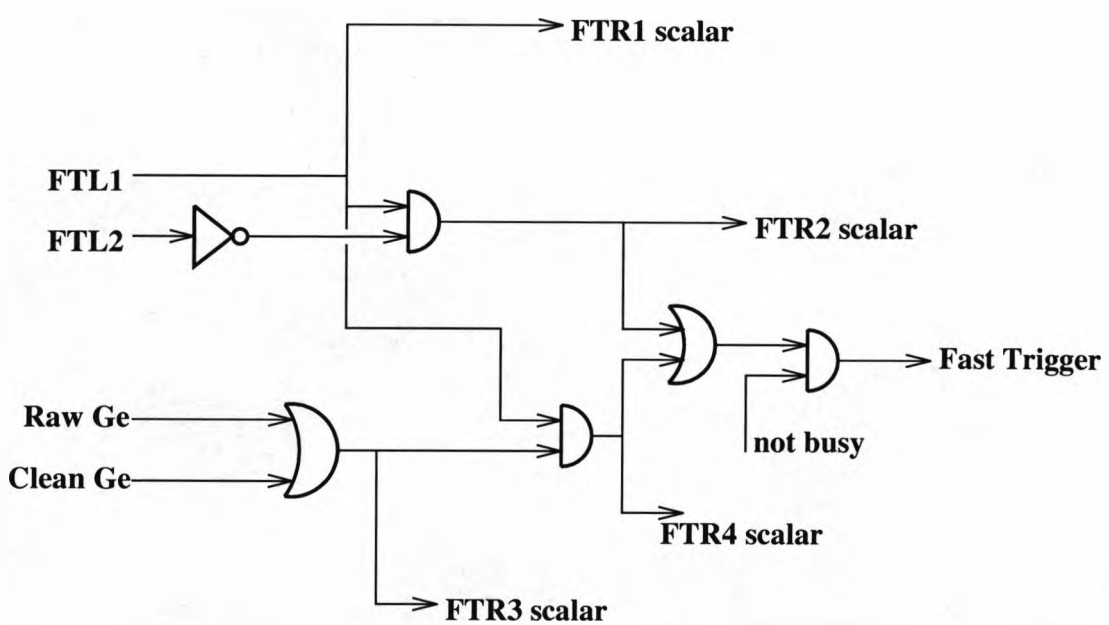

Figure 5.5: Electronic setup for the EUROGAM trigger system. The fast trigger is generated for particle-γ or particle singles events. FTL1 is output from the PPAC electronics, the Ge signals come from VXI cards. The scalars give the particle rate (FTR1 and FTR2), the γ-rate (FTR3) and the p-γ rate (FTR4). The FTL2 input is used for gain matching and calibrating the Ge detectors.

array. The correction was carried out using the same procedure used for the Pt experiment, equations (3.1)–(3.10) using $m_t = 161$, $m_b = 61$, $m_r = 160$, $m_s = 62$ and $E_b = 270$ MeV, assuming the γ-rays were emitted from the recoiling Dy nuclei. The Doppler corrected γ-ray energies were sorted into a particle-γ-γ matrix.

5.3 Results.

The experiment yielded 10.5 million unfolded particle-γ-γ events of which 83% are from the inelastic excitation of ^{161}Dy, 15% are from the pick-up reaction to ^{160}Dy and 2% are from the transfer channel to ^{162}Dy. Figure 5.6 shows the total projection of the p-γ-γ matrix, with the energies of the ground state band transitions in ^{160}Dy and ^{162}Dy marked. The inset shows the region in which transitions from bands built on two quasiparticle states to the ground state band would be expected. There are clearly a large number of discrete transitions in this region. The ridge at 1290 keV is the high energy side of a broad peak due to the 1173 keV $2^+ \rightarrow 0^+$ transition in ^{62}Ni, which is broadened by the Doppler correction procedure.

Each of the transfer channels can be enhanced by requiring that at least one γ-ray is one of the intense ground state band transitions. The coincidence spectra for ^{160}Dy and ^{162}Dy produced by requiring a coincidence with at least one of the four strongest ground state band transitions are shown in figure 5.7, where the four ground state band transitions in each nucleus that are gated on are marked with dots. The transitions marked in the insets are from the γ-vibrational band, an octupole vibrational-like[44] $K^\pi = 2^-$ band and the S-band to the ground state band. The expected positions of the strongest transitions from the previously observed[45, 46] 2^- and S-bands to the ground state band in ^{162}Dy are marked with arrows.

5.3.1 Excitation Energy Sharing.

The measured γ-ray energies were also corrected for Doppler shift assuming that they were emitted by the scattered Ni to study the excitation of the Ni[48]. Figure 5.8 shows the γ-ray spectrum corrected for Ni emission.

The average excitation energy for the ^{62}Ni was about 2.5 MeV[48]. This excitation

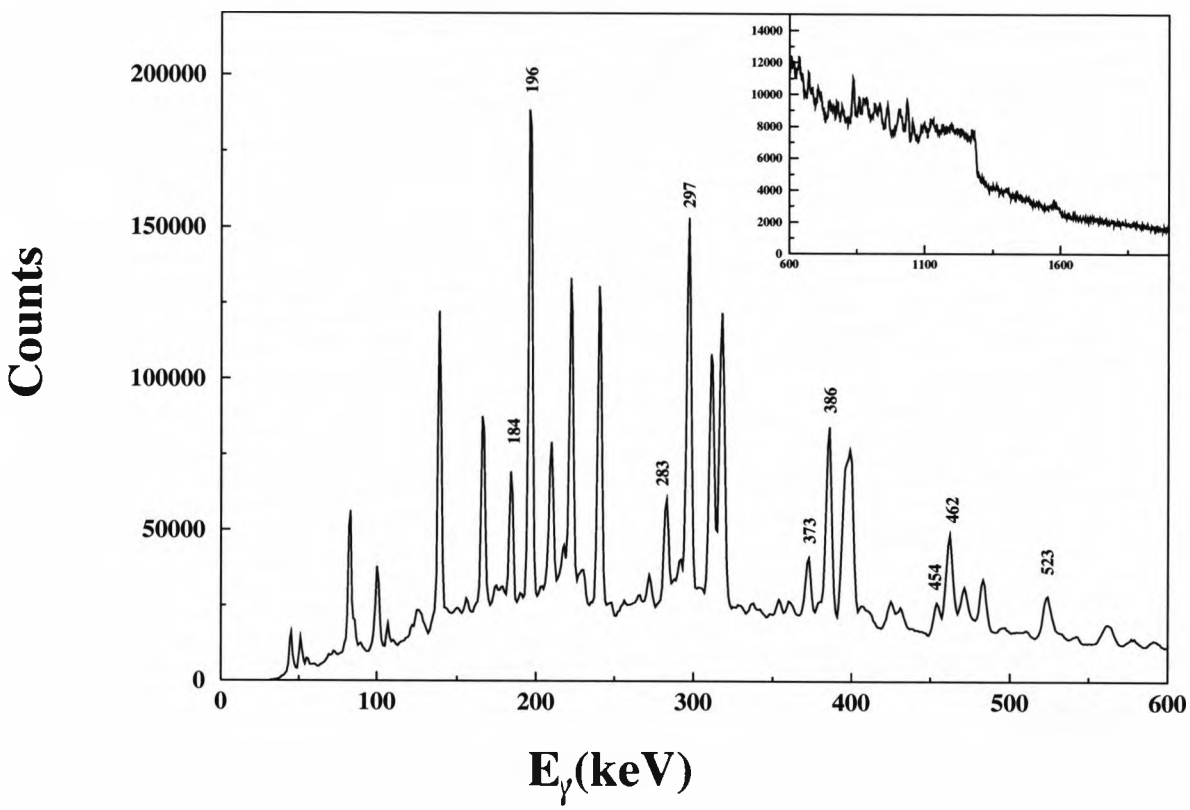

Figure 5.6: The total projection of the p-γ-γ matrix. The transitions labelled are the ground state band transitions in ^{160}Dy (196 keV, 297 keV, 386 keV, 462 keV and 523 keV) and ^{162}Dy (184 keV, 283 keV, 373 keV and 454 keV). The inset is the region where transitions from 2 quasi-particle bands to the ground state band would be expected. The ridge at 1290 keV is due to the 1173 keV transition in ^{62}Ni

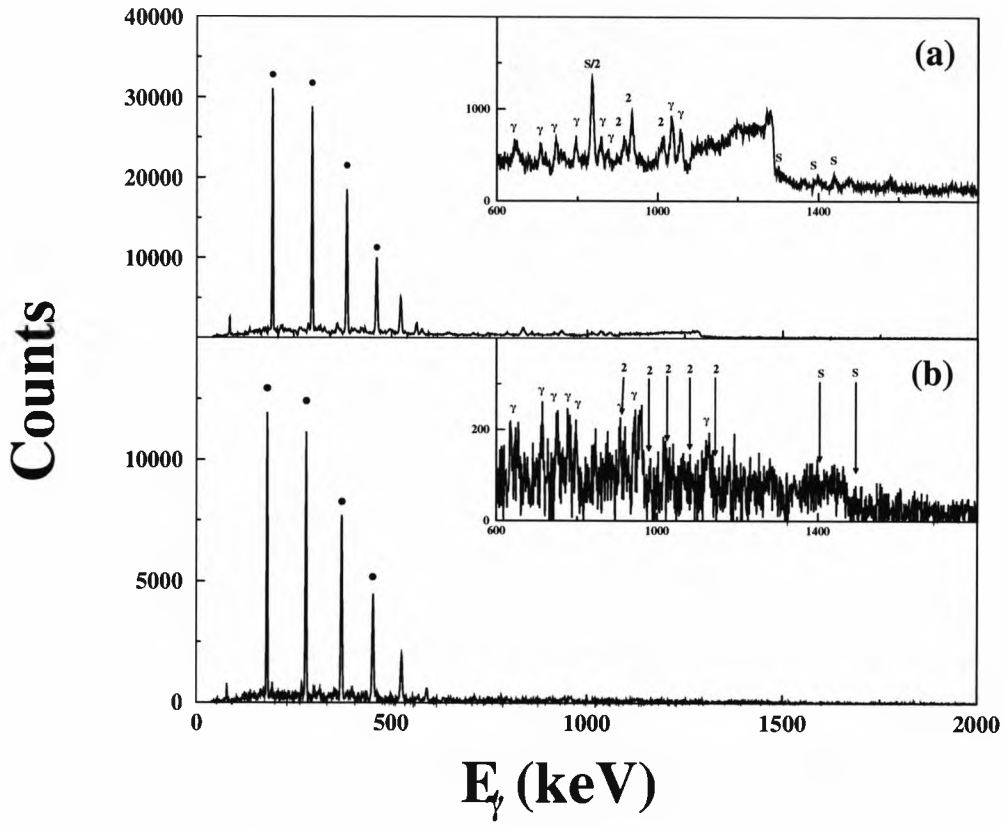

Figure 5.7: Spectra produced by gating on the four strongest ground state band transitions in (a) ^{160}Dy and (b) ^{162}Dy. The dots indicate the ground state band transitions that were gated on. The insets show transitions from the γ-vibrational band and two of the bands built on two quasiparticle states (the 2^- and S-bands) to the ground state band. The arrows in the spectrum for ^{162}Dy show where the most intense of the transitions from the 2^- and S-bands would be expected. Again, the broad peak at 1070–1290 keV is due to the 1173 keV transition in ^{62}Ni

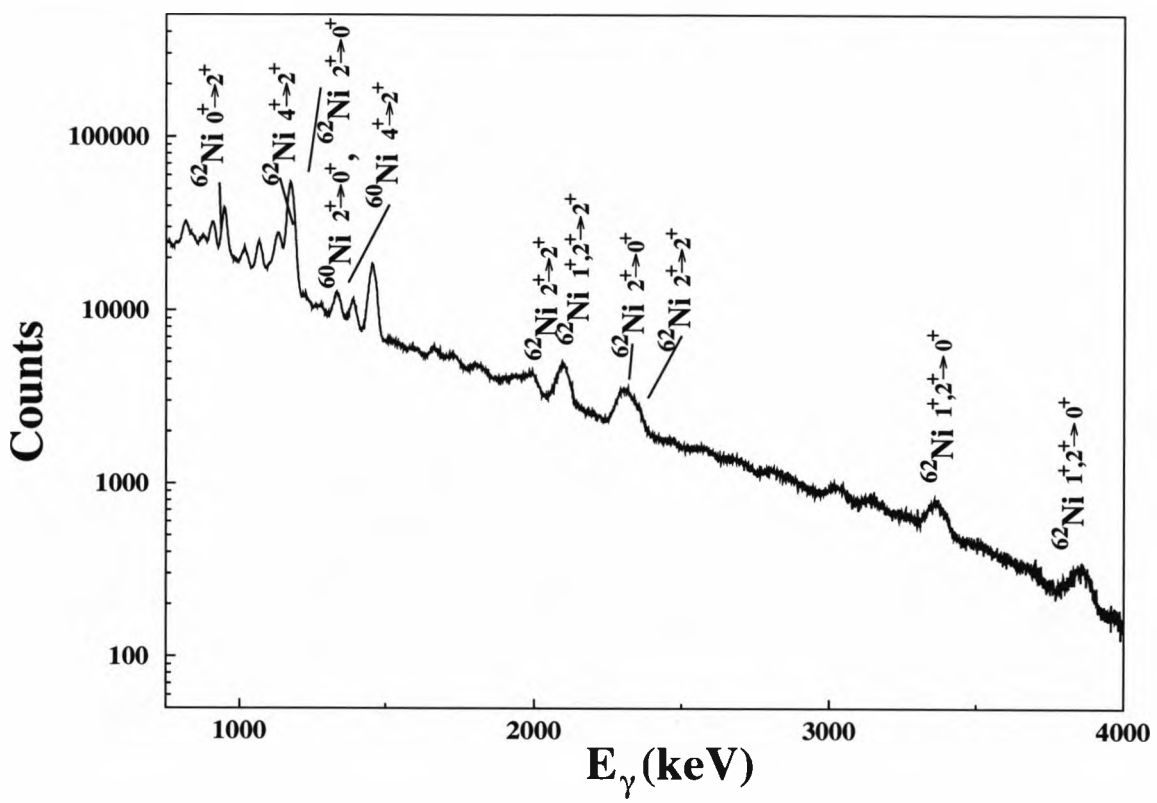

Figure 5.8: The Doppler shift corrected γ-ray spectrum for emission from the Ni particles. The labelled transitions belong to ^{62}Ni (the pick-up channel) and ^{60}Ni (the stripping channel). The unlabelled transitions mostly belong to ^{61}Ni (the inelastic channel).

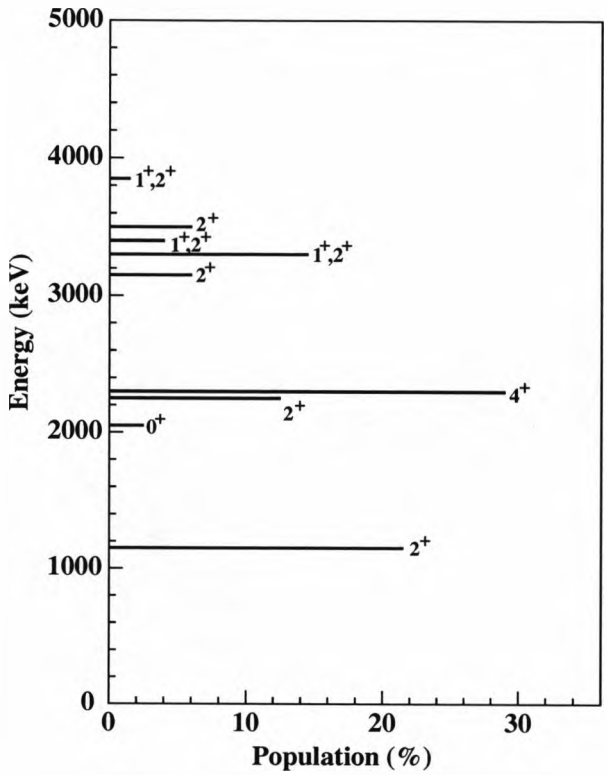

Figure 5.9: The relative population of excited states in ^{62}Ni populated in the pick-up reaction. Typical errors range from 10% to 20% of the values shown. The population of the ground state is less than 10%. Taken from reference[48].

was distributed over several states with excitation energy up to 4 MeV. The relative populations of these states, after accounting for internal conversion, Ge efficiency, branching ratios and feeding, are shown in figure 5.9. The relative population of the ground state is about zero, with a 10% upper limit. The distribution of intensity is highly fragmented.

Similarly, the relative population of states in ^{60}Ni can also be found. Only three levels are significantly excited; the 0^+ ground state with $\approx$ 18% of the intensity, the 2^+ level at 1332 keV with $\approx$ 57% of the intensity and the 4^+ level at 2506 keV with $\approx$ 25% of the intensity.

5.3.2 Inelastic Excitation of ^{161}Dy.

Levels in ^{161}Dy were populated by Coulomb excitation of the target. The γ-ray intensities of the known ground band transitions in ^{161}Dy[50] in the p-γ singles spectrum which could be clearly resolved were measured. The intensities for the transitions

E_γ	Transition	I_γ	E_γ	Transition	I_γ
100.4	$\frac{9}{2}^+ \rightarrow \frac{5}{2}^+$	22.3(8)	311.6	$\frac{19}{2}^+ \rightarrow \frac{15}{2}^+$	1426(1)
101.1	$\frac{17}{2}^+ \rightarrow \frac{15}{2}^+$	288.7(2)	318.1	$\frac{21}{2}^+ \rightarrow \frac{17}{2}^+$	1246(1)
103.6	$\frac{25}{2}^+ \rightarrow \frac{23}{2}^+$	12.6(1)	380.0	$\frac{27}{2}^+ \rightarrow \frac{23}{2}^+$	52.2(5)
107.6	$\frac{21}{2}^+ \rightarrow \frac{19}{2}^+$	48.2(5)	395.9	$\frac{25}{2}^+ \rightarrow \frac{21}{2}^+$	740(4)
139.5	$\frac{15}{2}^+ \rightarrow \frac{13}{2}^+$	692(9)	399.6	$\frac{23}{2}^+ \rightarrow \frac{19}{2}^+$	675(3)
140.4	$\frac{11}{2}^+ \rightarrow \frac{7}{2}^+$	314(9)	468.9	$\frac{31}{2}^+ \rightarrow \frac{29}{2}^+$	21.5(4)
167.0	$\frac{13}{2}^+ \rightarrow \frac{9}{2}^+$	651.0(8)	470.7	$\frac{29}{2}^+ \rightarrow \frac{25}{2}^+$	91.0(10)
210.3	$\frac{19}{2}^+ \rightarrow \frac{17}{2}^+$	459.6(8)	482.9	$\frac{27}{2}^+ \rightarrow \frac{23}{2}^+$	217.5(9)
222.8	$\frac{15}{2}^+ \rightarrow \frac{11}{2}^+$	1229(1)	541.2	$\frac{33}{2}^+ \rightarrow \frac{29}{2}^+$	18.7(7)
240.7	$\frac{17}{2}^+ \rightarrow \frac{13}{2}^+$	1349(1)	559.4	$\frac{31}{2}^+ \rightarrow \frac{27}{2}^+$	51.2(10)
292.1	$\frac{23}{2}^+ \rightarrow \frac{21}{2}^+$	135.0(6)			

Table 5.1: The intensities of the γ-rays in ^{161}Dy.

which could not be clearly resolved were found from spectra produced by gates on the p-γ-γ matrix. The intensities were corrected for the relative efficiency of the Ge array determined from a ^{152}Eu source. These intensities are given in table 5.1.

The level scheme for the ground state band in ^{161}Dy is known[50], and is shown in figure 5.10, which also gives the relative γ-ray branching ratios from each level.

From the known γ-ray branching ratios and internal conversion coefficients[51], and the measured γ-ray intensities the total intensity of the decays from each level can be found. This is the total population of each level, the sum of the decays from higher levels and direct population by Coulomb excitation. The relative population of each level was also found using the Gosia[52] code which simulates Coulomb excitation. The population of each level relative to the $\frac{13}{2}^+$ level measured in this experiment and predicted by the Gosia code are given in table 5.2.

The relative population of states determined from the current experiment and the Gosia code are similar, except for the $\frac{9}{2}^+$ level. The discrepancy between the measured and calculated population for this level is probably due to poor efficiency calibration for γ-rays with energies below 120 keV. This indicates that the calibration and the method for determining the population of levels from the decay scheme are accurate.

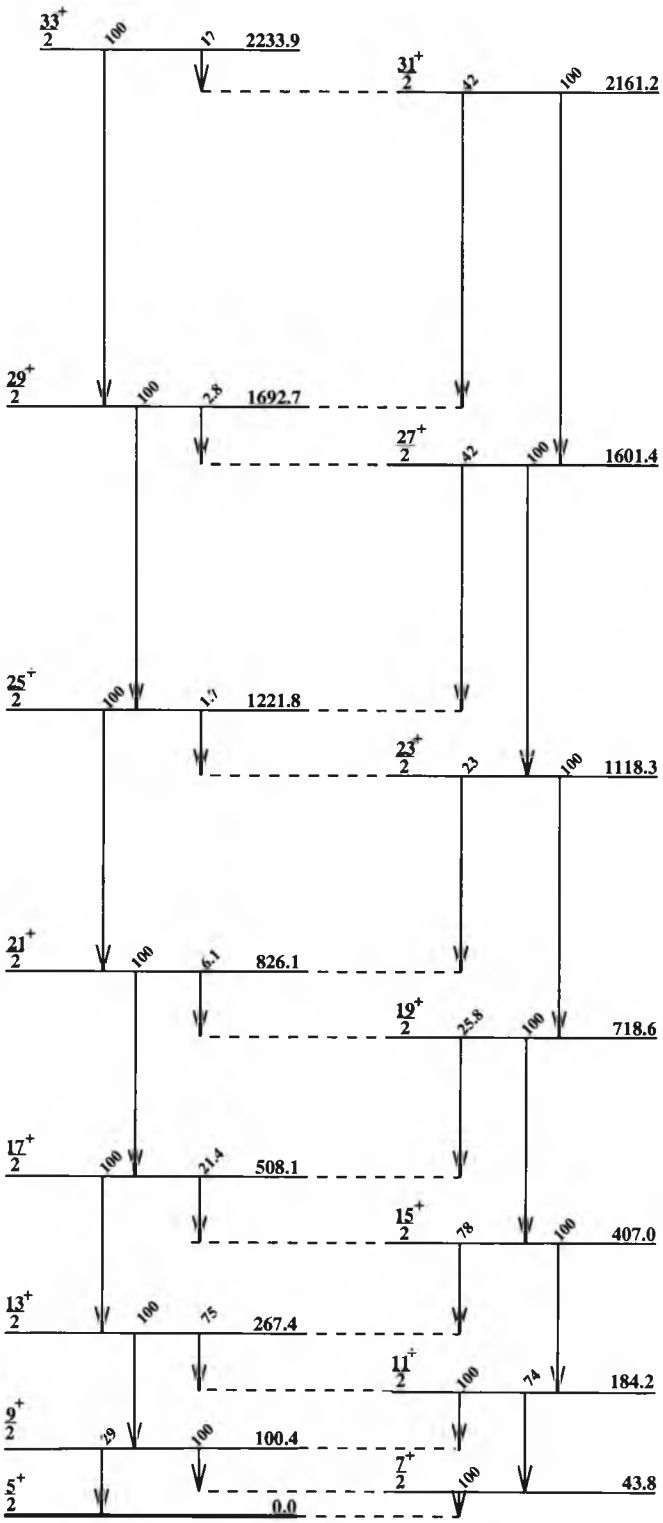

Figure 5.10: The level scheme for the ground state band in ^{161}Dy. The relative γ-ray branching ratios for each level are shown above the arrow marking the transition.

Level	Relative population		Level	Relative population	
	Measured	Gosia		Measured	Gosia
$\frac{9}{2}^+$	42.5(15)	122.2	$\frac{11}{2}^+$	86.4(19)	90.0
$\frac{13}{2}^+$	100.0(1)	100.0	$\frac{15}{2}^+$	61.1(6)	62.4
$\frac{17}{2}^+$	67.1(1)	77.4	$\frac{19}{2}^+$	51.6(1)	48.9
$\frac{21}{2}^+$	41.6(1)	56.4	$\frac{23}{2}^+$	27.0(1)	31.4
$\frac{25}{2}^+$	21.1(1)	29.3	$\frac{27}{2}^+$	8.3(1)	14.3
$\frac{29}{2}^+$	2.7(1)	9.6	$\frac{31}{2}^+$	1.9(1)	4.5
$\frac{33}{2}^+$	1.2(1)	2.1			

Table 5.2: The relative population of the levels in the ground state band of ^{161}Dy as measured in the current experiment and given by the Gosia code.

5.3.3 The Population of ^{160}Dy.

States in ^{160}Dy were populated via the pick-up reaction. Gates were set on the p-γ-γ matrix to determine the decay scheme of ^{160}Dy. From the spectra produced by such gates the energies and intensities of the γ-rays in ^{160}Dy relative to the $4_g^+ \rightarrow 2_g^+$ transition were found, and are given in table 5.3. The subscripts g, γ, S, 1, 2, 8 correspond to levels in the ground state band, γ-vibrtational band, S-band, 1^-, 2^- and 8^- bands respectively. The subscript 4 refers to levels in the 4^+ and 4^- bands for positive and negative parity states respectively. These intensities can be normalized to the transitions in ^{161}Dy, the intensity of the 196.4 keV $4_g^+ \rightarrow 2_g^+$ transition is 825.8 ± 0.9 with the same normalization as the ^{161}Dy transitions.

Figures 5.11 and 5.12 show the level schemes for the observed positive and negative parity bands in ^{160}Dy. The ground state band, γ-vibrational band, S-band, 4^+, 1^-, 2^-, 4^- and 8^-- bands were all observed. No γ-rays for transitions from other known bands[53] were observed. The observed transitions are shown with the relative intensities marked above the arrows. The levels shown by dashed lines are levels in the observed bands known from previous work[44] but which are not observed here.

From the observed intensities of the transitions the total population of each of the bands can be found. By accounting for feeding of the bands, this is the intensity of the direct population of each state in the transfer reaction. From the population of each level the weighted mean excitation energy and spin for the population of each

E_γ	Transition	I_γ	E_γ	Transition	I_γ
125.0	$\{5_2^- \to 3_2^-$, $4_2^- \to 2_2^-\}$	3.5(9), 1.1(2)	(669.7)	$8_8^- \to 7_\gamma^+$	< 0.8
178.4	$12_2^- \to 11_\gamma^+$	0.32(4)	709.3	$5_\gamma^+ \to 6_g^+$	1.3(2)
196.4	$4_g^+ \to 2_g^+$	100.0(1)	727.1	$4_4^+ \to 2_\gamma^+$	2.2(1)
205.2	$7_2^- \to 5_2^-$	1.2(1)	747.5	$12_\gamma^+ \to 12_g^+$	1.5(1)
208.3	$6_2^- \to 4_2^-$	4.6(2)	754.4	$5_4^+ \to 3_\gamma^+$	0.5(3)
222.3	$10_2^- \to 9_\gamma^+$	0.40(6)	762.5	$3_\gamma^+ \to 4_g^+$	3.2(3)
240.4	$1529.4 \to 5_\gamma^+$	2.2(1)	(772.3)	$6_4^+ \to 4_\gamma^+$	< 0.7
241.9	$11_2^- \to 9_\gamma^+$	0.40(6)	795.8	$10_\gamma^+ \to 10_g^+$	1.6(1)
264.6	$8_2^- \to 7_\gamma^+$	0.44(9)	817.1	$10_S^- \to 10_g^+$	0.39(8)
273.1	$1562.1 \to 5_\gamma^+$	0.50(6)	836.6	$\{8_\gamma^+ \to 8_g^+$, $11_2^- \to 10_g^+$, $10_S^+ \to 10_g^+\}$	2.4(2), 0.3(2), 3.3(2)
287.6	$6_\gamma^+ \to 4_\gamma^+$	1.2(5)			
287.4	$9_2^- \to 7_2^-$	1.2(1)	857.3	$6_\gamma^+ \to 6_g^+$	1.9(3)
288.0	$8_2^- \to 6_2^-$	2.1(1)	873.5	$4_\gamma^+ \to 4_g^+$	1.9(8)
294.4	$2_2^- \to 2_\gamma^+$	2.0(1)	915.1	$8_2^- \to 8_g^+$	1.5(3)
297.1	$6_g^+ \to 4_g^+$	85.0(4)	934.5	$9_2^- \to 8_g^+$	3.7(3)
305.1	$6_2^- \to 5_\gamma^+$	0.37(6)	964.4	$\{3_\gamma^+ \to 2_g^+$, $2_\gamma^+ \to 0_g^+\}$	10.1(2)
329.1	$7_\gamma^+ \to 5_\gamma^+$	0.69(10)			
336.8	$4_2^- \to 3_\gamma^+$	1.6(1)	1005.1	$5_\gamma^+ \to 4_g^+$	5.6(2)
359.8	$10_2^- \to 8_2^-$	1.2(1)	1010.6	$8_S^+ \to 8_g^+$	0.5(2)
361.1	$\{(1977.1 \to 7_\gamma^+)$, $(1975.9 \to 7_2^-)\}$	1.4(1)	1013.5	$6_2^- \to 6_g^+$	3.7(2)
			1033.7	$7_2^- \to 6_g^+$	1.5(2)
362.3	$8_\gamma^+ \to 6_\gamma^+$	0.50(10)	1035.4	$7_\gamma^+ \to 6_g^+$	5.4(3)
362.6	$11_2^- \to 9_2^-$	0.23(5)	1057.3	$\{9_\gamma^+ \to 8_g^+$, $11_\gamma^+ \to 10_g^+\}$	3.6(4)
364.5	$\{(4034.6 \to 18_g^+)$, $(3457.4 \to 16_g^+)\}$	0.8(2)			
			(1069.9)	$4_\gamma^+ \to 2_g^+$	< 0.5
385.8	$8_g^+ \to 6_g^+$	54.8(4)	1097.5	$1677.8 \to 6_g^+$	0.9(2)
405.6	$9_\gamma^+ \to 7_\gamma^+$	1.9(2)	1102.2	$4_2^- \to 4_g^+$	1.4(3)
421.7	$10_\gamma^+ \to 8_\gamma^+$	1.2(1)	1117.2	$3_1^- \to 4_g^+$	0.5(3)
424.8	$12_2^- \to 10_2^-$	1.6(1)	1126.8	$5_2^- \to 4_g^+$	2.3(1)
433.3	$(13_2^-) \to 11_2^-$	1.0(1)	(1142.3)	$6_S^+ \to 6_g^+$	< 0.4
461.9	$10_g^+ \to 8_g^+$	27.7(4)	1154.2	$6_\gamma^+ \to 4_g^+$	0.8(3)
465.9	$11_\gamma^+ \to 9_\gamma^+$	0.72(8)	1167.9	$2_2^- \to 2_g^+$	0.8(2)
474.0	$12_\gamma^+ \to 10_\gamma^+$	1.9(3)	1196.4	$\{1_1^- \to 2_g^+$, $3_2^- \to 2_g^+\}$	2.9(1)
482.0	$14_2^- \to 12_2^-$	0.45(3)			
482.5	$8_8^- \to 8_\gamma^+$	1.4(1)	1219.7	$8_\gamma^+ \to 6_g^+$	1.5(3)
(491.1)	$4_1^- \to 3_\gamma^+$	< 1.1	1253.6	$4_1^- \to 4_g^+$	1.4(4)
(491.5)	$6_4^+ \to 6_\gamma^+$	< 0.4	1273.6	$2_1^- \to 2_g^+$	3.6(6)
496.8	$8_1^- \to 7_\gamma^+$	2.6(2)	1281.3	$5_4^- \to 6_g^+$	2.5(6)
497.0	$1925.0 \to 10_g^+$	0.41(6)	1295.8	$10_S^+ \to 8_g^+$	0.46(7)
497.7	$6_1^- \to 5_\gamma^+$	1.9(1)	1311.5	$1891.8 \to 6_g^+$	1.6(3)
(513.5)	$5_4^+ \to 5_\gamma^+$	< 0.7	(1313.6)	$3_1^- \to 2_g^+$	2.0(2)
523.1	$12_g^+ \to 10_g^+$	12.4(3)	1319.3	$8_8^- \to 8_g^+$	1.2(2)
(533.8)	$4_4^+ \to 4_\gamma^+$	< 0.5	1366.8	$5_1^- \to 4_g^+$	1.5(3)
564.0	$14_g^+ \to 12_g^+$	3.7(2)	1396.4	$8_S^+ \to 6_g^+$	2.4(2)
577.5	$\{16_g^+ \to 14_g^+$, $18_g^+ \to 16_g^+\}$	2.0(5)	1439.4	$6_S^+ \to 4_g^+$	2.0(2)
			1479.5	$2059.8 \to 6_g^+$	2.3(2)
(636.7)	$7_4^+ \to 6_\gamma^+$	< 0.6	1523.1	$4_S^+ \to 2_g^+$	0.62(8)
(640.0)	$6_4^+ \to 5_\gamma^+$	< 0.4	1580.5	$5_4^- \to 4_g^+$	3.3(3)
645.8	$4_4^+ \to 3_\gamma^+$	0.75(11)	1654.3	$3082.3 \to 10_g^+$	0.7(2)
648.9	$7_\gamma^+ \to 8_g^+$	1.6(4)	1736.3	$2019.5 \to 4_g^+$	1.5(3)

Table 5.3: Energies and relative intensities of ^{160}Dy transitions derived in the present work. The levels labelled with the subscripts g, γ, S, 1, 2, 8 correspond to levels in the ground state band, γ-vibrational band, S-band, 1^-, 2^- and 8^- bands respectively. The subscript 4 refers to levels in the 4^+ and 4^- bands for positive and negative parity states respectively.

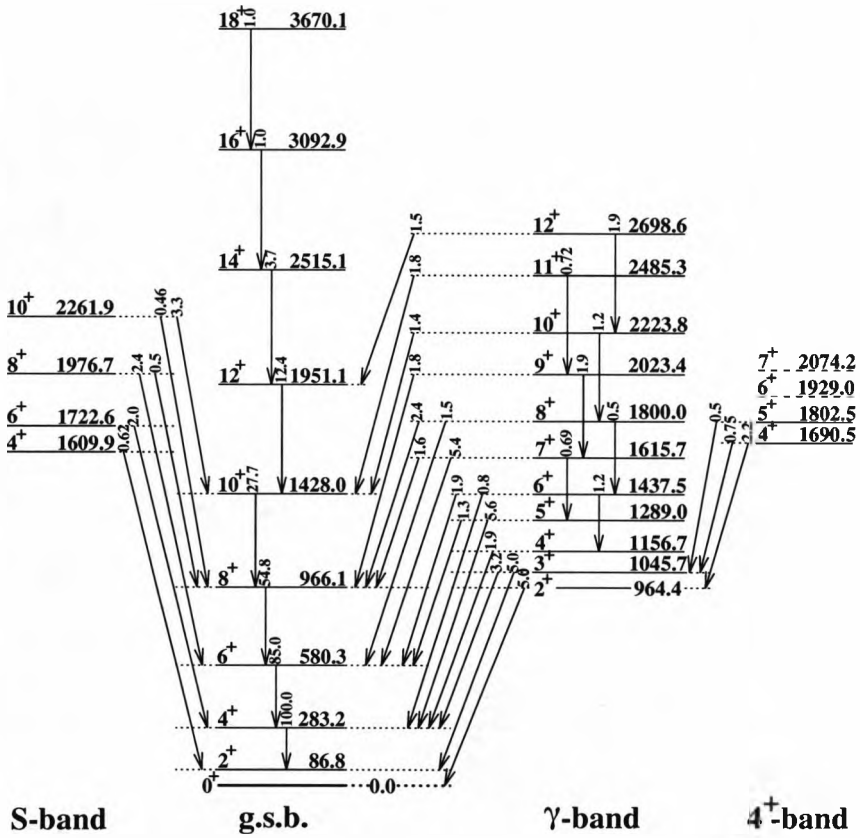

Figure 5.11: Level scheme for the positive parity bands in ^{160}Dy, showing the observed transitions. The relative intensities of the transitions are given above the arrows. The dashed lines indicate levels known from previous work but not observed here.

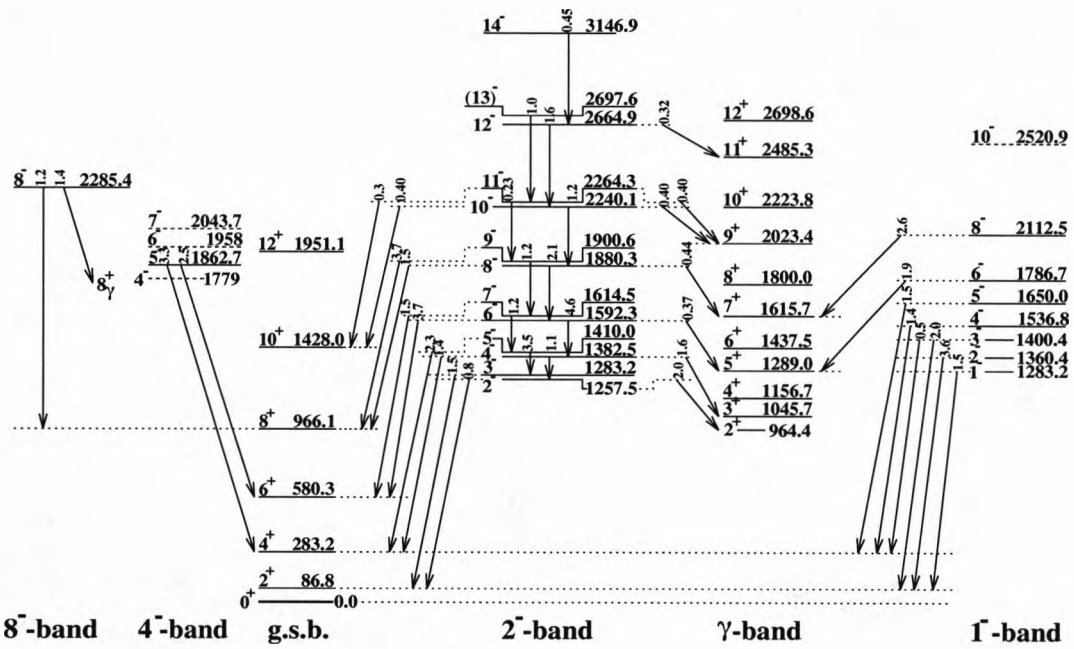

Figure 5.12: Level scheme for the negative parity bands in ^{160}Dy, showing the observed transitions. The relative intensities of the transitions are given above the arrows. The dashed lines indicate levels known from previous work but not observed here.

band	population	I_{ex}	$\overline{E}_{ex}$ (MeV)
gsb	39%	8.5	1.0
γ-band	17%	8.7	1.7
2^--band	17%	7.5	1.7
1^--band	11%	4.5	1.6
S-band	6.9%	8.5	2.0
4^--band	4.3%	$5^\dagger$	$1.9^\dagger$
4^+-band	2.6%	4.2	1.7
8^--band	1.9%	$8^\dagger$	$2.3^\dagger$

Table 5.4: The population and weighted mean spin and excitation energy for each of the bands populated in ^{160}Dy. Only one level is observed in the 4^- and 8^- bands, so the mean values of spin and excitation energy (marked by a †) given are the spin and excitation energy of that level.

band can also be found. Table 5.4 gives the intensity (as a percentage of the total intensity of the transfer channel) and the weighted mean of the excitation energy and spin of each of the bands.

The Ground State Band.

The ground state band (gsb) has been observed in Coulomb excitation work to spin 18[54]. In the ^{158}Gd(α,2n)^{160}Dy experiment[44] it was observed to spin 16. In the present work the gsb is seen to spin 18. There is considerable feeding of the gsb from other bands, as can be seen in figure 5.7.

The γ-vibrational Band.

The $K^\pi = 2^+$ (γ-vibrational) band had previously been observed up to a possible spin 12[44]. In the present data this band is also seen to spin 12. Figure 5.13 shows a selection of gates on transitions between the γ-band and the gsb. Several transitions to the γ-band from higher lying bands can be seen. There are some weak transitions between levels within the γ-band.

The S-band.

A previous ^{161}Dy(^{3}He,α)^{160}Dy experiment[43] had observed levels at 1723 keV and 1974 keV identified as the 6_S^+ and 8_S^+ levels of the $K^\pi = (0^+)$ S-band. A weak level at 1607 keV was also weakly populated and proposed as possibly the 4_S^+ level. A

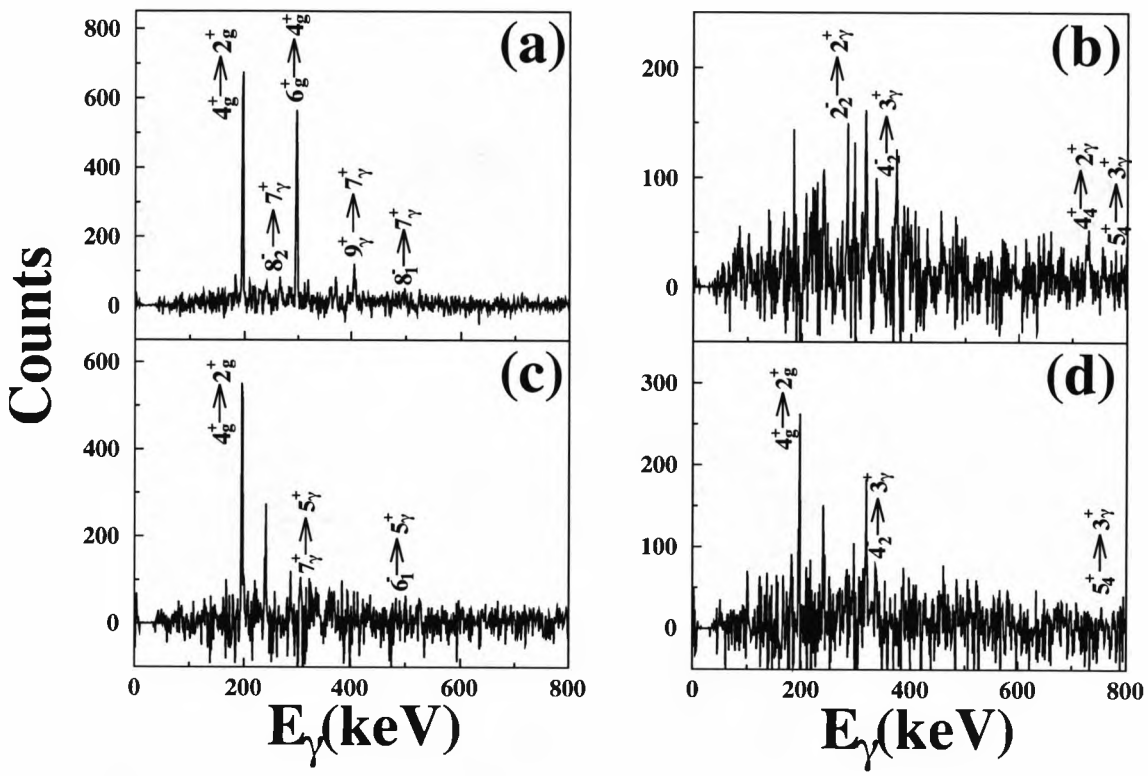

Figure 5.13: Spectra produced by gates set on transitions between the γ-band and the ground state band. (a) gate on the 1035 keV $7^+_\gamma \rightarrow 6^+_g$ transition, (b) gate on the 964 keV $3^+_\gamma \rightarrow 2^+_g$ and $2^+_\gamma \rightarrow 0^+_g$ transitions, (c) gate on the 1005 keV $5^+_\gamma \rightarrow 4^+_g$ transition, (d) gate on the 763 keV $3^+_\gamma \rightarrow 4^+_g$ transition. Transitions within the gsb and between higher lying bands and the γ-band are marked. Many of the other transitions are from other unknown levels or are contaminants from ^{161}Dy or ^{162}Dy.

later ^{158}Gd(α,2n)^{160}Dy experiment[44] observed the 6_S^+ and 8_S^+ levels at 1726.5 keV and 1978.3 keV, and also the 10_S^+ level at 2265.2 keV. The energies of the 6_S^+ and 8_S^+ levels were higher than those given in the earlier experiment, but within the errors, the 4_S^+ level was not populated.

In the present work the 4_S^+, 6_S^+, 8_S^+ and 10_S^+ levels were all populated, and observed to decay to the gsb. The energies of the levels are lower than those reported in the (α,2n) reaction, but closer to the energies reported in the (^{3}He,α) reaction. Transitions between levels within the S-band are not observed.

The 4^+-band.

The $K^\pi = 4^+$ band had previously been observed to spin 7[44]. In the present work only the 4^+ and 5^+ levels are populated, and observed to decay to the γ-band.

The 1^--band.

The $K^\pi = 1^-$ band had previously been observed to spin 10[44]. In the present work it is populated to spin 8. The 6^- and 8^- levels are observed to decay to the γ-band. The lower levels (1^-–5^-) are observed to decay to the gsb. No transitions between levels within the 1^--band are observed.

The 2^--band.

The $K^\pi = 2^-$ band had previously been populated to possible 12^- and 14^- levels. It is the most strongly populated of the quasiparticle bands seen in this reaction, where it is observed to spin 14. Figure 5.14 shows the spectra given by the sum of gates on the 288 keV, 360 keV and 425 keV transitions between levels in the 2^--band and the sum of gates on the 835 keV, 935 keV, 1013 keV and 1036 keV transitions between the 2^--band and the gsb. In these spectra the transitions within the 2^--band, between the 2^--band and the γ-band, between the 2^--band and gsb and within the gsb are clearly seen. The peaks at 139 keV, 222 keV, 240 keV and 318 keV are mostly contaminants from ^{161}Dy. In neither of these spectra is there any evidence of strong feeding of the 2^--band from a higher lying band.

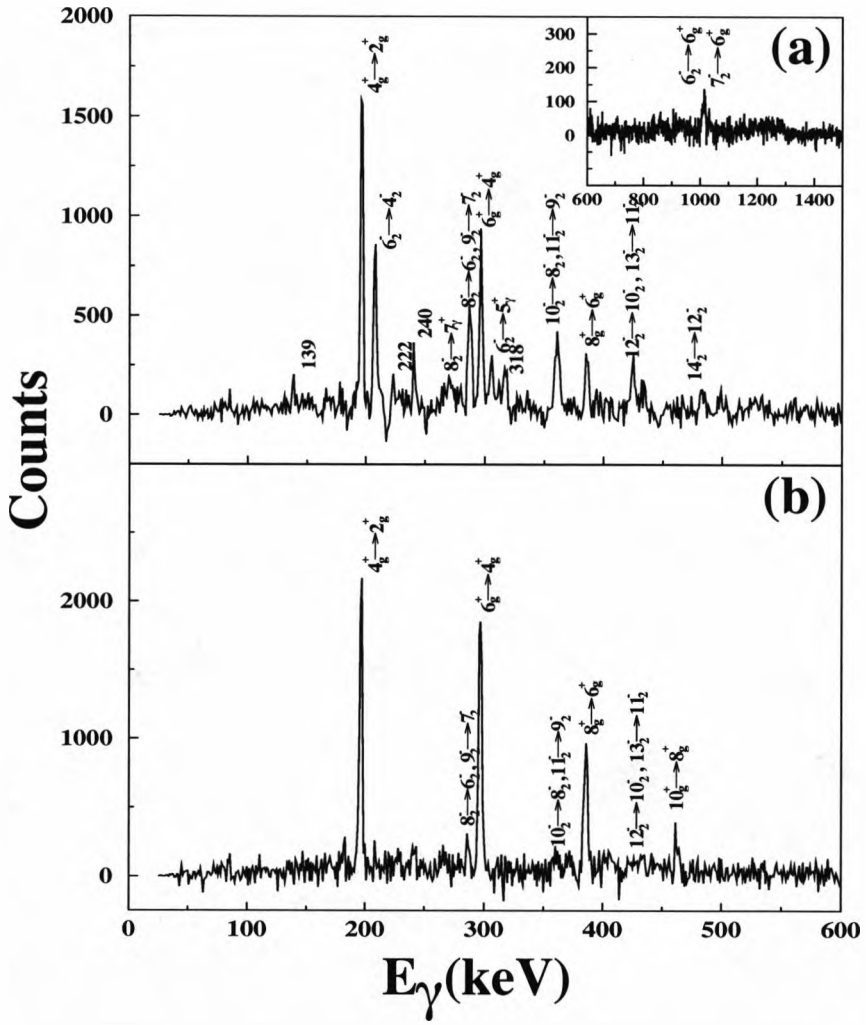

Figure 5.14: Spectra (a) in coincidence with transitions between levels in the 2^--band and (b) in coincidence with transitions from the 2^--band to the ground state band. The peaks at 139 keV, 222 keV, 240 keV and 318 keV are largely contaminants from ^{161}Dy.

The 4^--band.

The $K^\pi = 4^-$ band had previously been populated to spin 7[44]. In the present work only decays from the 5^- level to the gsb are observed. The 4^--band was observed in reference[44] to show peculiar decays from the 5^- level to the 6^+_g and 4^+_g levels, which could result from a $K = 0{,}1$ admixture of only a few percent. It is only these transitions from the 4^--band that are observed in the present work.

The 8^--band.

The $K^\pi = 8^-$ bandhead at 2288.0 keV had previously been observed[44]. In the present work this band head at 2285.4 keV is observed to decay to the 8^+_g and 8^+_γ levels. The strong decay of the 8^- bandhead to the 8^+_g state is surprising. High K states would normally be expected to decay to the γ-vibrational state. This indicates that there is probably some strong mixing with low K states.

Population of states in ^{62}Ni.

The correction for the Doppler shift can also be made assuming that the γ-ray is emitted by the scattered Ni nucleus. A p-γ-γ matrix was produced with one axis giving the energy of the γ-rays assuming they were emitted by the Dy and the other axis assuming the γ-rays were emitted by the Ni. Gates were then set on transitions in Dy producing spectra of γ-rays emitted by the Ni in coincidence with that transition. It was hoped that it would then be possible to determine whether the energy sharing in the Ni depended on the population of different 2 quasiparticle configurations in the Dy. Figure 5.15 show the Ni spectra in coincidence with transitions in the $K^\pi = 2^-$ band and the ground state band. There are insufficient statistics in the spectra produced by the gates on transitions from the 2^--band to say determine whether the population of states in the Ni is different than the spectra produced the the gate on the ground state band.

Figure 5.16 is part of the level scheme for ^{62}Ni, showing the transitions labelled in figure 5.15. The 1442 keV transition seen in figure 5.15 is not known in ^{62}Ni, or in any of the other Ni isotopes populated in this experiment.

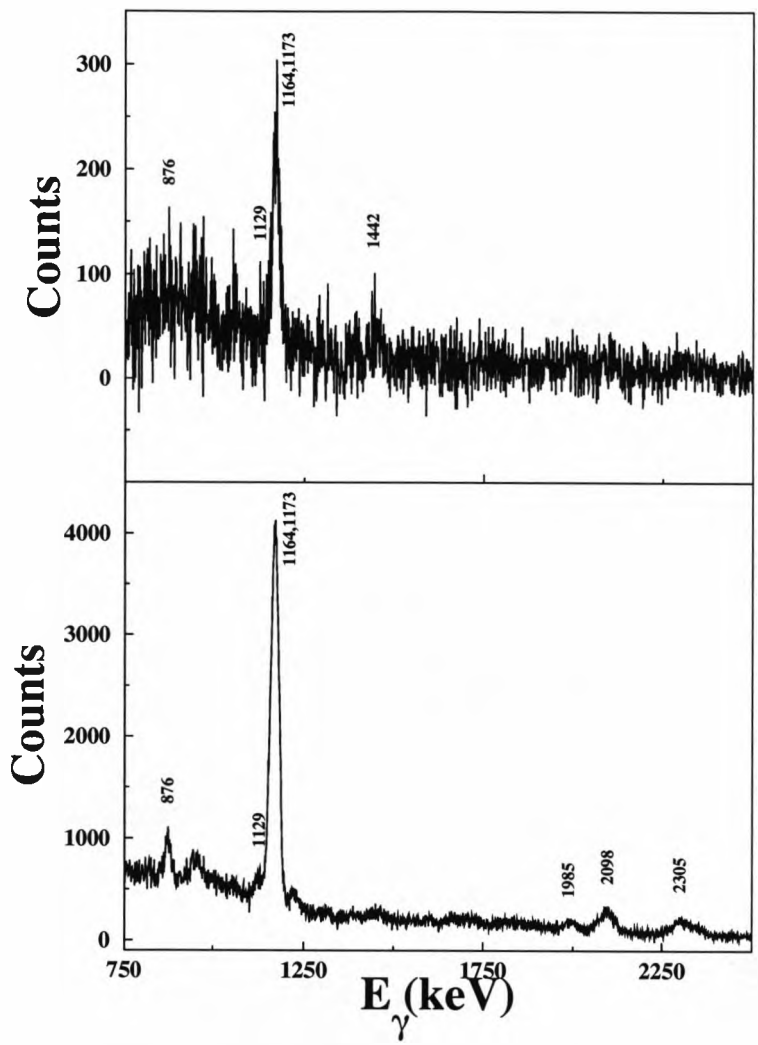

Figure 5.15: Spectra of ^{62}Ni γ-rays in coincidence with (a) transitions from or in the 2^--band and (b) the strong transitions in the ground state band.

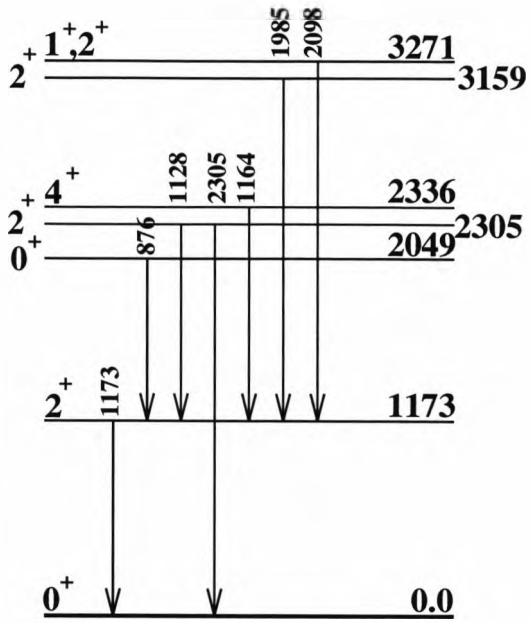

Figure 5.16: Part of the level scheme for ^{62}Ni, showing the transitions labelled in figure 5.15.

5.3.4 The Population of ^{162}Dy.

States in ^{162}Dy were populated via the stripping reaction, and also by Coulomb excitation of the 2.5% target impurity. To determine the relative population of the side bands in ^{162}Dy populated by the transfer reaction it is necessary to correct for the inelastic excitation of the ^{162}Dy in the target.

To do this the output from Gosia[52] was used to give the relative population of each level in the ground state band of ^{162}Dy following inelastic excitation. It was assumed that inelastic excitation only significantly excites the ground state band. Gosia showed that the 184 keV $4_g^+ \rightarrow 2_g^+$ transition accounts for 90% of the population of ^{162}Dy by inelastic excitation. The intensity of this transition as a result of inelastic excitation can be found by a comparison with the inelastic excitation of ^{161}Dy.

The intensity of the 167 keV γ-ray in ^{161}Dy is 651.0 ± 0.8 with an internal conversion coefficient $\alpha = 0.44$[51] giving the total intensity of the 167 keV transition as 937.4 ± 1.2. There are two transitions from the $\frac{13}{2}^+$ level, there is also a 83 keV transition to the $\frac{11}{2}^+$ level, which is 75% of the 167 keV γ-ray intensity[50]. The γ-ray intensity of this transition is therefore 488.3 ± 0.6 with an internal conversion coefficient $\alpha = 4.9$ giving the total intensity as 2881.0 ± 3.5. Therefore, the population

of the $\frac{13}{2}^+$ level is 3818 ± 4. From the Gosia calculation, the population of this level accounts for 59% of the Coulomb excitation of ^{161}Dy. Therefore, the total intensity of the Coulomb excitation of ^{161}Dy is 6471 ± 7. The intensity of the $4_g^+ \rightarrow 2_g^+$ transition in ^{162}Dy due to Coulex is expected to be $\frac{2.5}{95.9}(6471 \pm 7) \times 0.9 = 151.8 \pm 0.2$. The measured intensity of the 185 keV $4_g^+ \rightarrow 2_g^+$ transition is 294.3 ± 0.7 with an internal conversion coefficient $\alpha = 0.32$ giving the total intensity of the 184 keV transition as 388.5 ± 0.7.

This calculation gives that 39% of the $4_g^+ \rightarrow 2_g^+$ transition strength in ^{162}Dy is due to inelastic excitation of the target, and 61% is due to the transfer.

The relative intensities of transitions in ^{162}Dy as a result of transfer are given in table 5.5. The intensities of the transitions from the γ-band to the ground state band due to transfer are found assuming that the population of the γ-band as a result of Coulomb excitation is neglibable. The relative intensities of the higher ground state band transitions due to transfer were found by subtracting the intensities given by Gosia. The intensities can be normalized to the ^{161}Dy transitions, the 184.2 keV $4_g^+ \rightarrow 2_g^+$ γ-ray has an intensity of 179.5 ± 0.4 due to transfer.

Figure 5.17 shows the observed level scheme for ^{162}Dy, with the known levels in the 2^-[55] and S-bands[45] and the (unobserved) transitions marked in figure 5.7 and given in table 5.5 shown by dashed arrows. No transitions from other known bands[55] were observed.

The ground state band (gsb) had previously been observed to spin 18[55], it is observed here to be populated to spin 12 by the transfer reaction. The γ-vibrational band is known to spin 14[55], it is observed here to spin 10.

5.3.5 γ-ray Multiplicities.

The γ-ray multiplicity of the transfer channels were compared to the multiplicity of the inelastic channel. In this analysis the measurement of the multiplicity was deduced from the ratio of the number of particle-γ-γ events to the number of particle-γ events.

Gates on peaks in each of the three isotopes, and suitable background regions, were set and the data was sorted to give spectra for the fold associated with each

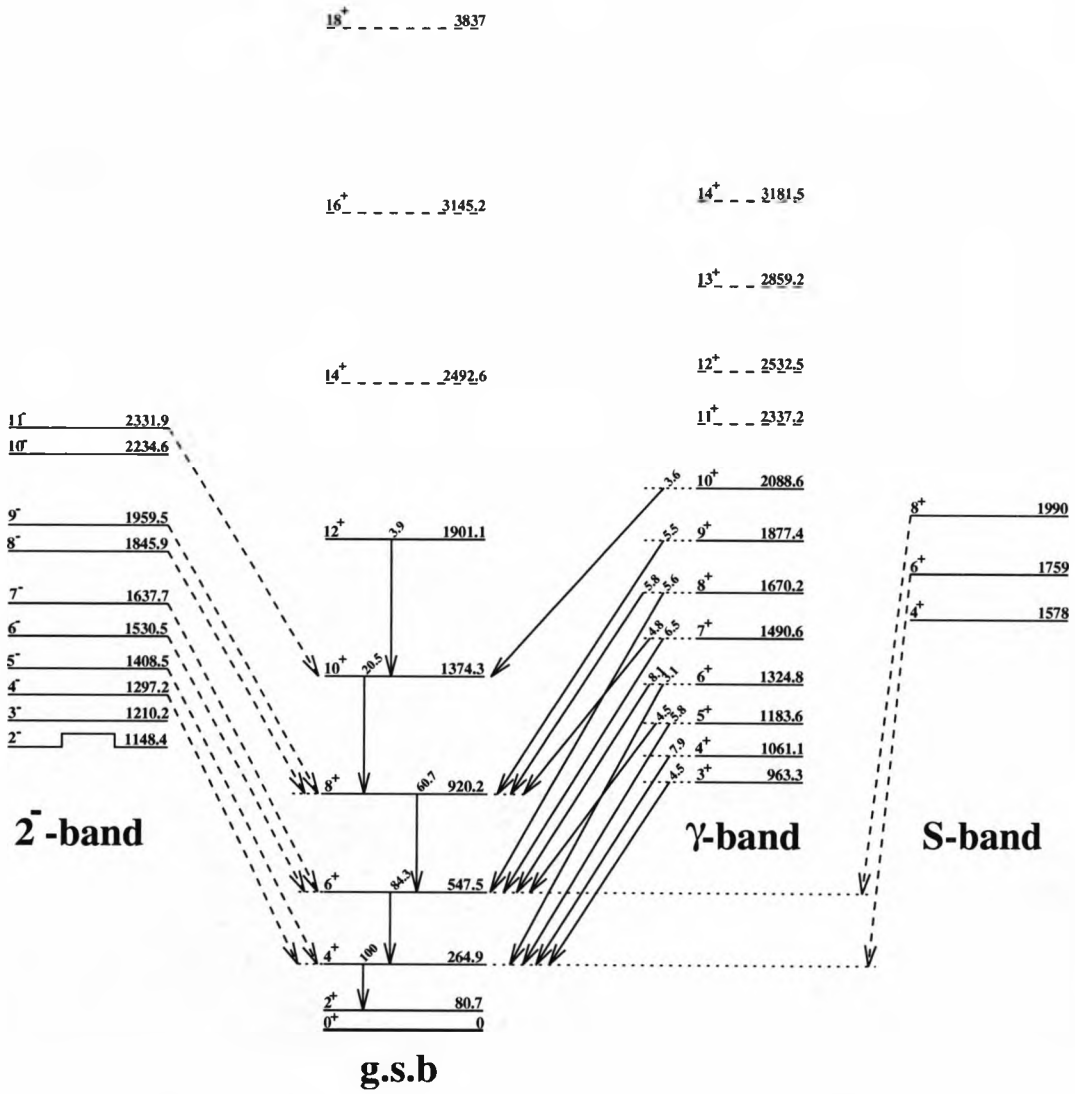

Figure 5.17: The level scheme for ^{162}Dy, showing the observed transitions and their relative intensities. The levels of the known 2^- and S-bands are also shown. The transitions marked with dashed arrows are the transitions which should be seen if these bands were populated. The levels marked with dashed lines are known from previous experiments but not observed here.

E_γ (keV)	Transition	I_γ	E_γ (keV)	Transition	I_γ
184.2	$4_g^+ \rightarrow 2_g^+$	100.0(3)	925	$8_2^- \rightarrow 8_g^+$	< 0.8
282.6	$6_g^+ \rightarrow 4_g^+$	84.3(4)	943.0	$7_\gamma^+ \rightarrow 6_g^+$	6.5(3)
372.7	$8_g^+ \rightarrow 6_g^+$	60.7(3)	957.2	$9_\gamma^+ \rightarrow 8_g^+$	4.9–6.8
454.1	$10_g^+ \rightarrow 8_g^+$	20.5(1)	957	$11_2^- \rightarrow 10_g^+$	< 1.8
526.8	$12_g^+ \rightarrow 10_g^+$	3.9(1)	962	$11_\gamma^+ \rightarrow 10_g^+$	
570.4	$7_\gamma^+ \rightarrow 8_g^+$	4.8(2)	980.3	$6_2^- \rightarrow 6_g^+$	< 1.0
591.5	$14_g^+ \rightarrow 12_g^+$	0.0	1031	$4_2^- \rightarrow 4_g^+$	< 0.8
634.9	$5_\gamma^+ \rightarrow 6_g^+$	4.5(3)	1038	$9_2^- \rightarrow 8_g^+$	< 0.8
652.6	$16_g^+ \rightarrow 14_g^+$	0.0	1059.1	$6_\gamma^+ \rightarrow 4_g^+$	3.1(2)
698.4	$3_\gamma^+ \rightarrow 4_g^+$	4.5(2)	1089	$7_2^- \rightarrow 6_g^+$	< 1.0
714.3	$10_\gamma^+ \rightarrow 10_g^+$	3.6(2)	1127.6	$8_\gamma^+ \rightarrow 6_g^+$	5.6(3)
750.0	$8_\gamma^+ \rightarrow 8_g^+$	5.8(3)	1142	$5_2^- \rightarrow 4_g^+$	< 1.6
778.0	$6_\gamma^+ \rightarrow 6_g^+$	8.1(3)	1442	$8_S^+ \rightarrow 6_g^+$	< 0.5
796.2	$4_\gamma^+ \rightarrow 4_g^+$	7.9(4)	1494	$6_S^+ \rightarrow 4_g^+$	< 0.7
919.9	$5_\gamma^+ \rightarrow 4_g^+$	5.8(3)			

Table 5.5: Energies and relative intensities of ^{162}Dy transitions derived in present work. The intensities given are for the transfer part of the ^{162}Dy channel.

isotope with background subtracted. The number of p-γ and p-γ-γ events for each channel were then measured.

In ^{161}Dy using a gate defined by the 139 keV $\frac{15}{2}^+ \rightarrow \frac{13}{2}^+$ and $\frac{11}{2}^+ \rightarrow \frac{7}{2}^+$, 167 keV $\frac{13}{2}^+ \rightarrow \frac{9}{2}^+$, 222 keV $\frac{15}{2}^+ \rightarrow \frac{11}{2}^+$, 240 keV $\frac{17}{2}^+ \rightarrow \frac{13}{2}^+$, 311 keV $\frac{19}{2}^+ \rightarrow \frac{15}{2}^+$, 318 keV $\frac{21}{2}^+ \rightarrow \frac{17}{2}^+$ and 396 keV $\frac{25}{2}^+ \rightarrow \frac{21}{2}^+$ transitions there were 12072269 p-γ events and 2294336 p-γ-γ events. The ratio of particle-γ-γ events to particle-γ events for the inelastic excitation of ^{161}Dy is therefore 0.19.

In ^{160}Dy using a gate defined by the 197 keV $4^+ \rightarrow 2^+$, 297 keV $6^+ \rightarrow 4^+$, 386 keV $8^+ \rightarrow 6^+$ and 462 keV $10^+ \rightarrow 8^+$ transitions there were 2588106 p-γ events and 1133385 p-γ-γ events. The ratio of particle-γ-γ events to particle-γ events for the ^{160}Dy channel is therefore 0.44.

In ^{162}Dy using a gate defined by the 184 keV $4^+ \rightarrow 2^+$, 283 keV $6^+ \rightarrow 4^+$, 373 keV $8^+ \rightarrow 6^+$ and 454 keV $10^+ \rightarrow 8^+$ transitions there were 1066357 p-γ events and 310199 p-γ-γ events. The ratio of particle-γ-γ events to particle-γ events for the total ^{162}Dy channel is therefore 0.29. However, 39% of this is the multiplicity for the

inelastic excitation and 61% the multiplicity due to the transfer. From the Gosia calculations the average excitation energy for the inelastic excitation of ^{161}Dy and ^{162}Dy can be found. From this and the known internal conversion coefficients[51] the average number of γ-rays emitted as a result of inelastic excitation can be found. The result of this is that the relative multiplicity following inelastic excitation of ^{162}Dy to that of ^{161}Dy is 1.8, and the ratio of multiplicities for the inelastic excitation of ^{162}Dy is 0.34. Therefore, the ratio of p-γ-γ events to p-γ events due to transfer to ^{162}Dy is $\frac{0.29-0.34\times0.39}{0.61} = 0.26$.

The ratios of the number of particle-γ-γ events to the number of particle-γ events were 0.44, 0.19 and 0.26 for the ^{160}Dy channel, the ^{161}Dy channel and the transfer contribution to ^{162}Dy respectively. These values imply that the multiplicity of the pick-up channel is about a factor of two larger than than for the inelastic channel, which is consistent with previous measurements[8]. The much lower multiplicity for the stripping channel is consistent with the non-observation of transitions from excited two quasiparticle states.

5.4 Discussion.

It can be seen by comparing the results for ^{160}Dy in table 5.3 with the results for ^{162}Dy in table 5.5 that the relative intensities of transitions from the γ-vibrational band to the ground state band are similar. However, transitions from the previously observed 2^- and S-bands to the ground state band are not observed in ^{162}Dy. The relative population of the 2^--band in ^{162}Dy is $< 50\%$ the relative population of this band in ^{160}Dy, and the relative population of the S-band is $< 30\%$ the population in ^{160}Dy.

Figure 5.18 gives the available neutron orbits for Dy isotopes derived from a cranked shell model calculation for a deformation of $\beta_2 = 0.25$. The ground state of ^{161}Dy has an unpaired (95^{th}) neutron in the $1i_{\frac{13}{2}}$, $\Omega = \frac{5}{2}$ level. Levels at $\hbar\omega = 0$ and $\hbar\omega \approx 0.2$ correspond to no Coulomb excitation and rotation induced by Coulomb excitation at the point of transfer respectively.

Figure 5.19 gives the available neutron orbits for Ni isotopes taken from refer-

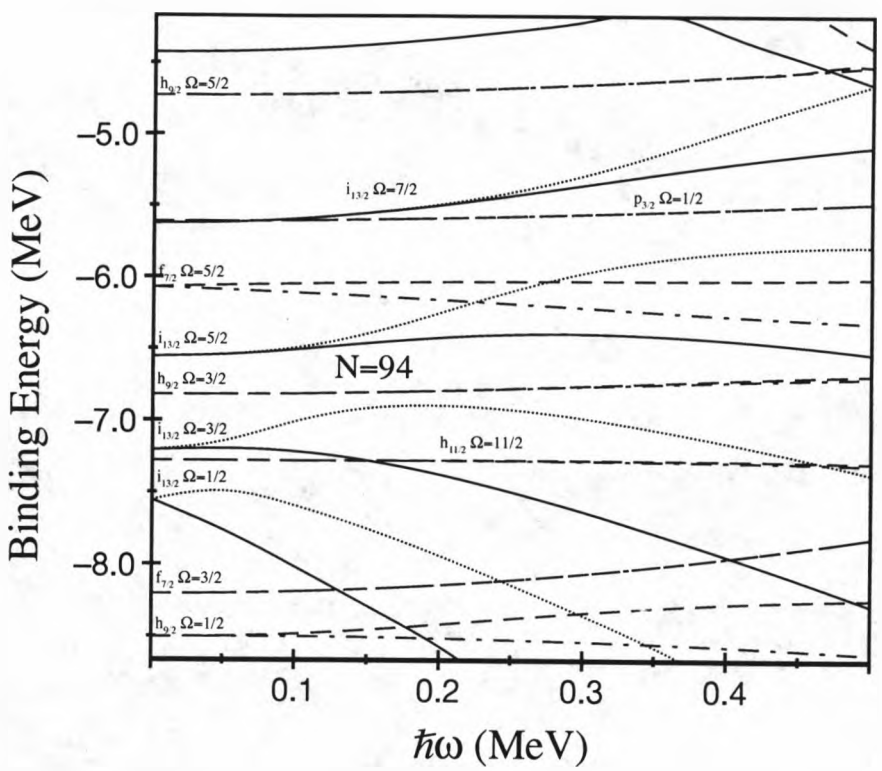

Figure 5.18: Neutron orbits for Dy isotopes derived from a cranked shell model calculation based on deformation $\beta_2 = 0.25$. The solid and dotted lines are positive parity states (positive and negative signature respectively), and the dot-dash and dashed lines are negative parity states (positive and negative signature respectively). The orbitals are labelled, and the N=94 shell gap is marked. The ground state of ^{161}Dy has the unpaired (95^{th}) neutron in the $i_{\frac{13}{2}}$, $\Omega = \frac{5}{2}$ level.

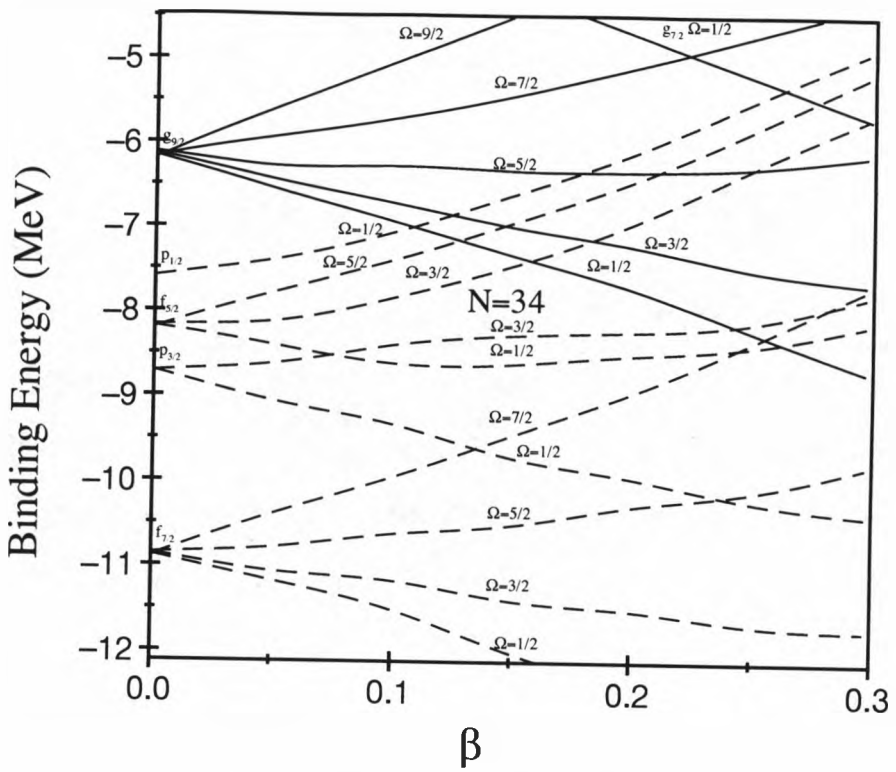

Figure 5.19: Neutron orbits for Ni isotopes taken from reference[27] for zero rotation. The solid lines are positive parity states, and the dashed lines are negative parity states. The orbitals are labelled, and the N=34 shell gap is marked. The ground state of ^{61}Ni has the unpaired (33^{rd}) neutron in the $p_{\frac{3}{2}}$, $\Omega = \frac{3}{2}$ level with deformation $\beta \approx 0.10$.

ence [27] for the Ni having no rotational energy. The ground state of ^{61}Ni has an unpaired (33^{rd}) neutron in the $p_{\frac{3}{2}}$, $\Omega = \frac{3}{2}$ level, so the deformation of ^{61}Ni is $\beta \approx 0.10$. For both of these figures the binding energy is found from the neutron seperation energy for ^{161}Dy and ^{61}Ni.

$$S_n = [m_{A-1} - m_A + m_n]c^2 \tag{5.1}$$

where $m_n = 939.6$ MeV/c^2 is the neutron mass. The mass of the nucleus, $m_A c^2 = \Delta + Ac^2$, where $c^2 = 931.5$ MeV. This gives the binding energy of the valence neutron as 6.6 MeV for ^{161}Dy and 8.6 MeV for ^{61}Ni. The binding energies of other states are then found from the spacing of levels at $\hbar\omega = 0$ in figure 5.18 for the Dy and figure 5.19 for the Ni.

Calculations based on the semi-classical formalism of Alder et al [18] were carried

out. These sum over the transfer probabilities to vacant orbitals in ^{61}Ni given in figure 5.19 for the pick-up reaction (to give ^{160}Dy) or from occupied orbitals in ^{61}Ni for the stripping reaction.

5.4.1 Semi-classical Transfer Theory (SCTT).

The differential cross section for transfer, if the use of a semi-classical theory is valid, can be written[18]

$$\frac{d\sigma}{d\Omega} = \left(\frac{d\sigma}{d\Omega}\right)_R P(\theta, \rho, \xi, \delta) \tag{5.2}$$

where the Rutherford cross section is

$$\left(\frac{d\sigma}{d\Omega}\right)_R = \frac{1}{4}\overline{a_c}^2 \sin^{-4}\left(\tfrac{1}{2}\theta\right) \tag{5.3}$$

with $\overline{a_c}$ the half distance of closest approach in a head-on collision.

Considering reactions of the form ${}^{A_1}_{Z_1}(C_1 + {}^{N}_{Z_N} n) + {}^{A_2}_{Z_2} C_2 \rightarrow C_1 + (C_2 + n)$, the transfer probability, $P(\theta, \rho, \xi, \delta)$, for the transfer of a nucleon or cluster, n, from a donor level n_1, l_1, j_1 in the projectile nucleus, $C_1 + n$, to an acceptor level n_2, l_2, j_2 in the target nucleus, C_2, is given by

$$P(\theta, \rho, \xi, \delta) = \chi^2 \sum_{\lambda} \begin{pmatrix} j_1 & j_2 & \lambda \\ \frac{1}{2} & -\frac{1}{2} & 0 \end{pmatrix}^2 B_\lambda(\theta, \rho, \xi, \delta) \tag{5.4}$$

The transferred angular momentum, λ, is restricted by the conservation of momentum and parity,

$$|l_1 - l_2| \leq \lambda \leq l_1 + l_2 \tag{5.5}$$

$$|j_1 - j_2| \leq \lambda \leq j_1 + j_2 \tag{5.6}$$

$$l_1 + l_2 + \lambda \text{ is even} \tag{5.7}$$

$\varepsilon = (\sin(\frac{1}{2}\theta))^{-1}$ is used to replace θ, giving $B_\lambda(\varepsilon, \rho, \xi, \delta)$. Scattering to $\theta = 180°$ is considered, so $\varepsilon = 1$ is used.

The parameter ξ is defined by the difference in the Coulomb parameters in the final and initial states.

$$\xi = \eta_f - \eta_i \tag{5.8}$$

$$\eta_i = \frac{e^2}{\hbar^2}\frac{Z_1 Z_2 m_i^*}{k_i} \tag{5.9}$$

$$\eta_f = \frac{e^2}{\hbar^2}\frac{(Z_1 - Z_N)(Z_2 + Z_N)m_f^*}{k_f} \tag{5.10}$$

where m_i^* and m_f^* are the reduced masses and k_i and k_f are the wave numbers.

$$k_i = \sqrt{\frac{2m_i^*}{\hbar^2}E_i} \tag{5.11}$$

$$k_f = \sqrt{\frac{2m_f^*}{\hbar^2}E_f} \tag{5.12}$$

where E_i and E_f are the kinetic energies of the system in the centre of mass in MeV.

$$E_i = \frac{m_p}{m_p + m_t}E_{lab} \tag{5.13}$$

$$E_f = E_i + Q \tag{5.14}$$

A mean Coulomb parameter $\eta = \frac{1}{2}(\eta_i + \eta_f)$ and wavenumber are $k = \frac{1}{2}(k_i + k_f)$ are defined. The half distance of closest approach for a head on collision is given by

$$\overline{a_c} = \eta/k \tag{5.15}$$

The parameter δ is a measure of the charge and mass transfer

$$\delta = \frac{uk_i\eta_i - vk_f\eta_f}{k} \tag{5.16}$$

where

$$u = 1 - \frac{N}{A_1}\frac{R_0 A_1^{\frac{1}{3}}}{\overline{a_c}(1+\varepsilon)} \tag{5.17}$$

$$v = \frac{A_2}{A_2 + N} + \frac{N}{A_2 + N}\frac{R_0 A_1^{\frac{1}{3}}}{\overline{a_c}(1+\varepsilon)} \tag{5.18}$$

The wavenumbers for the nucleons in the donor level, κ_1, and the acceptor level, κ_2, are

$$\kappa_1 = \sqrt{\frac{2m_i^*}{\hbar^2}|E_1^b|} = 0.2187\sqrt{\frac{N(A_1 - N)}{A_1}|E_1^b|} \tag{5.19}$$

$$\kappa_2 = 0.2187\sqrt{\frac{NA_2}{A_2+N}|E_2^b|} \tag{5.20}$$

where $|E_1^b|$ is the binding energy of a nucleon in the donor level and $|E_2^b|$ is the binding energy of a nucleon in the acceptor level.

The parameter ρ is defined as

$$\rho = \gamma_2\kappa_2\overline{a_c} \tag{5.21}$$

For neutron transfer $\gamma_2 = 1$.

A new parameter, ξ_{eff}, is defined,

$$\xi_{eff} \approx \xi + \left(\frac{\varepsilon}{1+\varepsilon}\right)\delta \tag{5.22}$$

And $B_\lambda(\varepsilon,\rho,\xi,\delta) \approx B_\lambda(\varepsilon=1,\rho,\xi_{eff}=0,\delta=0)$ is used. A plot of $B_\lambda(1,\rho,0,0)$ vs ρ for various λ is plotted in figure 5.20, which is taken from reference[18]. $B_\lambda(\varepsilon,\rho,\xi,\delta)$ is considerably larger for larger values of λ, so only the largest possible λ is used in the summation to give $P(\theta,\rho,\xi,\delta)$, equation (5.4).

The strength parameter χ^2 is defined by,

$$\chi^2 = 4\pi\frac{A_1(A_1-N)A_2(A_2+N)}{(A_1+A_2)^2}\frac{2J_f+1}{2J_i+1}\left(\frac{2M}{\hbar^2}\theta_{j_1l_1}\theta_{j_2l_2}\frac{N_{n_2l_2j_2}(\gamma_2\kappa_2)A_{n_1l_1j_1}}{\kappa_1\gamma_2\kappa_2}\right)^2 \tag{5.23}$$

where $\theta_{j_1l_1}$ and $\theta_{j_2l_2}$ are the spectroscopic factors for the donor and acceptor levels. These indicate how good the single particle description is for this state. J_i and J_f are the initial and final target spins. The form factor,

$$A_{n_1l_1j_1} = \int_0^{r=R_c-R_0A_2^{\frac{1}{3}}} r_1^2dr_1f_{n_1l_1j_1}(\kappa_1r_1)V(r_1,r=r_c-R_0A_2^{\frac{1}{3}})i_{l_1}(\gamma_2\kappa_2r_1) \tag{5.24}$$

For neutron transfers,

$$A_{n_1l_1j_1} \approx \frac{\hbar^2}{2M}N_{n_1l_1j_1}\left(\frac{\kappa_2}{\kappa_1}\right)^{l_1}\frac{1}{\kappa_1} \tag{5.25}$$

which is exact for $\kappa_1 = \kappa_2$.

$$\chi^2 = \frac{263}{E_i}\frac{(A_1-N)(A_2+N)}{A_1+A_2}\frac{2J_f+1}{2J_i+1}\left(\theta_{j_1l_1}\theta_{j_2l_2}N_{n_1l_1j_1}N_{n_2l_2j_2}\frac{(\gamma_2\kappa_2)^{l_1-1}}{(\gamma_1\kappa_1)^{l_1+1}}\right)^2 \tag{5.26}$$

where,

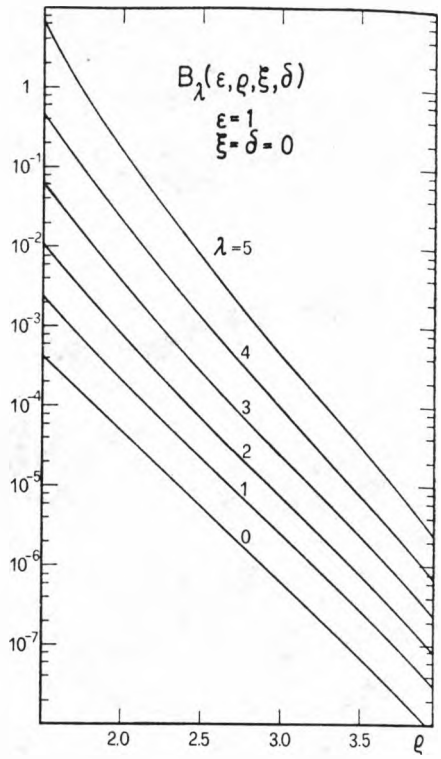

Figure 5.20: The transfer function $B_\lambda(1,\rho,0,0)$ vs ρ for different angular momenta, λ. Taken from reference[18].

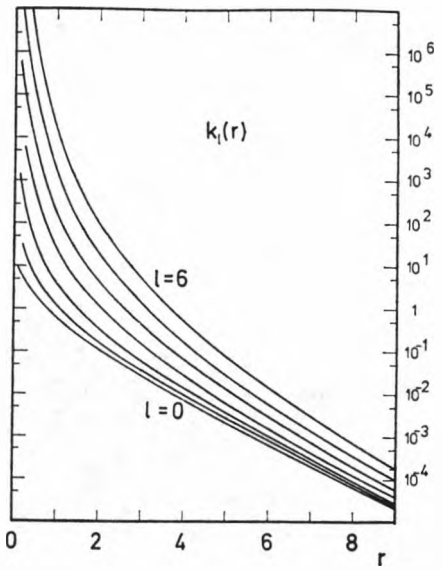

Figure 5.21: The Macdonald functions $k_l(r = \gamma\kappa R_0 A^{\frac{1}{3}})$ for various values of l. Taken from reference[18].

$$N_{nlj} = \frac{U_{nlj}(\gamma\kappa R_0 A^{\frac{1}{3}})}{k_l(\gamma\kappa R_0 A^{\frac{1}{3}})} \tag{5.27}$$

where $k_l(r)$ is the Macdonald function, which is plotted in figure 5.21. The asymptotic radial nucleon wavefunction $U_{nlj}(\gamma\kappa R_0 A^{\frac{1}{3}})$ is plotted in figure 5.22, both of these figures are taken from reference[18].

5.4.2 SCTT Applied to the ^{161}Dy(^{61}Ni,^{62}Ni)^{160}Dy Reaction.

This theory was then applied to this experiment. The calculations were carried out using the binding energies for $\hbar\omega = 0$ and $\hbar\omega = 0.2$, which gave similar results for the two values of $\hbar\omega$. This is because the binding energies in figure 5.18 for $\hbar\omega = 0$ and $\hbar\omega = 0.2$ are similar. The results of the calculations given below are all for $\hbar\omega = 0$.

The calculations assume that the spectroscopic factors $\theta_{j_1 l_1} = 1$ and $\theta_{j_2 l_2} = 1$. This assumes that the state is described perfectly by considering the transferred nucleon as a single particle which orbits a fixed core. It is assumed that this core is unaffected by the presence or absence of the nucleon or the transfer process. This will be unrealistic, however for the purpose of comparing the population of states in the two nuclei formed by the pick-up and stripping reactions it is reasonable to assume that the spectroscopic factors for similar configurations in the nuclei will be similar,

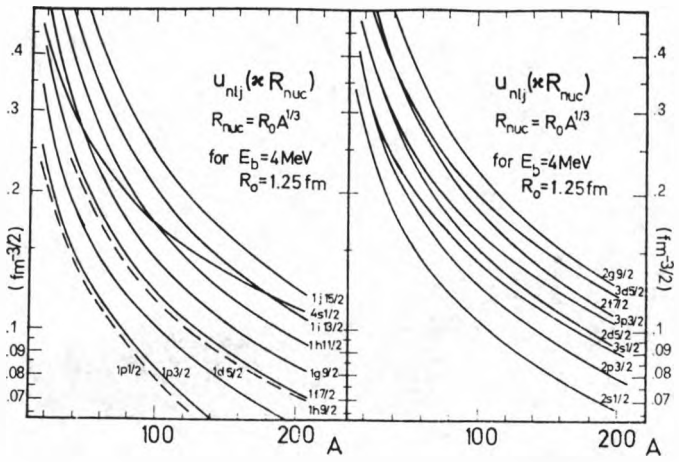

Figure 5.22: The asymptotic radial nucleon wavefunction $U_{nlj}(\kappa R_{nuc})$ as a function of mass number A for several nuclear states. Taken from reference[18].

and so in comparing different states the spectroscopic factors cancel out. The initial target spin, assuming the target is in the ground state, $J_i = \frac{5}{2}$. And the final target spin, J_f, is the K value for the two quasiparticle configuration in the residual Dy nucleus.

For the pick-up reaction to populate states in ^{160}Dy the neutron must be placed in one of the unoccupied orbitals at or just above the Fermi level in ^{61}Ni. From figure 5.9 the amount of the transfer channel populating each orbital in the Ni can be found. The configurations that these levels correspond to are known[56]. Transfers which put the neutron in a $2p_{\frac{3}{2}}$ orbital populate the 0^+ level at 0.0 MeV, the 0^+ level at 2.05 MeV and the 2^+ level at 3.16 MeV. Transfers which put the neutron in a $1f_{\frac{5}{2}}$ orbital populate the 2^+ level at 2.30 MeV and the 4^+ level at 2.34 MeV. Transfers which put the neutron in a $2p_{\frac{1}{2}}$ orbital populate the 2^+ level at 1.17 MeV and the group of levels between 3.27 MeV and 3.86 MeV. The values of E_b, κ_1, U_{nlj}, k_l, N_{nlj}, l_1, j_1 and the population for these orbitals are given in table 5.6. The neutron is taken from an occupied orbital at or just below the Fermi level in ^{161}Dy, the values of E_b, κ_2, ρ, U_{nlj}, k_l, N_{nlj}, l_2 and j_2 for the orbitals that give configurations for known bands in ^{160}Dy are given in table 5.7.

The values of $P(\theta, \rho, \xi, \delta)$ for the different orbitals in Ni for each of the configurations in ^{160}Dy involving a $1i_{\frac{13}{2}}$ $\Omega = \frac{5}{2}$ orbital which give the known bands in ^{160}Dy are

orbit	$2p_{\frac{3}{2}}\ \Omega=\frac{3}{2}$	$1f_{\frac{5}{2}}\ \Omega=\frac{3}{2}$	$1f_{\frac{5}{2}}\ \Omega=\frac{5}{2}$	$2p_{\frac{1}{2}}\ \Omega=\frac{1}{2}$
E_b(MeV)	8.6	8.2	7.8	7.5
κ_1	0.636	0.621	0.606	0.594
U_{nlj}	0.17	0.15	0.15	0.15
k_l	0.05	0.2	0.2	0.05
N_{nlj}	3.4	0.75	0.75	3.0
l_1	1	3	3	1
j_1	$\frac{3}{2}$	$\frac{5}{2}$	$\frac{5}{2}$	$\frac{1}{2}$
Population	0.13	0.12	0.27	0.48

Table 5.6: Values of E_b, κ_1, U_{nlj}, k_l, N_{nlj}, l_1, j_1 and the population for the states in Ni that the neutron may be put into for the pick-up reaction.

orbit	$1i_{\frac{13}{2}}\ \Omega=\frac{5}{2}$	$1h_{\frac{9}{2}}\ \Omega=\frac{3}{2}$	$1i_{\frac{13}{2}}\ \Omega=\frac{3}{2}$	$1h_{\frac{11}{2}}\ \Omega=\frac{11}{2}$	$2f_{\frac{7}{2}}\ \Omega=\frac{3}{2}$	$1h_{\frac{9}{2}}\ \Omega=\frac{1}{2}$
E_b(MeV)	6.6	6.9	7.3	7.4	8.3	8.6
κ_2	0.564	0.576	0.593	0.597	0.632	0.643
ρ	3.8	3.9	4.0	4.0	4.3	4.4
U_{nlj}	0.13	0.085	0.13	0.12	0.12	0.085
k_l	1.0	0.2	1.0	0.2	4×10^{-4}	0.2
N_{nlj}	0.13	0.43	0.13	0.60	3.0	0.43
l_2	6	5	6	5	3	5
j_2	$\frac{13}{2}$	$\frac{9}{2}$	$\frac{13}{2}$	$\frac{11}{2}$	$\frac{7}{2}$	$\frac{9}{2}$

Table 5.7: Values of E_b, κ_2, ρ, U_{nlj}, k_l, N_{nlj}, l_2, and j_2 for the states in Dy that the neutron may be taken from for the pick-up reaction.

orbit	$2p_{\frac{3}{2}}\ \Omega=\frac{3}{2}$	$1f_{\frac{5}{2}}\ \Omega=\frac{3}{2}$	$1f_{\frac{5}{2}}\ \Omega=\frac{5}{2}$	$2p_{\frac{1}{2}}\ \Omega=\frac{1}{2}$
$\frac{\kappa_2^{l_1-1}}{\kappa_1^{l_1+1}}$	2.47	2.14	2.36	2.83
χ^2	11.9	0.44	0.53	12.2
λ	7	9	9	7
$B_\lambda(1,\rho,0,0)$	4×10^{-5}	2×10^{-4}	2×10^{-4}	4×10^{-5}
$\begin{pmatrix} j_1 & j_2 & \lambda \\ \frac{1}{2} & -\frac{1}{2} & 0 \end{pmatrix}^2$	0.1029	0.0882	0.0882	0.5000
$P(\theta,\rho,\xi,\delta)$	4.7×10^{-6}	1.2×10^{-5}	1.5×10^{-5}	2.3×10^{-5}
E_x(MeV)	0.0	0.4	0.8	1.1
$\lvert E_x-Q_{gg}\rvert$(MeV)	4.2	3.8	3.4	3.1
$\sum P(\theta,\rho,\xi,\delta)$	1.3×10^{-4}			

Table 5.8: Values of $P(\theta,\rho,\xi,\delta)$ for the population of a $(\nu i_{\frac{13}{2}})^2$, E_{qp}=0.0 MeV ground state in ^{160}Dy taking the neutron from the $1i_{\frac{13}{2}}\ \Omega=\frac{5}{2}$ level and putting it into one of the levels in ^{61}Ni.

given in tables 5.8–5.16. The value of the total excitation energy, E_x, of the residual Dy and Ni nuclei and the difference between E_x and the ground state Q-value, Q_{gg}, of the reaction are also given. The value of K^π for each state is given. The spin K is found from the sum of the projection of the spin (Ω) values of the two particles in the configuration, either added in parallel or antiparallel giving two K values. The parity π is found from the product of the parities of the two particles, particles with the same parity giving positive parity states and particles with different parities giving negative parity states.

The energy of the resulting two quasiparticle configuration is given by;

$$E_{qp}=\Delta+(\Delta^2+(E_{sp}-\lambda)^2)^{\frac{1}{2}} \tag{5.28}$$

where $\Delta\approx0.85$ MeV is the pairing strength, E_{sp} is the energy of the unpaired neutron and λ is the Fermi energy.

The total $P(\theta,\rho,\xi,\delta)$ is the sum over all the states in Ni scaled by the population for the state in Ni. It is assumed that the population of states in Ni is the same for each of the configurations in the Dy. This is unlikely, but due to insufficient statistics it was not possible to determine the population pattern in the Ni for each of the configurations in the Dy. The dependence of the cross section on the excitation

orbit	$2p_{\frac{3}{2}}\ \Omega=\frac{3}{2}$	$1f_{\frac{5}{2}}\ \Omega=\frac{3}{2}$	$1f_{\frac{5}{2}}\ \Omega=\frac{5}{2}$	$2p_{\frac{1}{2}}\ \Omega=\frac{1}{2}$
$\frac{\kappa_2^{l_1-1}}{\kappa_1^{l_1+1}}$	2.47	2.36	2.64	2.83
χ^2	391	17.4	21.7	400
λ	6	6	6	4
$B_\lambda(1,\rho,0,0)$	4×10^{-6}	4×10^{-6}	4×10^{-6}	1×10^{-6}
$\begin{pmatrix} j_1 & j_2 & \lambda \\ \frac{1}{2} & -\frac{1}{2} & 0 \end{pmatrix}^2$	0.4091	0.1061	0.1061	0.5000
$P(\theta,\rho,\xi,\delta)$	6.4×10^{-4}	7.4×10^{-6}	9.2×10^{-6}	2.0×10^{-4}
E_x(MeV)	0.2	0.6	1.0	1.3
$\lvert E_x-Q_{gg}\rvert$(MeV)	4.0	3.6	3.2	2.9
$\sum P(\theta,\rho,\xi,\delta)$	1.8×10^{-4}			

Table 5.9: Values of $P(\theta,\rho,\xi,\delta)$ for the population of a $\nu i_{\frac{13}{2}} h_{\frac{9}{2}}$ 1^-, E_{qp}=1.7 MeV state in ^{160}Dy taking the neutron from the $1h_{\frac{9}{2}}$ $\Omega=\frac{3}{2}$ level and putting it into one of the levels in ^{61}Ni.

orbit	$2p_{\frac{3}{2}}\ \Omega=\frac{3}{2}$	$1f_{\frac{5}{2}}\ \Omega=\frac{3}{2}$	$1f_{\frac{5}{2}}\ \Omega=\frac{5}{2}$	$2p_{\frac{1}{2}}\ \Omega=\frac{1}{2}$
$\frac{\kappa_2^{l_1-1}}{\kappa_1^{l_1+1}}$	2.47	2.36	2.64	2.83
χ^2	1173	52.1	65.2	1199
λ	6	6	6	4
$B_\lambda(1,\rho,0,0)$	4×10^{-6}	4×10^{-6}	4×10^{-6}	1×10^{-6}
$\begin{pmatrix} j_1 & j_2 & \lambda \\ \frac{1}{2} & -\frac{1}{2} & 0 \end{pmatrix}^2$	0.4091	0.1061	0.1061	0.5000
$P(\theta,\rho,\xi,\delta)$	1.9×10^{-3}	2.2×10^{-5}	2.8×10^{-5}	6.0×10^{-4}
E_x(MeV)	0.2	0.6	1.0	1.3
$\lvert E_x-Q_{gg}\rvert$(MeV)	4.0	3.6	3.2	2.9
$\sum P(\theta,\rho,\xi,\delta)$	5.5×10^{-4}			

Table 5.10: Values of $P(\theta,\rho,\xi,\delta)$ for the population of a $\nu i_{\frac{13}{2}} h_{\frac{9}{2}}$ 4^-, E_{qp}=1.7 MeV state in ^{160}Dy taking the neutron from the $1h_{\frac{9}{2}}$ $\Omega=\frac{3}{2}$ level and putting it into one of the levels in ^{61}Ni.

orbit	$2p_{\frac{3}{2}}\ \Omega=\frac{3}{2}$	$1f_{\frac{5}{2}}\ \Omega=\frac{3}{2}$	$1f_{\frac{5}{2}}\ \Omega=\frac{5}{2}$	$2p_{\frac{1}{2}}\ \Omega=\frac{1}{2}$
$\frac{\kappa_2^{l_1-1}}{\kappa_1^{l_1+1}}$	2.47	2.36	2.64	2.83
χ^2	11.9	0.53	0.66	12.2
λ	7	9	9	7
$B_\lambda(1,\rho,0,0)$	4×10^{-5}	4×10^{-4}	4×10^{-4}	4×10^{-5}
$\begin{pmatrix} j_1 & j_2 & \lambda \\ \frac{1}{2} & -\frac{1}{2} & 0 \end{pmatrix}^2$	0.1029	0.0882	0.0882	0.5000
$P(\theta,\rho,\xi,\delta)$	4.9×10^{-5}	1.9×10^{-5}	2.3×10^{-5}	2.4×10^{-4}
E_x(MeV)	0.6	1.0	1.4	1.7
$\lvert E_x-Q_{gg}\rvert$(MeV)	3.6	3.2	2.8	2.5
$\sum P(\theta,\rho,\xi,\delta)$	1.3×10^{-4}			

Table 5.11: Values of $P(\theta,\rho,\xi,\delta)$ for the population of a $(\nu i_{\frac{13}{2}})^2$, E_{qp}=1.9 MeV state in ^{160}Dy taking the neutron from the $1i_{\frac{13}{2}}\ \Omega=\frac{3}{2}$ level and putting it into one of the levels in ^{61}Ni.

orbit	$2p_{\frac{3}{2}}\ \Omega=\frac{3}{2}$	$1f_{\frac{5}{2}}\ \Omega=\frac{3}{2}$	$1f_{\frac{5}{2}}\ \Omega=\frac{5}{2}$	$2p_{\frac{1}{2}}\ \Omega=\frac{1}{2}$
$\frac{\kappa_2^{l_1-1}}{\kappa_1^{l_1+1}}$	2.47	2.40	2.64	2.83
χ^2	1776	81.6	98.7	1815
λ	4	0	0	4
$B_\lambda(1,\rho,0,0)$	6×10^{-7}	8×10^{-8}	8×10^{-8}	6×10^{-7}
$\begin{pmatrix} j_1 & j_2 & \lambda \\ \frac{1}{2} & -\frac{1}{2} & 0 \end{pmatrix}^2$	0.3409	0.0	0.0	0.0
$P(\theta,\rho,\xi,\delta)$	3.6×10^{-4}	0.0	0.0	0.0
E_x(MeV)	0.7	1.1	1.5	1.8
$\lvert E_x-Q_{gg}\rvert$(MeV)	3.5	3.1	2.7	2.4
$\sum P(\theta,\rho,\xi,\delta)$	4.7×10^{-5}			

Table 5.12: Values of $P(\theta,\rho,\xi,\delta)$ for the population of a $\nu i_{\frac{13}{2}}\, h_{\frac{11}{2}}\ 3^-$, E_{qp}=2.0 MeV state in ^{160}Dy taking the neutron from the $1h_{\frac{11}{2}}\ \Omega=\frac{11}{2}$ level and putting it into one of the levels in ^{61}Ni.

orbit	$2p_{\frac{3}{2}}\ \Omega=\frac{3}{2}$	$1f_{\frac{5}{2}}\ \Omega=\frac{3}{2}$	$1f_{\frac{5}{2}}\ \Omega=\frac{5}{2}$	$2p_{\frac{1}{2}}\ \Omega=\frac{1}{2}$
$\frac{\kappa_2^{l_1-1}}{\kappa_1^{l_1+1}}$	2.47	2.40	2.64	2.83
χ^2	4313	198	240	4408
λ	4	0	0	4
$B_\lambda(1,\rho,0,0)$	6×10^{-7}	8×10^{-8}	8×10^{-8}	6×10^{-7}
$\begin{pmatrix} j_1 & j_2 & \lambda \\ \frac{1}{2} & -\frac{1}{2} & 0 \end{pmatrix}^2$	0.3409	0.0	0.0	0.0
$P(\theta,\rho,\xi,\delta)$	8.8×10^{-4}	0.0	0.0	0.0
E_x(MeV)	0.7	1.1	1.5	1.8
$\lvert E_x-Q_{gg}\rvert$(MeV)	3.5	3.1	2.7	2.4
$\sum P(\theta,\rho,\xi,\delta)$	1.1×10^{-4}			

Table 5.13: Values of $P(\theta,\rho,\xi,\delta)$ for the population of a $\nu i_{\frac{13}{2}}\,h_{\frac{11}{2}}$ 8^-, E_{qp}=2.0 MeV state in ^{160}Dy taking the neutron from the $1h_{\frac{11}{2}}\ \Omega=\frac{11}{2}$ level and putting it into one of the levels in ^{61}Ni.

orbit	$2p_{\frac{3}{2}}\ \Omega=\frac{3}{2}$	$1f_{\frac{5}{2}}\ \Omega=\frac{3}{2}$	$1f_{\frac{5}{2}}\ \Omega=\frac{5}{2}$	$2p_{\frac{1}{2}}\ \Omega=\frac{1}{2}$
$\frac{\kappa_2^{l_1-1}}{\kappa_1^{l_1+1}}$	2.47	2.69	2.96	2.83
χ^2	19029	1098	1330	19449
λ	4	6	6	4
$B_\lambda(1,\rho,0,0)$	2×10^{-7}	6×10^{-7}	6×10^{-7}	2×10^{-7}
$\begin{pmatrix} j_1 & j_2 & \lambda \\ \frac{1}{2} & -\frac{1}{2} & 0 \end{pmatrix}^2$	0.1786	0.3788	0.0816	0.5000
$P(\theta,\rho,\xi,\delta)$	6.8×10^{-4}	2.5×10^{-4}	6.5×10^{-5}	1.9×10^{-3}
E_x(MeV)	1.6	2.0	2.4	2.7
$\lvert E_x-Q_{gg}\rvert$(MeV)	2.6	2.2	1.8	1.5
$\sum P(\theta,\rho,\xi,\delta)$	1.0×10^{-3}			

Table 5.14: Values of $P(\theta,\rho,\xi,\delta)$ for the population of a $\nu i_{\frac{13}{2}}\,f_{\frac{7}{2}}$ 1^-, E_{qp}=2.7 MeV state in ^{160}Dy taking the neutron from the $2f_{\frac{7}{2}}\ \Omega=\frac{3}{2}$ level and putting it into one of the levels in ^{61}Ni.

orbit	$2p_{\frac{3}{2}}\ \Omega=\frac{3}{2}$	$1f_{\frac{5}{2}}\ \Omega=\frac{3}{2}$	$1f_{\frac{5}{2}}\ \Omega=\frac{5}{2}$	$2p_{\frac{1}{2}}\ \Omega=\frac{1}{2}$
$\frac{\kappa_2^{l_1-1}}{\kappa_1^{l_1+1}}$	2.47	2.69	2.96	2.83
χ^2	57088	3295	3989	58346
λ	4	6	6	4
$B_\lambda(1,\rho,0,0)$	2×10^{-7}	6×10^{-7}	6×10^{-7}	2×10^{-7}
$\begin{pmatrix} j_1 & j_2 & \lambda \\ \frac{1}{2} & -\frac{1}{2} & 0 \end{pmatrix}^2$	0.1786	0.3788	0.0816	0.5000
$P(\theta,\rho,\xi,\delta)$	2.0×10^{-3}	7.5×10^{-4}	2.0×10^{-4}	5.8×10^{-3}
E_x(MeV)	1.6	2.0	2.4	2.7
$\lvert E_x-Q_{gg}\rvert$(MeV)	2.6	2.2	1.8	1.5
$\sum P(\theta,\rho,\xi,\delta)$	3.1×10^{-3}			

Table 5.15: Values of $P(\theta,\rho,\xi,\delta)$ for the population of a $\nu i_{\frac{13}{2}} f_{\frac{7}{2}}$ 4^-, E_{qp}=2.7 MeV state in ^{160}Dy taking the neutron from the $2f_{\frac{7}{2}}\ \Omega=\frac{3}{2}$ level and putting it into one of the levels in ^{61}Ni.

orbit	$2p_{\frac{3}{2}}\ \Omega=\frac{3}{2}$	$1f_{\frac{5}{2}}\ \Omega=\frac{3}{2}$	$1f_{\frac{5}{2}}\ \Omega=\frac{5}{2}$	$2p_{\frac{1}{2}}\ \Omega=\frac{1}{2}$
$\frac{\kappa_2^{l_1-1}}{\kappa_1^{l_1+1}}$	2.47	2.78	3.07	2.83
χ^2	652	40.2	49.0	666
λ	6	6	6	4
$B_\lambda(1,\rho,0,0)$	2×10^{-6}	2×10^{-6}	2×10^{-6}	2×10^{-7}
$\begin{pmatrix} j_1 & j_2 & \lambda \\ \frac{1}{2} & -\frac{1}{2} & 0 \end{pmatrix}^2$	0.4091	0.1061	0.1061	0.5000
$P(\theta,\rho,\xi,\delta)$	5.3×10^{-4}	8.5×10^{-6}	1.0×10^{-5}	6.7×10^{-5}
E_x(MeV)	2.0	2.4	2.8	3.1
$\lvert E_x-Q_{gg}\rvert$(MeV)	2.2	1.8	1.4	1.1
$\sum P(\theta,\rho,\xi,\delta)$	1.0×10^{-4}			

Table 5.16: Values of $P(\theta,\rho,\xi,\delta)$ for the population of a $\nu i_{\frac{13}{2}} h_{\frac{9}{2}}$ 2^-, E_{qp}=3.0 MeV state in ^{160}Dy taking the neutron from the $1h_{\frac{9}{2}}\ \Omega=\frac{1}{2}$ level and putting it into one of the levels in ^{61}Ni.

hole orbital	K^π	E_{qp} (MeV)	$\sum P(\theta,\rho,\xi,\delta)$
$\nu i_{\frac{13}{2}}\ \Omega=\frac{5}{2}$	0^+ (gsb)	0.0	1.3×10^{-4}
$\nu h_{\frac{9}{2}}\ \Omega=\frac{3}{2}$	1^-	1.7	1.8×10^{-4}
$\nu h_{\frac{9}{2}}\ \Omega=\frac{3}{2}$	4^-	1.7	5.5×10^{-4}
$\nu i_{\frac{13}{2}}\ \Omega=\frac{3}{2}$		1.9	1.3×10^{-4}
$\nu h_{\frac{11}{2}}\ \Omega=\frac{11}{2}$	3^-	2.0	4.7×10^{-5}
$\nu h_{\frac{11}{2}}\ \Omega=\frac{11}{2}$	8^-	2.0	1.1×10^{-4}
$\nu f_{\frac{7}{2}}\ \Omega=\frac{3}{2}$	1^-	2.7	1.0×10^{-3}
$\nu f_{\frac{7}{2}}\ \Omega=\frac{3}{2}$	4^-	2.7	3.1×10^{-3}
$\nu h_{\frac{9}{2}}\ \Omega=\frac{3}{2}$	2^-	3.0	1.0×10^{-4}

Table 5.17: Values of $P(\theta,\rho,\xi,\delta)$ summed over states in Ni for configurations in ^{160}Dy which involve the $1i_{\frac{13}{2}}$, $\Omega=\frac{5}{2}$ neutron and a hole in the orbital given.

energy is not considered.

The values of $P(\theta,\rho,\xi,\delta)$ summed over the levels in Ni for each of the configurations in ^{160}Dy are given in table 5.17 along with the K^π and E_{qp} for the resulting two quasiparticle state. The values of E_{qp} given assume pure two quasiparticle states, mixing with other two quasiparticle and octupole states will reduce these. Since it is known that the two quasiparticle states mix strongly[57] the values of K^π and E_{qp} are guides derived from assuming pure two quasiparticle natures for these states.

The S-band.

The S-band has been previously observed in both ^{160}Dy[43, 44] and ^{162}Dy[45] and assigned a $(\nu i_{\frac{13}{2}})^2$ (0^+) configuration. The two quasiparticle energy of the $(\nu i_{\frac{13}{2}})^2$ band is $\approx$ 1.9 MeV. The lowest lying level of this band observed is the 4^+ level at 1610 keV, so the energy of this band is lower than the predicted two quasiparticle energy.

The 4^+-band.

The $K^\pi=4^+$ band has previously been observed in ^{160}Dy[44] and assigned a $\nu h_{\frac{9}{2}} f_{\frac{7}{2}}$ configuration. Such a state is not directly populated by the removal of one neutron from the ^{161}Dy ground state, although it is weakly populated in this experiment.

The 2^--band.

The significant population of the $K^\pi = 2^-$ band is surprising. This band was not seen in the (^{3}He,α) reaction[43] and reference[44] suggests that it has a $\pi d_{\frac{5}{2}} h_{\frac{11}{2}}$ configuration based on the population of a similar band in ^{162}Dy following β-decay of ^{162}Tb[46] and the non-observation of this band in the neutron transfer reaction mentioned above. Reference[44] also states that this band is likely to be octupole in origin and mixes with higher lying (unseen) $K^\pi = 0^-$ and 1^- octupole bands. The $K^\pi = 0^-$ band interaction shifts the odd-spin members of the 2^--band downwards, it also affects the observed 1^--band in the same way.

The 2^--band is also known to mix with $\nu i_{\frac{13}{2}} h_{\frac{9}{2}}$ two quasineutron states[57], one of which can be formed directly by removing a neutron from the ^{161}Dy ground state. This state has a two quasiparticle energy of 3.0 MeV, which is considerably higher than the observed band head energy of 1.26 MeV.

The 1^- and 4^--bands.

The $K^\pi = 1^-$ and $K^\pi = 4^-$ bands previously observed in ^{160}Dy[43, 44] have the same $\nu i_{\frac{13}{2}} h_{\frac{9}{2}}$ configuration, the 1^--band resulting from antiparallel and the 4^--band from parallel coupling. The 1^--band has octupole vibrational character[44] but to a smaller extent than the 2^--band. Table 5.17 suggests that the 4^--band should be the more strongly populated of the two bands, however in this experiment the 1^--band is seen to be the more strongly populated.

The 8^--band.

The $K^\pi = 8^-$ band has been previously observed and assigned a $\nu i_{\frac{13}{2}} h_{\frac{11}{2}}$ configuration. Table 5.17 suggests that this band should be accompanied by a 3^- state populated with approximately 45% of the strength of the 8^- state based on the same configuration with antiparallel coupling. Such a band would be too weak to be seen in this data, and is not known from other experiments[53].

The Octupole Bands.

Two octupole bands, the 1^- and 2^-- bands, have been populated in this experiment. Both of these bands are populated more strongly than would be suggested if they were purely two quasiparticle in nature. The 1^--band should be populated more weakly than the 4^--band based on parallel coupling of the same configuration, but it is populated more strongly. The 2^--band has a mainly two quasiproton configuration, and so should not be significantly populated in a neutron transfer experiment, and indeed was not seen in an earlier light ion induced neutron transfer reaction[43].

Octupole bands are expected to contain both proton and neutron components, in which case it would be unlikely that they are populated by a neutron transfer reaction. It is possible however that the strong population of octupole bands is the result of virtual proton transfer occurring simultaneously with the neutron transfer.

5.4.3 SCTT Applied to the ^{161}Dy(^{61}Ni,^{60}Ni)^{162}Dy Reaction.

For the stripping reaction to populate states in ^{162}Dy the neutron must be taken from one of the occupied orbitals at or just below the Fermi level in ^{61}Ni. The population of the different states in ^{60}Ni can be found from the known relative population of levels in ^{60}Ni. The values of E_b, κ_2, ρ, U_{nlj}, k_l, N_{nlj}, l_1, j_1 and the population for these orbitals are given in table 5.18. The neutron is placed in an unoccupied level at or just above the Fermi level in ^{161}Dy, the values of E_b, κ_1, U_{nlj}, k_l, N_{nlj}, l_2, and j_2 for the levels which give known bands in ^{162}Dy are given in table 5.19.

The values of $P(\theta, \rho, \xi, \delta)$, E_x and $|E_x - Q_{gg}|$ for the different orbitals in Ni for each of the possible configurations in the ^{162}Dy involving an $1i_{\frac{13}{2}}$ $\Omega = \frac{5}{2}$ orbital giving known bands in ^{162}Dy are given in tables 5.20–5.23.

The values of $P(\theta, \rho, \xi, \delta)$ summed over the levels in Ni for each of the configurations in ^{162}Dy are given in table 5.24 along with the K^π and E_{qp} for the resulting two quasiparticle states.

orbit	$2p_{\frac{3}{2}}\ \Omega=\frac{3}{2}$	$2p_{\frac{3}{2}}\ \Omega=\frac{1}{2}$	$1f_{\frac{7}{2}}\ \Omega=\frac{5}{2}$
E_b(MeV)	8.6	10.0	10.8
κ_2	0.647	0.697	0.725
ρ	4.4	4.7	4.9
U_{nlj}	0.17	0.17	0.17
k_l	0.05	0.05	0.2
N_{nlj}	3.4	3.4	0.85
l_2	1	1	3
j_2	$\frac{3}{2}$	$\frac{3}{2}$	$\frac{7}{2}$
Population	0.18	0.57	0.25

Table 5.18: Values of E_b, κ_2, ρ, U_{nlj}, k_l, N_{nlj}, l_2, j_2 and population for the states in Ni that the neutron may be taken from for the stripping reaction.

orbit	$1i_{\frac{13}{2}}\ \Omega=\frac{5}{2}$	$2f_{\frac{7}{2}}\ \Omega=\frac{5}{2}$	$1i_{\frac{13}{2}}\ \Omega=\frac{7}{2}$
E_b(MeV)	6.6	6.2	5.7
κ_1	0.560	0.543	0.521
U_{nlj}	0.13	0.12	0.13
k_l	1.0	0.04	1.0
N_{nlj}	0.13	3.0	0.13
l_1	6	3	6
j_1	$\frac{13}{2}$	$\frac{7}{2}$	$\frac{13}{2}$

Table 5.19: Values of E_b, κ_1, U_{nlj}, k_l, N_{nlj}, l_1, and j_1 for the states in Dy that the neutron may be put into for the stripping reaction.

orbit	$2p_{\frac{3}{2}}\ \Omega=\frac{3}{2}$	$2p_{\frac{3}{2}}\ \Omega=\frac{1}{2}$	$1f_{\frac{7}{2}}\ \Omega=\frac{5}{2}$
$\frac{\kappa_2^{l_1-1}}{\kappa_1^{l_1+1}}$	6.56	9.52	11.6
χ^2	82.3	148	16.1
λ	7	7	9
$B_\lambda(1,\rho,0,0)$	2×10^{-6}	2×10^{-7}	4×10^{-6}
$\begin{pmatrix} j_1 & j_2 & \lambda \\ \frac{1}{2} & -\frac{1}{2} & 0 \end{pmatrix}^2$	0.1538	0.1538	0.0882
$P(\theta,\rho,\xi,\delta)$	2.5×10^{-5}	4.6×10^{-6}	5.7×10^{-6}
E_x(MeV)	0.0	1.43	2.2
$\lvert E_x-Q_{gg}\rvert$(MeV)	0.4	1.0	1.8
$\sum P(\theta,\rho,\xi,\delta)$	8.5×10^{-6}		

Table 5.20: Values of $P(\theta,\rho,\xi,\delta)$ for the population of a $(\nu i_{\frac{13}{2}})^2$, E_{qp}=0.0 MeV ground state in ^{162}Dy taking the neutron from one of the levels in ^{61}Ni and putting it in the $1i_{\frac{13}{2}}\ \Omega=\frac{5}{2}$ level.

orbit	$2p_{\frac{3}{2}}\ \Omega=\frac{3}{2}$	$2p_{\frac{3}{2}}\ \Omega=\frac{1}{2}$	$1f_{\frac{7}{2}}\ \Omega=\frac{5}{2}$
$\frac{\kappa_2^{l_1-1}}{\kappa_1^{l_1+1}}$	4.82	5.59	6.05
χ^2	23668	31834	2331
λ	4	4	6
$B_\lambda(1,\rho,0,0)$	2×10^{-7}	6×10^{-8}	1×10^{-7}
$\begin{pmatrix} j_1 & j_2 & \lambda \\ \frac{1}{2} & -\frac{1}{2} & 0 \end{pmatrix}^2$	0.1786	0.1786	0.0947
$P(\theta,\rho,\xi,\delta)$	8.5×10^{-4}	3.4×10^{-4}	2.2×10^{-5}
E_x(MeV)	0.5	1.9	2.7
$\lvert E_x-Q_{gg}\rvert$(MeV)	0.1	1.5	2.3
$\sum P(\theta,\rho,\xi,\delta)$	3.5×10^{-4}		

Table 5.21: Values of $P(\theta,\rho,\xi,\delta)$ for the population of a $\nu i_{\frac{13}{2}} f_{\frac{7}{2}}$ 0^-, E_{qp}=1.8 MeV state in ^{162}Dy taking the neutron from one of the levels in ^{61}Ni and putting it in the $2f_{\frac{7}{2}}\ \Omega=\frac{5}{2}$ level.

orbit	$2p_{\frac{3}{2}}\ \Omega=\frac{3}{2}$	$2p_{\frac{3}{2}}\ \Omega=\frac{1}{2}$	$1f_{\frac{7}{2}}\ \Omega=\frac{5}{2}$
$\frac{\kappa_2^{l_1-1}}{\kappa_1^{l_1+1}}$	4.82	5.59	6.05
χ^2	260348	350174	25641
λ	4	4	6
$B_\lambda(1,\rho,0,0)$	2×10^{-7}	6×10^{-8}	1×10^{-7}
$\begin{pmatrix} j_1 & j_2 & \lambda \\ \frac{1}{2} & -\frac{1}{2} & 0 \end{pmatrix}^2$	0.1786	0.1786	0.0947
$P(\theta,\rho,\xi,\delta)$	9.4×10^{-3}	3.7×10^{-3}	2.4×10^{-4}
E_x(MeV)	0.5	1.9	2.7
$\lvert E_x-Q_{gg}\rvert$(MeV)	0.1	1.5	2.3
$\sum P(\theta,\rho,\xi,\delta)$	3.9×10^{-3}		

Table 5.22: Values of $P(\theta,\rho,\xi,\delta)$ for the population of a $\nu i_{\frac{13}{2}} f_{\frac{7}{2}}$ 5^-, E_{qp}=1.8 MeV state in ^{162}Dy taking the neutron from one of the levels in ^{61}Ni and putting it in the $2f_{\frac{7}{2}}\ \Omega=\frac{5}{2}$ level.

orbit	$2p_{\frac{3}{2}}\ \Omega=\frac{3}{2}$	$2p_{\frac{3}{2}}\ \Omega=\frac{1}{2}$	$1f_{\frac{7}{2}}\ \Omega=\frac{5}{2}$
$\frac{\kappa_2^{l_1-1}}{\kappa_1^{l_1+1}}$	10.94	15.8	19.2
χ^2	227	478	44.1
λ	7	7	9
$B_\lambda(1,\rho,0,0)$	2×10^{-6}	2×10^{-7}	4×10^{-6}
$\begin{pmatrix} j_1 & j_2 & \lambda \\ \frac{1}{2} & -\frac{1}{2} & 0 \end{pmatrix}^2$	0.1538	0.1538	0.0882
$P(\theta,\rho,\xi,\delta)$	7.0×10^{-5}	1.5×10^{-5}	1.6×10^{-5}
E_x(MeV)	0.9	2.3	3.1
$\lvert E_x-Q_{gg}\rvert$(MeV)	0.5	1.9	2.7
$\sum P(\theta,\rho,\xi,\delta)$	2.5×10^{-5}		

Table 5.23: Values of $P(\theta,\rho,\xi,\delta)$ for the population of a $(\nu i_{\frac{13}{2}})^2$, E_{qp}=2.1 MeV state in ^{162}Dy taking the neutron from one of the levels in ^{61}Ni and putting it in the $1i_{\frac{13}{2}}\ \Omega=\frac{7}{2}$ level.

neutron orbital	K^π	E_{qp} (MeV)	$\sum P(\theta,\rho,\xi,\delta)$
$\nu i_{\frac{13}{2}}\ \Omega=\frac{5}{2}$	0^+ (gsb)	0.0	8.5×10^{-6}
$\nu f_{\frac{7}{2}}\ \Omega=\frac{5}{2}$	0^-	1.8	3.5×10^{-4}
$\nu f_{\frac{7}{2}}\ \Omega=\frac{5}{2}$	5^-	1.8	3.9×10^{-3}
$\nu i_{\frac{13}{2}}\ \Omega=\frac{7}{2}$		2.1	2.5×10^{-5}

Table 5.24: Values of $P(\theta,\rho,\xi,\delta)$ summed over states in Ni for configurations in ^{162}Dy which involve the $1i_{\frac{13}{2}}$, $\Omega=\frac{5}{2}$ neutron and a neutron in the orbital given.

The 0^- and 5^--bands.

The $K^\pi = 0^-$ and $K^\pi = 5^-$ bands have been observed previously[46] using the ^{160}Gd(α,2n)^{162}Dy reaction. They are not observed in the present experiment.

The S-band.

The S-band based on a $(\nu i_{\frac{13}{2}})^2$ configuration has been previously observed in ^{162}Dy[45] using the ^{161}Dy(α,^{3}He)^{162}Dy reaction. It is not observed in this experiment.

The 2^--band.

The $K^\pi = 2^-$ band in ^{162}Dy has been observed previously and assigned the same $\pi h_{\frac{11}{2}} d_{\frac{5}{2}}$ two quasiproton configuration as the band in ^{160}Dy[46]. This band is not populated in this reation.

5.4.4 Comparison of Pick-up and Strippping Channels.

The probabilities for populating two quasiparticle states in ^{162}Dy given in table 5.24 are similar to those for two quasiparticle states in ^{160}Dy given in table 5.17. However, the measured population of such states in ^{162}Dy is much less than the population of similar states in ^{160}Dy.

In the pick-up reaction it has been shown that over 50% of the excitation energy is taken up ^{62}Ni[48], leaving $\approx$2 MeV excitation in ^{160}Dy. This would leave ^{160}Dy with the energy needed to populate two quasiparticle states with band heads at $\approx 2\Delta = 1.7$ MeV. However, if 50% of the excitation energy in the stripping reaction is taken up by the ^{60}Ni then there is only $\approx$ 0.2 MeV left for excitation of ^{162}Dy. So, ^{162}Dy would be populated at energies well below the band heads of two quasiparticle states, subsequent Coulomb excitation will not significantly excite two quasiparticle states.

5.5 Summary.

Significant population of two quasiparticle and side bands in the ^{161}Dy(^{61}Ni,^{62}Ni)^{160}Dy pick-up reaction has been observed. In particular, the population of the $K^\pi = (0^+)$

S-band, and $K^\pi = 1^-$, 2^- and 4^- bands is appreciable. The observed population of the $K^\pi = 2^-$ (octupole) band is surprising given its alleged (proton) configuration. The population of the other octupole band (the $K^\pi = 1^-$ band) is also stronger than would be expected from a semi-classical transfer theory calculation.

The corresponding two quasiparticle states in ^{162}Dy were not observed in the ^{161}Dy(^{61}Ni,^{60}Ni)^{162}Dy stripping reaction. This can be explained by the low Q-value of this reaction if appreciable sharing of the excitation energy with the projectile is assumed.

Chapter 6

Summary and Conclusion.

6.1 Summary.

6.1.1 Population of Second Minima.

Two experiments were carried out to try to populate states in the second minimum of the nuclear potential surface using Heavy Ion-induced Transfer Reactions (HITR).

The ^{195}Pt(^{61}Ni,^{62}Ni)^{194}Pt reaction was used to try to populate a superdeformed band in ^{194}Pt. There was no indication that this experiment successfully populated a superdeformed band. This may be due to one of two possible explanations. The first is simply that there is no superdeformed band in ^{194}Pt. The second explanation is that the experiment either did not populate the superdeformed band at all, or populated it without sufficient intensity to be observed, either because the overlap between the population window and the superdeformed band is small or the mixing between the superdeformed and normal deformed wavefunctions is weak.

The ^{239}Pu(^{117}Sn,^{118}Sn)^{238}Pu reaction was used to try to populate the known (0^+, $T_{\frac{1}{2}}$ = 0.5 ns, E_x = 2.4 MeV) fission isomer in ^{238}Pu. A single candidate delayed fission event was observed. This would correspond to a cross section for populating the fission isomer in ^{238}Pu using this reaction of (80 ± 80) nb. This low cross section could be because the entry states to the second minimum are unstable with respect to decay through the outer barrier. Alternatively, the two quasiparticle states that the reaction selectively populates do not readily couple to the superdeformed state.

Neither of these experiments significantly populated a state in the second minimum of the nuclear potential.

6.1.2 Population of Quasiparticle States.

An experiment was carried out to populate two quasiparticle states using a HITR.

The ^{161}Dy(^{61}Ni,^{62}Ni)^{160}Dy reaction was used to populate collective bands built upon two quasiparticle excitations. Several bands built on two quasineutron excitations involving the $1i_{\frac{13}{2}}$, $\Omega = \frac{5}{2}$ neutron orbital were populated in ^{160}Dy. The $K^{\pi} = 2^{-}$ octupole band was significantly populated, although it has a mainly two quasiproton configuration, and the $K^{\pi} = 1^{-}$ octupole band was also more strongly populated than expected. The $K^{\pi} = 4^{+}$ band was also weakly populated, although it's configuration doesn't involve the $1i_{\frac{13}{2}}$, $\Omega = \frac{5}{2}$ neutron orbital.

States in ^{162}Dy were also populated using the ^{161}Dy(^{61}Ni,^{60}Ni)^{162}Dy reaction. In this reaction there was no indication that any two quasiparticle states had been significantly populated. This can be explained by the low Q-value of this reaction.

6.2 Conclusions and Further Work.

The two experiments attempting to populate states in the second minimum were not very successful. This may be a result of introducing insufficient angular momentum and excitation energy into the residual nucleus to explore the overlap region between the first and second minima. Alternatively, the quasiparticle states that are selectively populated in such a reaction do not readily mix with the second minimum.

There are several possible further experiments that may be performed to attempt to populate a superdeformed band in the $A \approx 190$ region. For example, the ^{195}Pt(^{87}Sr,^{88}Sr)^{194}Pt ($Q_{gg} = 5.0$ MeV) or ^{195}Pt(^{47}Ti,^{48}Ti)^{194}Pt ($Q_{gg} = 5.5$ MeV) reactions could be used to populate ^{194}Pt at higher spin and excitation energy. These reactions should increase the overlap between the superdeformed band in the residual nucleus and the population window. This should enhance the population of the superdeformed band, if it exists. Or, the ^{192}Pt(^{16}O,^{14}C)^{194}Hg two proton stripping reaction may be used to try and populate the known superdeformed band in ^{194}Hg. The sensitivity of these experiments would be greatly enhanced by the use of larger more efficient Ge detector arrays and PPAC's, which would allow the collection of more statistics.

An experiment is planned to try to populate the 0.5 ns fission isomer in ^{238}Pu more strongly using the ^{237}Np(^{58}Ni,^{57}Co)^{238}Pu reaction with similar apparatus as that used for the experiment described in this thesis. A simulation predicts that the detection rate for delayed fission events could be about 600/day, compared to just one event in the experiment described here.

The experiment to populate collective bands built upon two quasiparticle excitations populated several such states, as previous experiments had already suggested. The population of some of these bands was unexpected. The reaction mechanism is relatively selective, most of the bands populated are based on two quasineutron structures involving the $1i_{\frac{13}{2}}$, $\Omega = \frac{5}{2}$ neutron which is the unpaired neutron in the ground state of the target. So, single nucleon transfer reactions induced by heavy ions are useful mechanisms for the selective population of such collective bands.

The advent of larger Ge detector arrays will increase the amount of statistics available to study such structures. In particular, the use of clover or cluster detectors would reduce problems associated with the Doppler broadening of the γ-rays that are detected close to 90°, and the number of detectors will increase the average multiplicity of the events detected. This will enable the detection of weaker transitions, such as those within bands and possibly between bands. It will then be possible to study more accurately the population of such bands, and the interactions (if any) between them.

Bibliography

[1] M.W. Sachs, V. Chasman, and D.A. Bromley, *Phys.Rev.* **139**, B92, (1965).

[2] R. Bock, M. Gross-Schulte, and W. Von Oertzen, *Phys.Lett.* **22**, 456, (1966).

[3] W. Von Oertzen, B. Gebauer, A. Gamp, H.G. Bohlen, F. Busch and D. Schüll, *Z.Phys.* **A313**, 189, (1983).

[4] W. Von Oertzen, H.G. Bohlen, B. Gebauer, R. Künkel, F. Pühlhofer, and D. Schüll, *Z.Phys.* **A326**, 463, (1987).

[5] G. Himmele, H. Backe, P.A. Butler, D. Habs, V. Metag, H.J. Specht, and J.B. Wilhelmy, *Nucl.Phys.* **A404**, 401, (1983).

[6] F.W.N. de Boer, E. Grosse, W. Spreng, H.J. Wollersheim, E.G. Eckert, and Ch. Lauterbach, *GSI Annual Report*, (1984).

[7] A.O. Macchiavelli, M.A. Deleplanque, R.M. Diamond, F.S. Stephens, E.L. Dines, and J.E. Draper, *Nucl.Phys.* **A432**, 436, (1985).

[8] M.W. Guidry, S. Juutinen, X.T. Liu, C.R. Bingham, A.J. Larabee, L.L. Riedinger, C. Baktash, I.Y. Lee, M.L. Halbert, D. Cline, B. Kotlinski, W.J. Kernan, T.M. Semkow, D.G. Sarantites, K. Honkanen, and M. Rajagopalan, *Phys.Lett.* **163B**, 79, (1985).

[9] C.Y. Wu, X.T. Liu, S.P. Sorensen, R.W. Kincaid, M.W. Guidry, D. Cline, W.J. Kernan, E. Vogt, T. Czosnyka, A.E. Kavka, M.A. Stoyer, J.O. Rasmussen, and M.L. Halbert, *Phys.Lett.* **188B**, 25, (1987).

[10] K.G. Helmer, C.Y. Wu, D. Cline, M.A. Deleplanque, R.M. Diamond, A.E. Kavka, W.J. Kernan, X.T. Liu, A.O. Macchiavelli, R.J. McDonald, J.O. Rasmussen, F.S. Stephens, M.A. Stoyer, and E.G. Vogt, *Phys.Rev.* **C44**, 2598 (1991).

[11] P.J. Twin, *Nucl.Phys.* **A522**, 13c, (1991).

[12] V. Metag, D. Habs, and H.J. Specht, *Phys.Reports* **65**, 2, (1980).

[13] M.A. Riley, D.M. Cullen, A. Alderson, I. Ali, P. Fallon, P.D. Forsyth, F. Hanna, S.M. Mullins, J.W. Roberts, J.F. Sharpey-Schafer, P.J. Twin, R. Poynter, R. Wadsworth, M.A. Bentley, A.M. Bruce, J. Simpson, G. Sletten, W. Nazarewicz, T. Bengtsson, R. Wyss, *Nucl.Phys.* **A512**, 178, (1990).

[14] P.A. Butler, C. Baktash, C.R. Bingham, M. Carpenter, D. Cline, B. Cox, M.W. Guidry, J. Juutinen, A.E. Kavka, W.J. Kernan, R.W. Kincaid, A. Larabee, I.Y. Lee, X.T. Liu, S.P. Sorensen, E. Vogt, and C.Y. Wu, *Phys.Lett.* **191B**, 333, (1987).

[15] P.D. Bond, *Kernfysisch Versneller Instituut Annual Report*, 484, (1984).

[16] W.R. Phillips, *Rep.Prog.Phys.* **40**, 345, (1977).

[17] L.J.B. Goldfarb and W. von Oertzen, *Heavy Ion Collisions* Ed. R. Bock, 215, (1979).

[18] K. Alder, R. Morf, M. Pauli and D. Trautmann, *Nucl.Phys.* **A191**, 399, (1972).

[19] A. Fleury and J.M. Alexander, *Ann.Rev.Nuc.Sci.* **24**, 279, (1974).

[20] P.J.A. Buttle and L.J.B. Goldfarb, *Nucl.Phys.* **A176**, 299, (1971).

[21] M.W. Guidry, R.W. Kincaid and R. Donangelo, *Phys.Lett.* **150B**, 265, (1985).

[22] M. Girod, J.P. Delaroche and J.F. Berger, *Phys.Rev.* **C38**, 1519, (1988).

M. Girod, J.P. Delaroche, D. Gogny and J.F. Berger, *Phys.Rev.Lett.* **62**, 2452, (1989).

P. Bonche, J. Dobaczewski, H. Flocard, P-H. Heenen and J. Meyer, *Nucl.Phys.* **A510**, 466, (1990).

[23] J. Blons, D. Goutte, A. Leprêtre, R. Lucas, V. Méot, D. Paya, X.H. Phan, G. Barreau, T.P. Doan, G. Pedemay, J.A. Becker and M.A. Stoyer, *Proceedings of the International Conference on Nuclear Structure at High Angular Momentum, Ottawa*, 198, (1992).

[24] P.J. Nolan, D.W. Gifford, P.J. Twin, *Daresbury Laboratory Annual Report, Nuclear Structure Appendix*, 104, (1985/6).

[25] R.J. Poynter, *PhD Thesis, University of Liverpool*, (1989).

[26] C.J. Borkowski and M.K. Kopp, *Rev.Scient.Instr.* **39**, 1515, (1968).

[27] C.M. Lederer and V.S. Shirley, *Table of Isotopes, 7^{th} Edition*, (1978).

[28] C.W. Beausang and E.S. Paul, *private communication.*

[29] B. Singh *Nuclear Data Sheets* **56**, 75, (1989).

[30] J. Halperin *Nuclear Data Sheets* **28**, 485, (1979).

[31] P. Limkilde and G. Sletten, *Nucl.Phys.* **A199**, 504, (1973).

[32] M. Devlin, D. Cline, K.G. Helmer, R. Ibbotson, C.Y. Wu, P.A. Butler, A.J. Cresswell, G.D. Jones, M.A. Stoyer, and J.O. Rasmussen, *Phys.Rev.* **C47**, 2178, (1993).

[33] A.J. Cresswell, M. Devlin, P.A. Butler, D. Cline, K.G. Helmer, R. Ibbotson, G.D. Jones, M.A. Stoyer, J.O. Rasmussen, and C.Y. Wu, Submitted to *Phys.Rev.C.*

[34] M. Jääskeläinen, D.G. Sarantites, R. Woodward, F.A. Dilmanian, J.T. Hood, R. Jääskeläinen, D.C. Hensley, M.L. Halbert, and J.H. Barker, *Nucl.Instr.Meth.* **204**, 385, (1983).

[35] M.A. Stoyer, *PhD Thesis, University of California, Berkeley, LBL-29357*, (1990).

D.C. Aumann and G. Müllen, *Nucl.Instr.Meth.* **115**,75, (1974).

J.E. Evans, R.W. Lougheed, M.S. Coops, R.W. Hoff and E.K. Hulet, *Nucl.Instr.Meth.* **102**, 389, (1972).

[36] Northcliffe and Schilling, *Nuclear Data Tables* **A7**, 233, (1970).

[37] R. Vandenbosch and J.R. Huizenga, *Nuclear Fission*, (Academic Press, New York, 1973).

[38] M.A. Stoyer, *PhD Thesis, University of California, Berkeley, LBL-29357*, (1990).

[39] M.R. Schmorak, *Nuclear Data Sheets* **66**, 839, (1992).

[40] E.N. Shurshikov, *Nuclear Data Sheets* **53**, 601, (1983).

[41] G. Himmele, H. Backe, P.A. Butler, D. Habs, V. Metag, J.B. Wilhelmy, and H.J. Specht, *Nucl.Phys.* **A391**, 191, (1982).

[42] H. Backe, L. Richter, D. Habs, V. Metag, J. Pedersen, P. Singer, and H.J. Specht, *Phys.Rev.Lett.* **42**, 490, (1979).

[43] J. Gen-Ming, J.D. Garrett, G. Løvhøiden, T.F. Thorsteinsen, J.C. Waddington, and J. Rekstad, *Phys.Rev.Lett.* **46**, 222, (1981).

[44] H.J. Riezebos, M.J.A. De Voigt, C.A. Fields, X.W. Cheng, R.J. Peterson, G.B. Hagemann, and A. Stolk, *Nucl.Phys.* **A465**, 1, (1987).

[45] E. Andersen, H. Helstrup, G. Løvhøiden, T.F. Thorsteinsen, M. Guttormsen, S. Messelt, T.S. Tveter, M.A. Hofstee, J.M. Schippers, and S.Y. van der Werf, *Nucl.Phys.* **A550**, 235, (1992).

[46] C.A. Fields, K.H. Hicks, R.A. Ristinen, F.W.N. De Boer, P.M. Walker, J. Borggreen, and L.K. Peker, *Nucl.Phys.* **A389**, 218, (1982).

[47] A.J. Cresswell, P.A. Butler, D. Cline, R.A. Cunningham, M. Devlin, F. Hannachi, R. Ibbotson, G.D. Jones, P.M. Jones, M. Simon, J. Simpson, J.F. Smith, and C.Y. Wu, to be submitted.

[48] C.Y. Wu, D. Cline, M. Devlin, K.G. Helmer, R.W. Ibbotson, M.W. Simon, P.A. Butler, A.J. Cresswell, G.D. Jones, P.M. Jones, J.F. Smith, and R.A. Cunningham, submitted to *Phys.Rev.* **C**.

[49] P.J. Nolan, *Nucl.Phys.* **A520**, 657c, (1990).

[50] R.G. Helmer *Nuclear Data Sheets* **59**, 1, (1990).

[51] R.S. Hager and E.C. Seltzer, *Nucl.Data* **A4**, 1, (1968).

[52] T. Czosnyka, D. Cline and C.Y. Wu, *Bull.Am.Phys.Soc.* **28**, 745, (1983).

[53] C.W. Reich, *Nuclear Data Sheets* **68**, 405, (1993).

[54] F. Kearns, G. Varley, G.D. Dracoulis, T. Inamura, J.C. Lisle and J.C. Willmott, *Nucl.Phys.* **A278**, 109, (1977).

[55] R.G. Helmer *Nuclear Data Sheets* **44**, 659, (1985).

[56] O. Karban, A.K. Basak, F. Entezami and S. Roman, *Nucl.Phys.* **A366**, 68, (1981).

[57] C. Günther, H. Ryde, and K. Krien, *Nucl.Phys.* **A122**, 401, (1968).